Lawrence Berkeley Laboratory
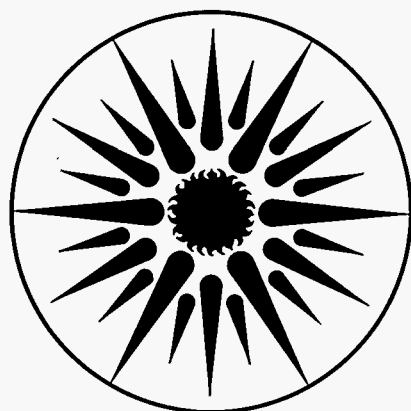
UNIVERSITY OF CALIFORNIA

ENERGY & ENVIRONMENT DIVISION

Applications of X-Ray Absorption Spectroscopy and Low Temperature XMCD to Metalloproteins

J.H. Christiansen
(Ph.D. Thesis)

December 1995

RECEIVED
JUL 3 0 1996
OSTI

**ENERGY
AND ENVIRONMENT
DIVISION**

MASTER

DISCLAIMER

APPLICATIONS OF X-RAY ABSORPTION SPECTROSCOPY

AND

LOW TEMPERATURE XMCD

TO

METALLOPROTEINS

by

Jason H. Christiansen
Ph.D. Thesis

Department of Applied Science
University of California
Davis, California   95616

and

Energy & Environment Division
Ernest Orlando Lawrence Berkeley National Laboratory
University of California
Berkeley, California   94720

January 1996

Recycled Paper

DISCLAIMER

Portions of this document may be illegible in electronic image products. Images are produced from the best available original document.

Applications of X-Ray Absorption Spectroscopy and Low Temperature XMCD to Metalloproteins

Copyright © 1995

by

Jason Hans Christiansen

For Pat
She's had to put up with stress, beamtime travel, late nights, etc.
and she's <u>always</u> been there

Applications of X-Ray Absorption Spectroscopy and Low Temperature XMCD to Metalloproteins

Abstract

I have used the extended x-ray absorption fine structure (EXAFS) and ultra-low temperature x-ray magnetic circular dichroism (XMCD) to study the environments of the metal sites in metalloproteins. EXAFS has been used to study the Zn site in spinach carbonic anhydrase. The EXAFS, in parallel with site directed mutagenesis studies, indicate that the active site Zn is in a cys-cys-his-H_2O environment, very different from the mammalian carbonic anhydrase active site. Nitrogenase, the primary enzyme in biological nitrogen fixation, contains two complex metal clusters of unique structure. Only recently has crystallography been able to propose models for these structures, but much more remains to be done. EXAFS studies at the Fe and Mo K-edges of nitrogenase solutions and crystals yielded information about the various metal-metal distances in these two clusters. We assigned 4 Fe and 3 Mo interactions <4 Å. Single crystal Mo K-edge EXAFS then found a very long Fe-Fe distance of ~5.1 Å. These distances were then used to further refine the proposed crystallographic models to their highest accuracy yet. Studies were carried further by examining nitrogenase in oxidized and

reduced forms - states for which there is no crystallographic information. Small structural changes were observed and we put forth an EXAFS model that attempts to deconvolute the EXAFS distances of the two metal clusters. This model illustrates a possible expansion of the metal-metal interactions during oxidation and contraction upon reduction. Nitrogenase Apo I, a genetic mutant of nitrogenase which is thought to contain only one of the two different metal clusters, was also examined using EXAFS. These studies showed results consistent with current models, yet the metal clusters were very disordered. Finally, I used ultra-low temperature methods to further the development of x-ray magnetic circular dichroism as a technique for studying biological systems. Experiments were performed on the copper in plastocyanin. Data was collected that definitively proves that the sample surface was at 0.55 ±0.05 K. This results opens the door to further study of more complex biological metal clusters.

Table of Contents

Chapter IX: Operation of the Ultra-Low Temperature ^{3}He Cryostat and 6-Tesla

Chapter X: X-Ray Magnetic Circular Dichroism at Temperatures < 1 K:

Demonstration with the Blue Copper Site in Plastocyanin

Acknowledgements

My time with the Cramer Group has been both educational as well as enjoyable. I have had positive interactions with so many people that I found this section harder to write than I had first thought.

First and foremost, I would like to thank Steve Cramer, for help and guidance, and also for hiring me. My being hired by him was almost accidental, but it has paid off for me immensely. Going over all of my work in preparation for writing this dissertation, I can see how far I have come. I have learned more than I ever would have imagined. And for the fact that I am writing this dissertation now, I will always be grateful to Steve. He's my boss, and I also consider him my good friend. To make it to this point is one of the greatest thrills of my life, and I owe it to him. But he still owes me money.

In the last two years, I have seen several of my mentors leave. There are three former postdocs who taught me a great deal: Simon George, Jie Chen and Jan Van Elp. Simon George taught me about everything from

vacuum technique and EPR spectroscopy to bacterial genetics. I learned volumes from him, and he always took an interest in my progress. He could also keep me in stitches. He gave me great words of advice: "work hard, play hard and rest a lot". Jie Chen and I spent countless hours staying up all night at beamlines. It is with Jie that I first got to see my name in print. When I first started, Jie is the one who was charged with bringing me up to speed, so we spent a lot of time together. It was fun and scientifically fruitful. Jan Van Elp taught me much of what I know about UHV technique and the L-edge/XMCD experiment. I have to admit, the two of us had some volatile times, but I would be lying if I did not say that he was a strong influence in my experimental career. We may have had some bad moments, but several hours and several beers later, things would be alright.

Corie Ralston and I have been through some real gauntlets, including the infamous 'u4 trip'. Corie and I seem to both have a certain type of 'bent' personality, so she is fun to work with and talk to. She left me Oreos at Brookhaven once too, I've always remembered that. Corie also deserves thanks for helping to proofread some of the chapters in this dissertation. Melissa Grush is a terrific 'person to bounce ideas off of', and she's become my good friend and confidante. I always like to show her what I'm working on, she's a great critic (and man can she be tough sometimes). We've spent a lot of time at the Coffee House talking about the work we are doing, or just

generally complaining about things. I'd also like to thank Brenda Weiss for all her help and friendship, and lots of deep theological discussions. I really appreciate the time she had my birthday announced on the NSLS experimental floor. Xin Wang has always been the first person I go to when I need to know about L-edge and XMCD theory. We've also had some fun, late night discussions. When I began working on the XMCD experiment, I got the chance to learn from Gang Peng. Without his help, I could never have obtained the XMCD results I did. He and I went through some real 'high pressure' beamtime. Although we never worked together, Clay Randall and I spent a lot time 'not working'. It was always fun to go out and have a few drinks with Clay or hit the driving range.

There were others outside of the Cramer Group that have also had a strong influence on me. Graham George of SSRL has always been really good about explaining EXAFS analysis to me. He would tell me about new ideas and ways of looking at data - always updating me on his latest analysis software packages. When I started working on the ultra-low temperature experiments, I got to work with Anthony Young of EOLBNL. I'm still not quite sure why he was willing to put himself into the middle of such a tough experiment, but he never gave less than 110%. When I was collecting what would become the final data set for this dissertation, Tony stayed up with me for over 24 hours. He had to leave to go to a meeting! He was always willing

to discuss ideas. He and I would talk for hours when I was trying to design the shielding for the ^{3}He cryostat. Tony also put up with a lot of my ribbing him for being a 'fed'. While on the topic of the XMCD experiment, I should also say thanks to Roger Carr of SSRL for being so helpful at getting us set-up to use his EPU. He really worked hard to make sure that we got data, not because he had to, because he wanted to. When I spoke at an SSRL users' meeting, he came by just to hear my talk and learn about the data I collected. I would like to thank all the staff at SSRL and the NSLS who have helped me with my work the last couple of years.

One of the things I have missed as I moved away from EXAFS and into the XMCD experiment is working with Roland Tittsworth and Brian Hales. It was always great when I got to work with Roland at a beamline. It was fun and it was also good for me in that I could learn about other aspects of nitrogenase from the guy who made the samples. He helped me to see things from a colorful 'southern redneck' perspective. Seriously, he was great to work with and a good friend - we've had 5 publications with both our names on them and one about to be submitted. I want to thank Brian for giving us the opportunity to do all this and for being so helpful to me in the recent past with recommendations.

Finally, there is some family I want to acknowledge. I want to thank

Bobbi, Peter and Peggy for raising me and being great parents. For helping me through all these years. Helping me gain the abilities that got me to this point. An extra thanks to Peter for helping to proofread all my drafts. I'm sure it was a laborious and boring task, especially to one who isn't in this field, but it was invaluable to me.

All in all, it's been a good time.

Chapter I

X-Ray Absorption Spectroscopy

ABSTRACT

This chapter is an introduction to the techniques of x-ray absorption spectroscopy. There will be discussion of the Extended X-Ray Absorption Fine Structure and a brief discussion of soft x-ray L-edge absorption for 3d transition metals. These sections will lay the groundwork for the chapters that follow. The methods of data acquisition and use of synchrotron radiation will also be covered.

Introduction

Consider a beam of photons with intensity I_o passing through a material. A certain quantity of these photons will be absorbed by the sample in accordance with the well known relation:

$$I = I_0 e^{-\mu(E)t}$$

where I is the intensity of photons emerging from the sample of thickness t and $\mu(E)$ is the absorption coefficient of the sample at a given photon energy E. The processes by which light is absorbed generally depend on the energy of the incoming photons. In the case of IR and UV/VIS techniques, photon energy is absorbed by exciting rotational-vibrational and valence electronic states. In the case of x-ray energies, photons are absorbed by exciting core electrons into valence and continuum states.

From quantum mechanics, the probability of a transition from an initial state to a final state is proportional to the square of the matrix element:

$$P_{if} \propto \left| \langle \psi_i | \hat{r} | \psi_f \rangle \right|^2$$

and by the Pauli exclusion principle, the final state, $|\psi_f\rangle$, must be unoccupied. If the x-ray photon has energy just below the binding energy of a core electron, an absorption event is not possible. If the photon energy is at, or greater than, the core electron binding energy, the probability is very large and absorption will occur. When the energy of the photon is near the binding energy the

absorption cross section will be greatest, and will decay as energy increases.

The absorption event promotes a core electron (the photoelectron) into an unoccupied valence state or, if the photoelectron has sufficient energy, into continuum states. What one then sees for the x-ray absorption coefficient is a series of 'edges' as illustrated in Figure 1. The notation used for these edges relates to the energy level of the photoelectron ejected: a K-edge corresponds to a 1s photoelectron, L_1 to 2s, L_2 and L_3 to the spin-orbit split $2p_{1/2}$ and $2p_{3/2}$ levels, etc.

There are two formalisms which describe the final states available to
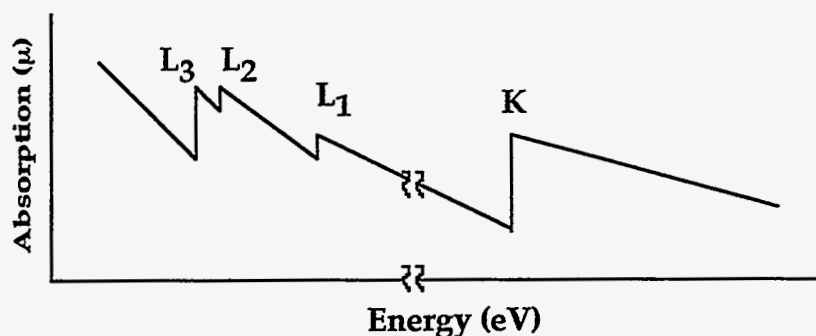
Figure 1: Illustration of the x-ray absorption edges. The L_3 and L_2 are only separated by the 2p spin orbit coupling. The K-edge is separated from the L_1 edge by the difference between 1s and 2s energy levels which is comparatively large.

the photoelectron and hence the structure in the x-ray absorption coefficient. In the vicinity of the absorption edge, where the photoelectron is not very energetic, it is useful to use an atomic multiplet model to calculate the available final states [1]. In the case of a more energetic photoelectron (~20-40

eV above the binding energy) it is more useful to consider the scattering from nearby atoms [2].

Extended X-ray Absorption Fine Structure (EXAFS)

When the ejected photoelectron has sufficient energy to escape the partially-bound valence states of the absorbing atom, it will then interact with the potentials of nearby atoms. This scattering gives rise to structure above the absorption edge. The photoelectron wave propagates out and scatters off
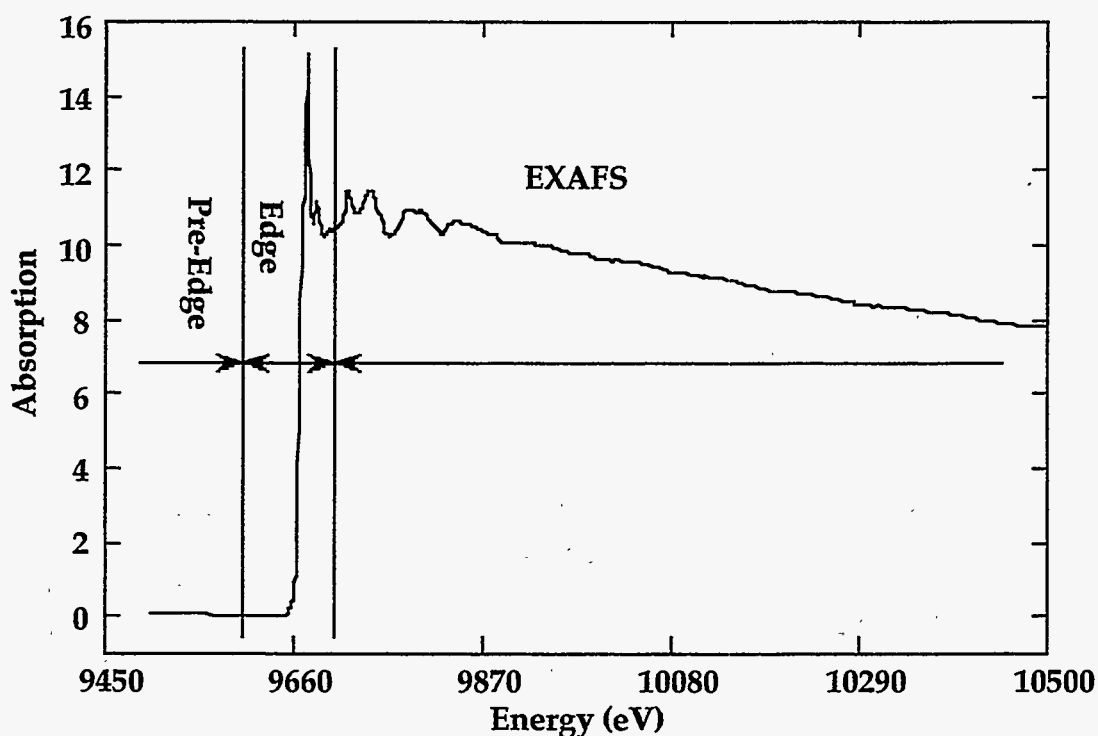
Figure 2: The K-edge spectrum of a Zn metal foil. The three regions are indicated (pre-edge, edge and EXAFS). The EXAFS Structure above the edge is clearly visible.

of the potentials of nearby atoms, generating backscattered waves. As the energy of the incoming photon beam is scanned, these waves interact. As

they move in and out of phase with each other, oscillations are set up in the absorption coefficient. These oscillations are referred to as the Extended X-Ray Absorption Fine Structure or EXAFS.

Shown in Figure 2 is a K-edge absorption spectrum for a Zn metal foil. This figure defines the three regions of an x-ray absorption spectrum. The 'pre-edge' region of the spectrum is dominated by absorption from the sample matrix. This slowly varying baseline will be used to subtract background contributions to the EXAFS during analysis. The 'edge' region is where the core photoelectron is promoted to unoccupied valence states and strongly localized on the absorbing atom. It is this region that can be treated with the multiplet model, as will be briefly discussed later. Finally, the structure above the edge is the EXAFS region.

The EXAFS consists of two parts: the oscillatory, or modulated part, and the smooth, or unmodulated part. The unmodulated portion is directly proportional to the photoabsorption that would be observed for a free atom. The modulated portion of the EXAFS is due to the interaction with neighboring atoms and contains the local structure information. These modulations can then be described by:

$$\chi(k) = \frac{\mu - \mu_0}{\mu_0}$$

where μ is the modulated part and μ_0 the unmodulated baseline. In practice,

the falloff observed in the EXAFS region is influenced by various experimental factors. As a result of this, an artificial approximation to this baseline must be made. Frequently, this is accomplished by fitting a cubic spline to the unmodulated part of the EXAFS. The above equation then becomes:

$$\chi(k) = \frac{\mu - \mu_{spl}}{\mu_0}$$

Which is the experimental form of the EXAFS oscillations.

When the ejected photoelectron has sufficient energy, the final state wave function for the absorption probability can be modeled by a single scattering formalism [2]. If the electron energy is not high enough (in the edge region), the interfering waves cannot be treated individually. The contributions of other atomic potentials to the outgoing and backscattered waves must be considered. This type of interaction is dominant in the edge region of the spectrum and can be treated with multiple-scattering methods. With a core electron initial state and scattered final states, it can be shown that the functional form of the EXAFS is [2]:

$$\chi(k) = \sum_i \frac{N_i \gamma_i f_i(k, R_i)}{k R_i^2} e^{-2\sigma_i^2 k^2} e^{-(\frac{2R_i}{\lambda})} \sin[2kR_i + \phi_i(k, R_i)]$$

where the summation is over the different absorber-backscatterer interactions. Although x-ray data is usually collected as a function of photon

energy, the equation above is in terms of the variable k. This is the magnitude of the photoelectron wave vector, as defined by the well known equation:

$$k = \left[\frac{8\pi^2 m_e}{h^2} (E - E_0) \right]^{1/2} \simeq [0.262(E - E_0)]^{1/2}$$

Expressing the function in terms of k brings the EXAFS into a space where the oscillations are periodic. More importantly, the energy difference in the above equation also allows photoelectron energy to be described by the amount of excess energy above the edge threshold that it possesses.

The overall nature of the EXAFS is that of a sum of exponentially decaying sine waves. The amplitude in the leading term is proportional to the number of atoms, N, (frequently referred to as the coordination number) at a given distance R. The distance and energy dependence in this leading term limit EXAFS analysis to local structure examinations: as distance and energy increase, the amplitude of the signal decreases quickly. The factor, γ, accounts for intrinsic processes in the system that reduce the EXAFS amplitude, such as multi-electron excitations. The exponential in terms of λ accounts for the fact that the photoelectron has a finite mean free path. This finite mean free path also limits the EXAFS to local structure.

The second exponential attenuation factor is in terms of σ^2, the so-

called Debye-Waller factor. For a given system, there will be a certain displacement in the atomic positions from thermal and static disorder. If the displacements are relatively small and have harmonic character, a gaussian distribution results, as is shown here. In this case, σ is the root mean square deviation for a given distance R. Although this is the generally accepted disorder model to use, there are cases where asymmetric distributions warrant a modification to this term [4].

The functions $f(k,R)$ and $\phi(k,R)$ are the backscattering amplitude and phase functions respectively. These functions are different for each absorber-backscatterer combination and are primarily responsible for the ability of EXAFS to determine the nature of individual backscatterers. The functions depend on the distance to the neighboring atom and also on the energy of the photoelectron wave. This energy dependence of the phase shift $\phi(k,R)$ as well as the angle, 2kR, means that the sine term in the EXAFS equation is not truly periodic.

Thorough calculations have been done to tabulate the phase and amplitude functions for atomic species. These tables can then be applied to unknown systems being studied. Another method is to determine the phase and amplitude functions for a particular absorber-backscatterer combination in a well defined compound. These phase and amplitude functions can then be applied to the unknown system currently under study. This brings up the

important issue of phase transferability. Can the phases for one system be applied to another different system? In general, there is good agreement when the phase and amplitude functions are transferred between different systems. However, what may need to be modified for different systems is the value of the threshold energy E_0. The valence energy levels are strongly dependent on the local surroundings. For this reason, small shifts in the threshold energy, ΔE_0, are added to each interaction in the EXAFS analysis to allow for transferability of the phase and amplitude functions. Methods now exist where *ab initio* calculations can be performed for a given system [6]. Analysis using these techniques can be somewhat cumbersome, since each interaction is calculated, refined and then re-calculated at the new refined values. Although it has been shown that using these *ab initio* calculations can lead to better fit quality, the errors in the distances, R, are still very small ($\sim\pm0.02$ Å [7]) when using tabulated phase and amplitude functions.

The use of EXAFS to gain local structural information from biological samples is well established [5]. The element specificity inherent in the technique allows an experimenter to observe local structure around a given site. Information about the type and number of neighbors surrounding the given element can be derived as well as distances to great accuracy (±0.02 Å [7]). Similar information can be gained from x-ray crystallography, but EXAFS has the advantage of not requiring ordered samples. This allows EXAFS studies of a broad range of samples where crystals have not yet been grown.

The ability to gain high accuracy distance information allows refinement of crystallographic models and the ability to observe small changes in metal-ligand distances.

Soft X-Ray L-edge Spectroscopy

Although not emphasized earlier, there are features present in the edge region of an XAS scan that can be important for learning more about the given system. This is the region of the spectrum where direct calculation of possible final states is appealing. Unfortunately, in many cases the edge features are much too broad or convoluted to perform an accurate analysis.

In the case of the 3d transition metals, an almost fourfold improvement in resolution can be gained by examining the L-edge absorption. This resolution allows the observation of spectral features which would be unresolvable in analogous K-edge studies. In the case of transition metals, the $L_{2,3}$ edges arise from transitions directly into the 3d metal valence orbitals, transitions which are formally dipole-forbidden in K-edge spectra. These orbitals contain important information about the symmetry and electronic structure of the metal and its environment.

The effect of the linewidth narrowing is demonstrated for $MnCl_2$ in Figure 3. The dipole forbidden 1s->3d transition is seen as an almost totally unresolvable doublet at the foot of the Mn K-edge. The presence of this
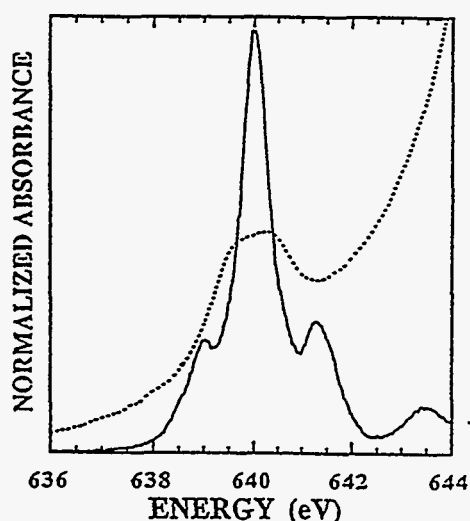
Figure 3: Comparison of the Mn K-edge (dashed) and Mn L_3-edge (solid) XAS spectra for $MnCl_2$. The energy scale is for the Mn L_3-edge. The spectra have been arbitrarily aligned and only the 1s->3d region of the Mn K-edge is shown.

feature can be explained by some 4p-character mixing into the 3d Mn orbitals and quadrupole allowed transitions. In contrast, the overlayed Mn L_3-edge shows much more structure from the dipole allowed 2p->3d transition.

For the case of $L_{2,3}$ edge absorption (still considering only 3d transition metals) the electron is promoted from the 2p shell into the valence 3d shell. For metals later in the periodic table, or for K-edge transitions, the interaction between the remaining core hole and valence electrons can be ignored. For the 3d transition metals, a proper description of the final state must take this 2p hole into account. The nature of these final states make them readily calculable using an atomic multiplet model [1,8].

For the calculation, the initial transition considered is $2p^6 3d^n$ ->

$2p^5 3d^{n+1}$, which is only a single L-edge transition. The 2p electron is ejected, the spin-orbit coupling of the core hole splits the 2p orbitals into $2p_{1/2}$ and $2p_{3/2}$. This splitting gives rise to the separate L_3 and L_2 edges. Once in the final state, the coulomb and exchange interactions of the electron with other d-orbital electrons is considered as well as any interaction with the 2p core hole. The allowed transitions are then calculated for this idealized system. To make the simulation more complete, the effect of the external crystal field is then folded in. This modifies the allowed transitions further, based on the symmetry of the absorbing atom. Finally, the broadening effects of lifetime and experimental error are used to broaden the transitions and a spectral simulation results.

XAS Data Collection

It would seem that the easiest way to collect XAS data is to set-up a traditional transmission experiment. The incident and transmitted beam could be measured and the resulting spectra analyzed. Unfortunately, this is not the case for biological samples. Metalloprotein solutions are generally very dilute (~mmolar in metal content). Revisiting the transmission relation gives:

$$I = I_0 e^{-(\mu_b + \mu_e)t} \quad , \quad \mu = \mu_b + \mu_e$$

where the absorption coefficient has been separated into contributions from the background absorption by the sample (μ_b) and the absorption of the

specific element being examined (μ_e). When the concentration is low, the

contribution of the background absorption will dominate. This results in a

very small signal on top of a large, slowly varying background. To overcome

this problem, dilute protein XAS is measured using fluorescence detection [9].

For this method of detection, a detector is tuned to collect only emission from

a specific element. This almost completely eliminates the background

contribution to the collected data. To maximize this method, multi-element

array detectors have been developed to collect as much of the fluorescence

signal as possible and maximize the signal to noise ratio [10].
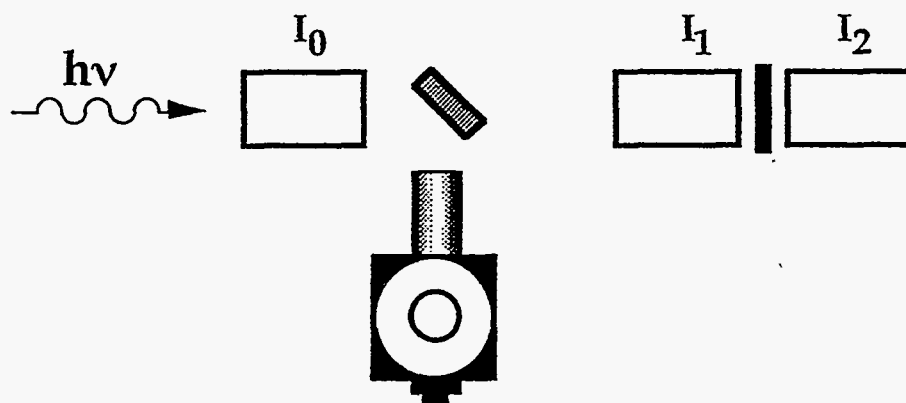
Figure 4: Rough diagram of the experimental XAS set-up. The beam is entering as hv and is monitored by I_0. The cooled sample is rotated at 45° to the fluorescence detector and incoming beam. For the hard x-ray experiments, an internal calibration can be used by placing I_1 and I_2 behind the sample.

A typical XAS experiment is shown schematically in Figure 4. In the

case of x-ray energies above ~3 keV (i.e. the K-edges of the 3d transition

metals), the experiment is performed in atmosphere. The beam intensities

(I_0, I_1 and I_2) are measured using gas ionization chambers placed in the beam path. The sample is usually cooled to cryogenic temperatures (~5-20 K) to minimize radiation damage and reduce the broadening effects from thermal disorder. The sample is oriented at 45° to the incident beam and the fluorescence detector.

The two extra gas ionization detectors are used to calculate an internal calibration. Since a portion of x-rays in this energy range will still transmit through the sample, a classic absorption experiment is run using a concentrated standard sample (i.e. a pure metal foil between I_1 and I_2). For each fluorescence scan of the protein being studied, an accompanying scan is made of the well characterized standard. This allows for very accurate energy calibration to be performed during data analysis.

In the case of soft x-ray experiments (i.e. the L-edges of 3d transition metals, <1 keV) the experiment must be conducted in vacuum. Soft x-rays have very short penetration depths and would be completely absorbed if an air path was used. In order to optimize the photon flux on the sample, soft x-ray beamlines operate in a 'windowless' mode. In this condition, the vacuum chamber connects directly to the beamline and ring vacuum. Fluorescence detectors have been developed that share this vacuum eliminating the need for absorbing windows over the detector elements [11].

Unfortunately, since the penetration depth is so small at these soft x-ray energies, the use of an internal calibration standard is impossible. Measurements must be alternated between the sample of interest and a well characterized standard. The measurement of beam intensity must also be relatively non-invasive. Usually, thin metal grids are placed into the vacuum to measure beam intensity. The porous nature of the grid allows much of the incident light to pass through while a fraction of the beam will excite an electron current in the metal that can be monitored externally.

Synchrotron Radiation

In order to perform these experiments, a continuously tunable source of x-rays must be utilized. The source must also be able to reach a very wide range of x-ray energies. The experiments in this thesis span a range of ~900 eV for the Cu L-edge to 21000 eV for Mo K-edge EXAFS. The best means of accomplishing these goals is to use synchrotron radiation.

When a very high energy electron ($E >> mc^2$) is deflected in a magnetic field, the energy released is synchrotron radiation. The energy lost to synchrotron radiation was originally a problem in high energy physics experiments and early studies of synchrotron radiation were designed to mitigate this energy loss. However, as scientists have found ways to study smaller and smaller structures, synchrotron radiation has moved from being an unwanted byproduct to a position where storage rings designed solely to

deliver high quality synchrotron radiation are being built all over the world. Now, there are dedicated synchrotron facilities which can deliver photons from the infrared energy range (10^{-2}-1.8 eV) to the hard x-ray regime (10^3-10^5 eV) [3].

A synchrotron storage ring consists of bend and straight sections (Figure 5). At each of these bends, the electron path is deflected by a magnetic
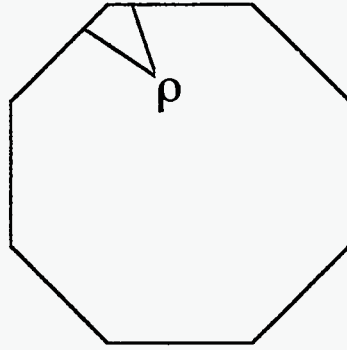
Figure 5: Schematic diagram of a synchrotron storage ring. It is apparent that the structure is not a true ring shape, but a closed path consisting of bend and straight sections. The radius of curvature is defined by each bend, as is indicated by ρ.

field and radiation is released. The spectral output of the electrons passing through one of these bend magnets is given by [3]:

$$N(h\nu) \propto \gamma(y) \int_{y}^{\infty} K_{2/3}(t) \; ; y = \left[\frac{h\nu}{h\nu_c} \right] \; ; h\nu_c = \frac{3hc\gamma^3}{4\pi\rho}$$

Where $K_{2/3}(t)$ is a modified Bessel function of the second kind and γ is the relativistic ratio (E/mc). This equation also introduces an important quantity for describing synchrotron radiation, the critical energy $h\nu_c$. The equation above is plotted for several different electron beam energies in the SPEAR ring at the Stanford Synchrotron Radiation Laboratory in Figure 6.

The general shape is one of a steady incline to a peak and then a sharp decline. Notice how the output energy range increases with an increase in the energy of the stored electron beam. Although the critical energy is located near the falloff point in the curve, there is still flux available beyond this point. Knowledge of the critical energy is then useful for gaining knowledge about the output of a synchrotron ring. For the SPEAR ring plotted in Figure 6, a 1 GeV electron beam will output better in the soft x-ray region of the spectrum (< 1 keV) while the 4 GeV electron beam will be a good emitter of hard x-rays (10^3-10^5 keV). The values along the y-axis of Figure 6 also give some insight into the high flux available from synchrotron radiation. Where classic x-ray tubes could deliver 10^{6-8} photons/sec, synchrotron bend magnets can deliver 10^{10-13} photons with a small focussed beam size [3].
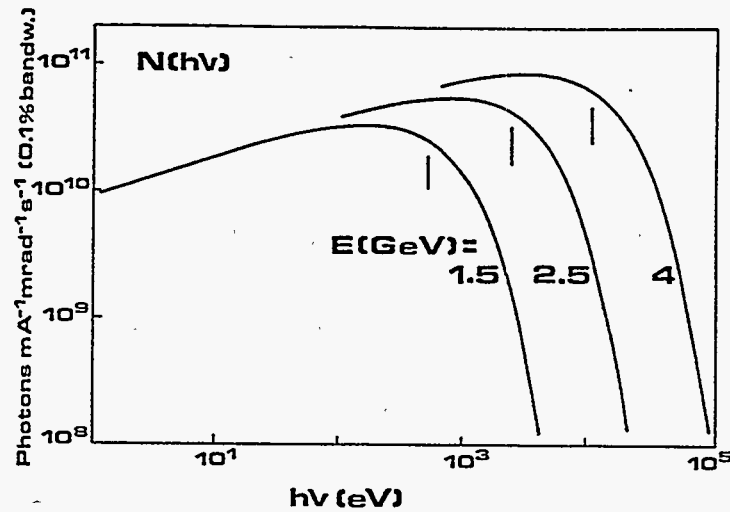
Figure 6: Spectral distribution of radiation emitted by the SPEAR storage ring. The curves are drawn for the three different electron energies shown. The vertical lines correspond to the critical energy points for each curve. From ref [3].

The relationships just discussed show the relationship of spectral output to the characteristics of the ring bend magnets (radius of curvature, ρ; ring energy, γ), but what of the straight sections? By arranging two rows of magnets in one of the ring straight sections, the electron beam can be perturbed several times with a small radius of curvature. This will produce radiation of higher intensity than a single bend magnet. This is the principle behind 'insertion devices' which are placed in the ring lattice and produce very high photon flux.

In a wiggler insertion device, the magnetic fields are generally small and the photon flux output is extremely high due to the number of different magnet periods that the electrons travel through. In the case of an undulator, the fields are usually higher and the number of magnetic periods can also be

greater. In this case, the interference effects in the output light cannot be ignored. These effects cause the spectral output of an undulator to be extremely bright light concentrated around a small range of energies. By changing the gap between the magnet rows in an undulator, and hence the magnetic field the electron beam sees, the position of this sharp energy peak can be moved. This allows the experimenter to 'tune' the energy of the undulator to conform to the requirements of the experiment being performed.

References

(1) A good discussion of soft x-ray absorption of 3d transition metals with a simple application: DeGroot, F.M.F.; Fuggle, J.C.; Thole, B.T.; Sawatzky, G.A. *Phys. Rev. B* **1990**, *41*, 928.

(2) Very good, but somewhat complex, derivation of EXAFS: Stern, E.A. in *X-Ray Absorption: Principles, Applications and Techniques of EXAFS, SEXAFS and XANES*, (Koningsberger, D.C., Prins, R., Eds.), **1988**, John Wiley & Sons, New York, pp 3.

(3) A good introductory treatment to synchrotron radiation: Margaritondo, G. *Introduction to Synchrotron Radiation*, **1988**, Oxford University Press, New York.

(4) Two nice treatments of asymmetry and anharmonicity in EXAFS: (a) Eisenberger, P.; Brown, G.S. *Sol. State Comm.* **1979**, *29*, 481. (b) Crescenzi, M. De; Balzarotti, A.; Comin, F.; Incoccia, S.; Mobilio, S.; Motta, N. *Sol. State Comm.* **1981**, *37*, 921.

(5) Good, but somewhat dated, overview of biological EXAFS studies: Cramer, S.P in *X-Ray Absorption: Principles, Applications and Techniques of EXAFS, SEXAFS and XANES*, (Koningsberger, D.C., Prins, R., Eds.), **1988**, John Wiley

& Sons, New York, pp 257.

(6) Description of the program FEFF, developed to perform multiple scattering and *ab initio* phase calculations: (a) Rehr, J.J.; Mustre de Leon, J.; Zabinsky, S.I.; Albers, R.C. *J. Am. Chem. Soc.* **1991**, *113*, 5135. (b) Mustre de Leon, J.; Rehr, J.J.; Zabinsky, S.I.; Albers, R.C. *Phys. Rev. B* **1991**, *44*, 4146.

(7) Mentions the error bars, also a good EXAFS review: Lee, P.A.; Citrin, P.H. Eisenberger, P.; Kincaid, B.M. *Rev. Mod. Phys.* **1981**, *53*, 805.

(8) Another good L-edge theory discussion: DeGroot, F.M.F.; Fuggle, J.C.; Thole, B.T.; Sawatzky, G.A. *Phys. Rev. B* **1990**, *42*, 5459.

(9) The classic demonstration of the uses for fluorescence detection: Jaklevic, J.; Kirby, J.A.; Klein, M.P.; Robertson, A.S.; Brown, G.S.; Eisenberger, P. *Sol. State Comm.* **1977**, *23*, 679.

(10) Cramer, S.P.; Tensch, O.; Yocum, M.; George, G.N. *Nucl. Instrum. Methods* **1988**, *A266*, 586.

(11) Cramer, S.P.; Chen, J.; George, S.J.; VanElp, J.; Moore, J.; Tensch, O.; Colaresi, J.; Yocum, M.; Mullins, O.C.; Chen, C.T. *Nucl. Instrum. Methods* **1992**, *A319*, 285.

Chapter II

Spinach Carbonic Anhydrase: Investigation of the Zinc-Binding Ligands by EXAFS[1]

ABSTRACT

A good demonstration of the EXAFS technique applied to biological systems is this study of plant carbonic anhydrase (for reference to complete study, see chapter footnote). The enzyme carbonic anhydrase has been well characterized in mammalian systems, but the structural properties of the plant isozymes remain elusive. To investigate the nature of the zinc-binding site in spinach carbonic anhydrase, we targeted potential zinc binding ligands for mutagenesis and examined resulting enzymes for catalytic activity and stoichiometric zinc binding. We then examined the wild-type protein using extended X-ray absorption fine structure (EXAFS) analysis to try and gain

information about the local surroundings of the zinc active site. Overall analysis of the results suggest that spinach carbonic anhydrase utilizes a Cys-His-Cys-H_2O ligand scheme to bind zinc ion at the active site.

Introduction

Carbonic anhydrase (CA, sometimes referred to as carbonate dehydratase) is a ubiquitous zinc metalloenzyme which catalyzes the reversible hydration of carbon dioxide. In mammals, CA plays important roles in facilitating carbon dioxide exchange in capillary beds and alveoli, maintaining the buffering capacity of blood, and reabsorbing bicarbonate across renal tubules [1]. Crystal structures for the human isozymes I and II and the bovine isozymes II and III have been solved, and they show that these enzymes coordinate an active-site zinc through three conserved histidine residues [2].

In higher plants which carry out C_3 photosynthesis, the majority of CA activity can be localized to the chloroplast stroma where the enzyme's role is unclear, although it may serve to concentrate carbon dioxide at the active site of ribulose-1,5-bisphosphate carboxylase/oxygenase [3]. CA from higher plants is quite different from the major mammalian isozymes in both primary sequence and multimeric assembly. CA from C_3 dicotyledonous plants is a hexamer with one zinc atom per monomer [3,4] which the major mammalian isozymes are monomeric [5]. Furthermore, sequence analysis reveals no homology between the plant and animal CA's, and this suggests that the animal and plant isozymes do not share a common evolutionary origin [6] and therefore may not share common physical properties.

Until a crystal structure becomes available for a plant-type CA, biochemical investigations may provide hints of structural characteristics of this enzyme. To this end, we have employed techniques of molecular biology and biophysics to investigate the nature of the zinc-binding site in spinach carbonic anhydrase. Here I will present results of experiments utilizing EXAFS analysis done in parallel with site-directed mutagenesis and elemental analysis.

Experimental

Sample Preparation. The complete discussion for the site-directed mutagenesis sample preparation as well as the sample preparation for elemental analysis is in the reference shown in the chapter footnote. For the EXAFS samples, wild type CA was purified and then, in order to remain consistent with samples generated for the mutagenesis, fused to the carboxyl terminus of *Staphylococcus* protein A to form a CA/A sample. This CA/A fusion protein was examined for activity and used as a control in the metal analysis. The acitivity of all samples was measured using photometric methods previously described [7].

The wild type A/CA fusion protein was purified from 50 g of cell paste. Protein was concentrated using Minicon-B15 clinical sample concentrators (Amicon) to a final concentration of ~2 mM and supplemented with 30% ethylene glycol; 80 µl samples were loaded into lucite cells with a 1mm path

length and sealed with 0.001 inch Kapton tape.

Data Collection. X-ray absorption spectra were recorded at the National Synchrotron Light Source, Brookhaven National Laboratory, on beamline X10-C. The beamline was run in the focussed mode with a Si(111) double crystal monochromator configuration. Higher order harmonics were rejected using a mirror position feedback system [8]. Frozen samples were loaded into an Oxford Instruments liquid helium flow cryostat maintained at ~10 K. XAFS data were collected in the fluorescence mode using a Canberra Industries 13-element Ge solid-state array detector [9] while incident beam intensity was monitored with a nitrogen filled ion chamber. Photon energy was calibrated by simultaneously collecting a transmission spectrum of a zinc metal foil and setting the first inflection point energy to 9659.0 eV.

Analysis Procedures. EXAFS oscillations were extracted from the raw data by routine methods [10] and were then quantitatively analyzed using a Levenberg-Marquardt non-linear least-squares calculated curve-fitting procedure to minimize the differences between the data and observed EXAFS [11]. Simulations were derived from the curved-wave functional form:

$$\chi(k) = \sum_i \frac{N_i \gamma f_i(k,R_i)}{kR_i^2} e^{-2\sigma^2 k^2} \sin[2kR_i + \phi_i(k,R_i)]$$

For this analysis, theoretical values for both phase and amplitude were used

[12] and γ, which represents intrinsic losses to EXAFS signal, was held fixed at 0.9 during all fits. During fitting, the total Zn coordination was set to four or five, and small changes in the threshold energy, ΔE_0, were fixed at -4.2 eV [13]. The interatomic distance (R), and mean square deviation of R (σ^2) were allowed to vary.

Results and Discussion

Sequences for CA expressed in *E. Coli* [14] as well as sequences from Synechococcus [6], Arabidopsis [15], peas [16], spinach [17], tobacco [18] and barley [19] were analyzed for conservation of the amino acids whose side chains are potential zinc ligands based on other enzyme active sites [20]. Homology alignments showed that one histidine, two cysteines, two glutamates and one aspartate are conserved among the plant-type CA's.

Prior to EXAFS analysis, site directed mutagenesis was used to change each of these six residues and obtain proteins expressed in *E. Coli* with modified activities (Table I). These mutated CA/A proteins, along with a wild type CA/A control sample were then examined using inductively coupled plasma emission atomic absorption spectroscopy (ICP-AES) after removal of any adventitious zinc. Of the six mutants generated, the two cysteine modifications (C150A, C213A) and one histidine (H210Q) had a greatly diminished capacity to bind zinc and exhibited lower activity (Table I).

Table I: Activity and Zinc Binding to Mutants of Spinach Carbonic Anhydrase

mutant	enzyme activity		mol Zn/ mol CA
	EPPS	imidazole	
W T	100	100	1.09
C150A	ND[b]	9	0.03
D152N	1	9	0.81
E194Q	22	5	0.80
H210Q	10	6	ND[b]
C213A	6	5	0.15
E266Q	81	100	1.25

[a] Activities expressed as percentage of wild type (WT), averaged for four to five independent assays and two protein preparations.
[b] not detectable.

To further investigate the structure of the active site of CA, the wild type spinach protein was examined using XAS. EXAFS has the advantage of providing a direct examination of the zinc local environment. The CA Zn K-edge EXAFS is relatively strong and without a clear beat pattern (Figure 1, left). The Fourier transform is dominated by a single peak centered at ~2.3Å with a few minor peaks above the noise between 3 and 4 Å (Figure 1, right). The pattern is similar to transforms observed in EXAFS studies of plastocyanin and other blue copper proteins [21].

The dominant feature in the transform could be simulated by a Zn-S interaction at ~2.3Å, but additional Zn-N/O interactions near 2Å were necessary to get a good fit. Unfortunately, EXAFS resolution does not allow

us to discern between light ligands such as nitrogen and oxygen. The small features present beyond the central 2.3Å peak are most likely due to multiple scattering interactions from an imidazole group and some contributions from
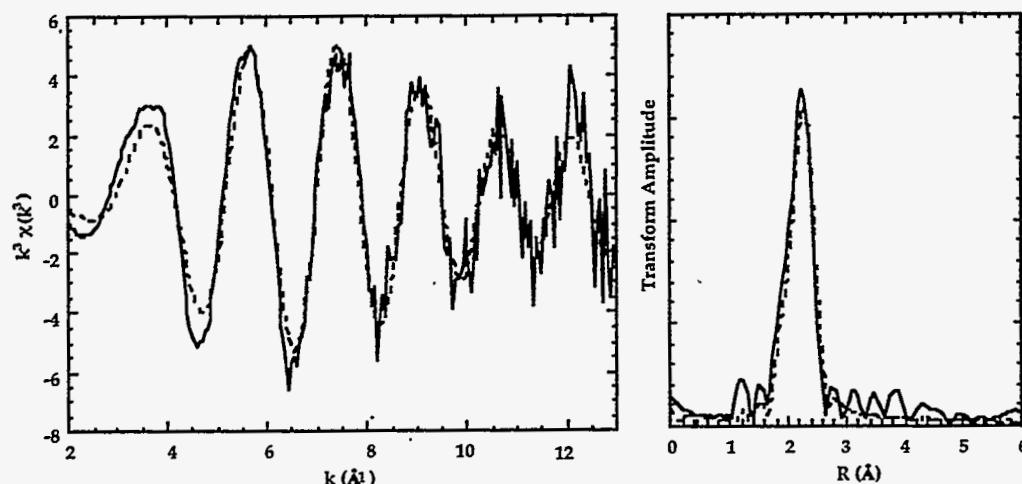
Figure 1: Results of EXAFS curve fitting analysis. *(left)* Experimental k^3 EXAFS (solid) with best fit results for a 2 Zn-S and 2 Zn-N/O model (dashed). *(right)* Fourier Tranforms of the experimental EXAFS (solid) and best fit (dashed).

the carbons of the cysteines. Unfortunately, with little knowledge of the symmetry and geometry of the site, attempts to unambiguously fit these features have not been successful. The quality of fitfor all possible combinations of sulfur and nitrogen/oxygen interactions was judged by comparing the fit index between resulting fit and the raw extracted EXAFS, these results are summarized in Table II.

Analysis of the EXAFS of spinach carbonic anhydrase yields evidence that the nearest neighbors of the zinc are sulfur and nitrogen/oxygen species. Of the five possible combinations of two distinct Zn-S and Zn-N/O

interactions in a four ligand system, 2 Zn-S and 2 Zn-N/O gives the best fit, in agreement with mutagenesis and ICP-AES results. This model represents a 20% improvement in fit index over the next lowest value (Table II). It is clear that a model with four N/O ligands coordinated to Zn, as found in mammalian CA systems, is not consistent with the EXAFS since the corresponding fit is of much worse quality than the others performed on this system. Attempts to fit a longer N/O shell at ~2.3Å were also unsuccessful, yielding fit indices of ~10^4 or causing the second Zn-N/O distance to contract back to ~2.1Å, giving the same result as the 4 N/O model. Furthermore, the presence of only two conserved cysteines per polypeptide in the plant type CA's is consistent with our 2 Zn-S - 2 Zn-N/O model and renders the 3 Zn-S - 1 Zn-N/O and 4 Zn-S models improbable.

Since four separate CA mutants yielded enzymes with activities of 10% or less, we also examined the EXAFS data for the possibility of pentacoordinate zinc as implicated for adenosine deaminase [22]. The fit index resulting from addition of a third N/O ligand at ~2.0Å for a 2 Zn-S - 3 Zn-N/O does yield a 16% improvement over the 2 Zn-S - 2 Zn-N/O model. However, several lines of evidence discredit this five ligand model. First, the fit indices for the best tetracoordinate model and the pentacoordinate model lie within the usual error range placed on values of coordination derived using the EXAFS technique. Therefore, it is objectively impossible to favor one model or the other based purely on EXAFS results. Second, when a

tetracoordinate zinc is converted to a pentacoordinate one in synthetic systems, the bond length of the leaving group is longer than the other four remaining bond lengths by up to 0.26 Å [23]. We can find no such asymmetry in the CA pentacoordinate model with the current data; all N/O bond lengths converge to the same average distance. Third, only three of the mutants tested showed strongly diminished capacity to bind zinc. It is, however, possible that the fifth ligand is not directly bound to zinc, but close enough to be evident in the EXAFS while not affecting the ability of the active site to bind zinc.

Table II: Results of EXAFS Curve Fitting Analysis

	model	N	R (Å)	σ^2 ($\text{Å}^{2}*10^{-3}$)	Fit Index[a] F
4 ligands	Zn-S	4	2.31	6.29	314
	Zn-S	3	2.32	4.08	
	Zn-N/O	1	2.04	1.35	212
	Zn-S	2	2.32	2.03	
	Zn-N/O	2	2.06	3.02	171
	Zn-S	1	2.32	1.00	
	Zn-N/O	3	2.08	5.09	255
	Zn-O/N	4	2.11	4.90	777
5 ligands	Zn-S	2	2.32	2.37	
	Zn-N/O	3	2.06	5.63	143

[a] $F=[\Sigma(\chi_e-\chi_s)^2 k^6]$. where χ_e represents the experimental data points and χ_s the simulated EXAFS. All fits were performed on range k=2-13 Å^{-1}. During the fits, the total Zn coordination was held fixed at four or five and small changes in the threshold energy (ΔE_0) were fixed at -4.2 eV [22], while the interatomic distance (R) and mean square deviation in R (σ^2) were allowed to vary.

Summary

Examination of the sequences for several species of CA shows that there are six probable zinc ligands conserved in all the peptides. By targeting each of these ligands for mutagenesis and then examining the enzymatic activity and the ability to bind zinc, three ligands can be implicated as being zinc ligands in the active site. Using EXAFS to study the local zinc structure shows that the active site is most likely a tetracoordinate zinc with 2 Zn-S ligands and 2 Zn-N/O ligands formed by two cysteines, one histidine, and, as in the mammalian enzyme, the fourth ligand may be an activated water. EXAFS also shows that there is no structural similarity between the plant carbonic anhydrase and the mammalian carbonic anhydrase which consists of 4 Zn-N/O ligands.

References

(1) Tashian, R.E. *Bioessays* **1989**, *10*, 186.

(2) *for example, see:* Håkansson, K.; Carlsson, M.; Svensson, L.A. *J. Mol. Biol.* **1992**, *227*, 1192.

(3) Graham, D.; Reed, M.L.; Patterson, B.D.; Hockley, D.G.; Dwyer, M.R. *Ann. N.Y. Acad. Sci.* **1984**, *429*, 222.

(4) Kisel, W.; Graf, G. *Phytochemistry* **1972**, *11*, 113.

(5) Deutsch, H.F. *Int. J. Biochem.* **1987**, *19*, 101.

(6) Fukuzawa, H.; Suzuki, E.; Komukai, Y.; Miyachi, S. *Proc. Natl. Acad. Sci. U.S.A.* **1992**, *89*, 4437.

(7) Khalifah, R.G. *J. Biol. Chem.* **1971**, *246*, 2561.

(8) Sansone, M.; Via, G.; George, G.N.; Meitzner, G.; Hewitt, R.; Marsch, J. in X-ray Absorption Fine Structure, Hasnain, S.S. ed.; Ellis Horwood, Ltd.:W. Sussex, England, 1991; pp 656-658.

(9) Cramer, S.P.; Tench, O.; Yocum, M.; George, G.N. *Nucl. Instrum. Methods* **1988**, *A266*, 586.

(10) Cramer, S.P.; Hodgson, K.O.; Steifel, E.I.; Newton, W.O. *J. Am. Chem. Soc.* **1978**, *100*, 2748.

(11) Marquardt, D.W. *J. Soc. Ind. Appl. Math.* **1963**, *11*, 243.

(12) McKale, A.G.; Knapp, G.S.; Chan, S.-K. *Phys. Rev. B* **1986**, *B33*, 841.

(13) Hubbard, S.R.; Bishop, W.R.; Kirschmeier, P.; George, S.J.; Cramer, S.P.; Hendrickson, W.A. *Science* **1981**, *254*, 1776.

(14) Sung, Y.C.; Fuchs, J.A. *J. Biol. Chem.* **1988**, *263*, 14769.

(15) Raines, C.A.; Horsnell, P.R.; Holder, C.; Lloyd, J.C. *Plant Mol. Biol.* **1992**, *20*, 1143.

(16) Roeske, C.A.; Ogren, W.L. *Nucleic Acids Res.* **1983**, *18*, 3413.

(17) Fawcett, T.W.; Browse, J.A.; Volokita, M.; Bartlett, S.G. *J. Biol. Chem.* **1989**, *265*, 5414.

(18) Majeau, N.; Coleman, J.R. *Plant Physiol.* **1992,** *100,* 1077.

(19) Bracey, M.H.; Bartlett, S.G. *in preparation.*

(20) Vallee, B.L.; Auld, D.S. *Biochemistry* **1990,** *29,* 5647.

(21) Scott, R.A.; Hahn, J.E.; Doniach, S.; Freeman, H.C.; Hodgson, K.O. *J. Am. Chem. Soc.* **1982,** 104, 5364.

(22) Wilson, D.K.; Quiocho, F.A. *Biochemistry* **1993,** *32,* 1689.

(23) Auf der Hyde, T.P.E.; Nassimbeni, L.R. *Acta Crystallogr. Sect. B* **1984,** *B40,* 582.

Chapter III

An Introduction to the Nitrogenase Enzyme

ABSTRACT

The extreme complexity of the nitrogenase enzyme has made it the subject of extensive study from many approaches, yet many things about the enzyme's catalytic function still remain a mystery. This chapter will be a brief introduction to the structure and function of the nitrogenase enzyme system. It describes the current crystallographic models for the MoFe and Fe protein and the implications that these structures have on enzymatic activity. The foundations laid down by prior studies will also be discussed.

Introduction

Nitrogen is a requirement for all living things; it is one of the most abundant elements in the biosphere and is a prime component of the proteins and nucleic acids on which all life is based. Almost 80% of the air we breathe consists of nitrogen in the form of dinitrogen (N_2). With a strong triple bond, dinitrogen is an almost totally unreactive molecule. Higher animals and plants are incapable of utilizing nitrogen in the unreactive dinitrogen form, however, bacteria have evolved which can reduce atmospheric dinitrogen to a form readily assimilated by biological systems. In this process, atmospheric dinitrogen is 'fixed' and reduced to ammonia which is readily incorporated into biomolecules via the glutamate dehydrogenase and glutamine synthetase pathways [1].

The fixation process has an elaborate, and not yet fully understood, redox chemistry with a concurrent evolution of hydrogen [2]. In contrast with industrial ammonia production (which requires temperatures of ~500°C and pressures of ~300 atm.), this reaction occurs anaerobically under ambient temperature and pressure. The overall catalysis reaction is shown below:

$$8H^+ + N_2 + 8e^- + nMgATP \rightarrow n2ase \rightarrow 2NH_3 + H_2 + nMgADP + nP_i$$

This reaction is energy intensive, and studies indicate that no less than 16 ATP molecules are hydrolyzed to reduce one molecule of dinitrogen [3]. It has been estimated that symbiotic nitrogen fixing bacteria in the root nodules of pea plants consume almost one fifth of the total ATP produced by the plant

[1].

Nitrogen fixation is carried out by the nitrogenase complex, an enzyme system consisting of two protein components (Figure 1). The smaller of the two, the Fe protein, is a ~60 kDa γ^2 dimer containing an Fe-S cluster. The larger of the two proteins is a ~220 kDa protein known as the MoFe protein. The MoFe protein is an $\alpha_2\beta_2$ tetramer containing two metal clusters: an Fe-S 'P-cluster' and a Mo-Fe-S 'M-center'. Alternate nitrogenases have been isolated that contain V-Fe-S [4] and Fe-Fe-S [5] M-centers. Although the subject of intensive spectroscopic study, the structure of the MoFe protein and associated metal clusters remained a mystery until the recent advent of crystallographic models.
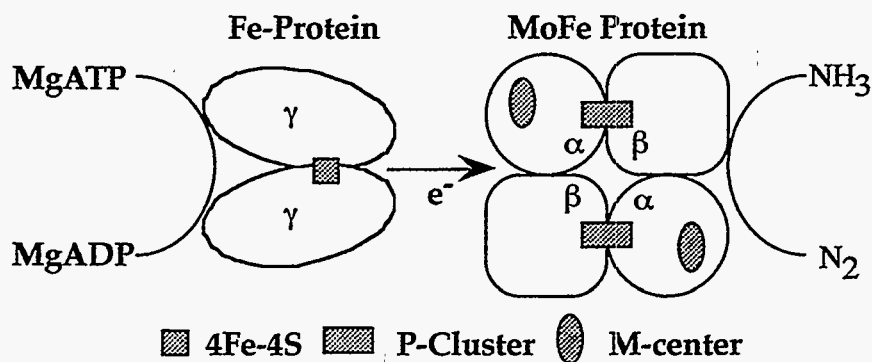
Figure 1: A schematic picture of the nitrogenase complex. The electrons come from a low potential reductant and enter the Fe protein. The Fe protein then reduces the MoFe protein, coupled with MgATP hydrolysis.

As isolated MoFe protein gives a characteristic S=3/2 EPR signal which has been shown to arise from the paramagnetic M-center [6]. Mössbauer

spectroscopy, combined with EPR results, provided a significant base for current our understanding of the nitrogenase metal clusters [7]. These studies found four different signals arising from Fe atoms in wild type MoFe protein. They assigned 8-10 Fe atoms to a paramagnetic 'M-center' which was associated with an S=3/2 EPR signal. Three other signals labelled 'D','S' and 'Fe^{2+}' did not show any paramagnetic activity and it was later proposed that they formed four 4Fe4S clusters in the MoFe protein [7]. Further electronic studies indicated that each P-cluster actually consisted of 2 magnetically coupled 4Fe4S cubes in an all ferrous configuration [8].

Prior to the crystal structure determination, the best source of high resolution structural information about the metal clusters was XAS spectroscopy. Mo K-edge EXAFS on isolated FeMo-cofactor, MoFe protein solutions and crystals found Mo-O/N, Mo-S and Mo-Fe distances of ~2.1 Å, ~2.4 and ~2.7 Å respectively [9-11]. Fe EXAFS on isolated FeMo-cofactor also exhibited a peak at ~3.7 Å assigned to an Fe-Fe interaction. Further EXAFS studies at the Fe and Mo K-edges of MoFe protein solutions and crystals will be discussed in chapters IV and V. Studies of reduced MoFe protein and a mutant nitrogenase will be discussed in chapters VI and VII.

Bolin and coworkers [12] put forth the first crystallographic model for the *Clostridium pasteurianum* MoFe protein to 5 Å resolution. Although this resolution was not sufficient enough to elucidate the atomic structure of

the metal clusters, important results were obtained. At this level, it was determined that the metals were arranged into two pairs of identical clusters in the $\alpha_2\beta_2$ tetramer; the M-center is situated inside the α subunit and the P-cluster lies across the $\alpha\beta$ interface. This model also provided further evidence that each P-cluster was composed of two coupled 4Fe4S clusters.

Crystallographic Models for Nitrogenase

A crystallographic structure of the Fe protein from *Azotobacter vinelandii* [13] has been proposed. The peptide structure has been described as having an 'iron butterfly' shape [14], similar to that shown in Figure 1. Coordinated by the two subunits is a 4Fe-4S cluster near the surface of the protein. Also in this cleft between the two subunits, and ~20 Å from the metal cluster, is a proposed site of nucleotide binding (one per γ subunit).

Two groups, working independently, have proposed structures for the nitrogenase MoFe protein. The overall $\alpha_2\beta_2$ structure of the peptide is formed by two $\alpha\beta$ dimers related by twofold symmetry. The M-center has been shown to consist of a 4Fe-3S fragment bridged by three inorganic sulfides to a 1Mo-3Fe-3S + homocitrate fragment [15-16] (Figure 2). This cluster can be extracted from the protein as the FeMo-cofactor or 'FeMo-co' [17]. Extensive spectroscopic study of this extracted cluster has shown that it has similar properties as the M-center [17]. Proteins which are FeMo-co deficient do not
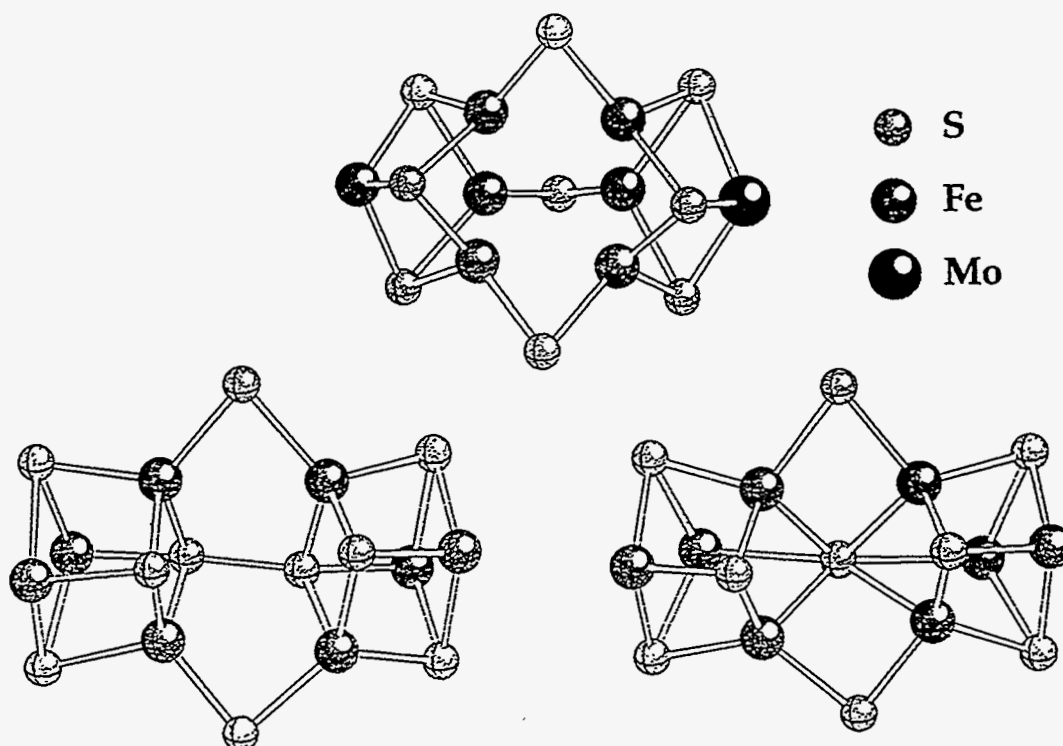
Figure 2: Proposed crystallographic models for the metal centers in the nitrogenase MoFe protein. *(top)* Proposed model for the Mo-Fe-S M-center. *(bottom)* Two proposed models for the Fe-S P-clusters. *(left)* The model proposed by Kim and Rees with a disulfide bond between the two cube fragments, *(right)* the model proposed by Campobasso and Bolin with a single sulfur between the two cube fragments.

exhibit nitrogenase activity, but can be reconstituted to an active form upon *in vitro* addition of FeMo-co. These studies, along with mutagenesis studies of the protein environment around the M-center [18], indicate that the M-center is almost certainly the site of substrate reduction. However, examination of the current crystallography has failed to identify the pathway for substrate access to the M-center. The proton donor source and hydrogen evolution site(s) have also not yet been determined.

The P-cluster lies on the interface of the αβ subunits. There is disagreement, however, as to the structure of this Fe-S cluster. One model proposed by Kim and Rees [15] is that of two 4Fe-4S cubes bridged by two inorganic sulfides and a disulfide bridge between the two cube corners (Figure 2). The model proposed by Campobasso and Bolin [16] is also two 4Fe-4S cubes with bridging sulfides, but they do not observe a disulfide between the two cube corners (Figure 2). Instead, they propose that the two cubes are fused by a single hexacoordinate sulfur.

Nitrogenase Activity

To reduce dinitrogen, both Fe and MoFe proteins must be present, as well as MgATP and a source of electrons. *In vivo*, electrons are donated to the nitrogenase complex via electron transfer proteins such as ferredoxins and flavodoxins [19]. For in *vitro* studies, dithionite is commonly used as the low potential reductant. Electrons enter the complex through the Fe protein and are delivered, one at a time, to the MoFe protein along with MgATP hydrolysis. Once in the MoFe protein, the electron transfer path becomes ambiguous. However, it has been speculated that the electron is donated first to the P-cluster and then transferred to the M-center, where substrates are reduced [20].

With an available crystal structure, much attention has been paid to the transfer of electrons to the MoFe protein and unavoidable ATP

hydrolysis. Molecular modeling studies suggest that the 4Fe-4S cluster of the Fe protein docks with the MoFe protein near the P-cluster [21]. This docking arrangement would bring the twofold symmetry axis of the Fe protein in line with the pseudo-twofold $\alpha\beta$ interface of the MoFe protein. Results of mutagenesis [22] and cross-linking [23] studies are consistent with this model. Furthermore, residues in the docking region are linked to the P-cluster ligands via short alpha helices [20]. During docking and hydrolysis, structural rearrangements could occur via these helices which could change the overall geometry and redox behavior of the P-cluster to facilitate electron transfer. Structural rearrangements such as this could initiate or be facilitated by the hydrolysis of MgATP on the Fe protein.

Nitrogenase is known to reduce several substrates other than nitrogen, such as azide, acetylene and methylisocyanide (for a more complete list, see ref [24]). In fact, the common method for measuring nitrogenase activity in the laboratory is to measure the rate of acetylene reduced to ethylene. Although there is compelling evidence that the M-center is the enzyme active site, the exact mechanism by which any substrates bind is still unknown. Electronic calculations by Dance [25] and Deng and Hoffman [26] indicated that dinitrogen might bind to the surface of the M-center, but that structural rearrangements would be necessary.

In a comprehensive series of papers, Thorneley and Lowe [27]

presented a kinetic model of nitrogenase activity (Figure 3). This model illustrates the eight different reduction states of the MoFe protein (denoted as E_0-E_7). To move from one 'E_n' state to the next, a rate limiting Fe and MoFe protein association/dissociation with ATP hydrolysis occurs [28]. An interesting aspect of this scheme is that dinitrogen does not bind until the E_3 state, yet hydrogen is evolved as soon as E_2. Also, ammonia is released two electron transfer cycles before returning to the resting state. This implies that ATP hydrolysis may not be connected directly to N_2 reduction.
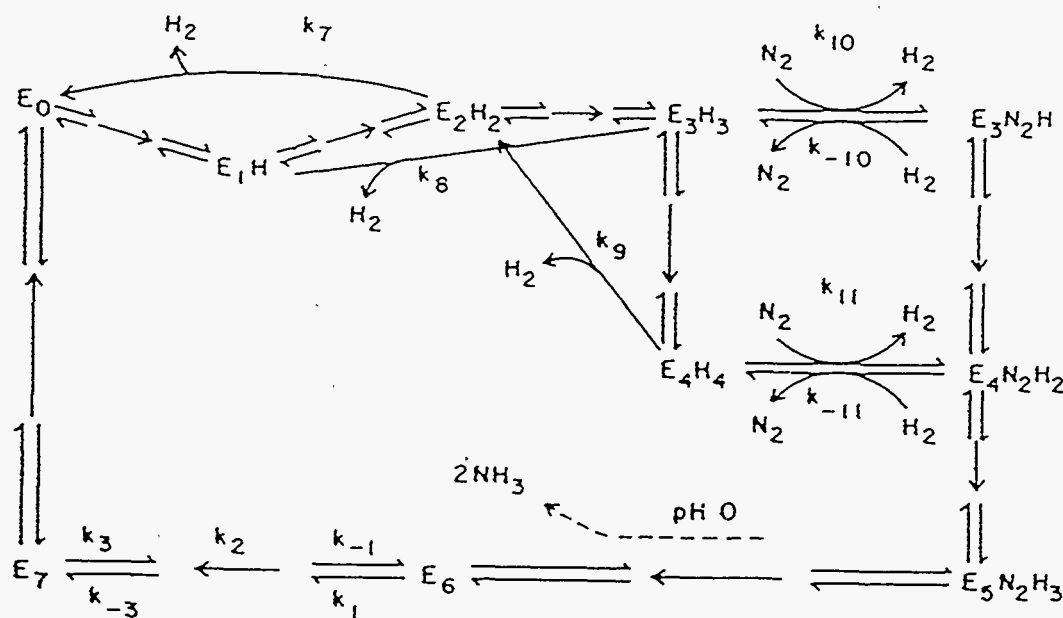
Figure 3: MoFe protein Kinetic scheme proposed by Thorneley and Lowe, from ref [27a]. Resting protein is in the E_0 state, and the other E_n states represent further reductions of the MoFe protein.

References

(1) Stryer, L. *Biochemistry,,* W.H. Freeman and Co., New York, 1988; pp 576.

(2) (a) Orme-Johnson, W.H. *Annu. rev. Biophys. Biophys. Chem.* **1985,** *14,* 419.

(b) Eady, R.R. *Adv. Inorg. Chem.* **1991,** *36,* 77.

(3) Eady, R.R.; Lowe, D.J.; Thorneley, R.N.F. *FEBS Lett.* **1978,** *95,* 211.

(4) (a) Hales, B.J.; Case, E.E.; Morningstar, J.E.; Dzeda, M.F.; Mauterer, L.A. *Biochemistry* **1986,** *25,* 7251. (b) Robson, R.L.; Eady, R.R.; Richardson, T.H.; Miller, R.W.; Hawkins, M.; Postgate, J.R. *Nature* **1986,** *322,* 388.

(5) Chisnell, J.R.; Premakumar, R.; Bishop, P.E. *J. Bacteriol.* **1988,** *170,* 27.

(6) Münck, E.; Rhodes, H.; Orme-Johnson, W.H.; Davis, L.C.; Brill, W.J.; Shah, V.K. *Biochim. Biophys. Acta* **1975,** *400,* 32.

(7) Huynh, B.W.; Münck, E.; Orme-Johnson, W.H. *Biochim. Biophys. Acta* **1979,** *527,* 192.

(8) (a) McLean, P.A.; Vasilios, P.; Orme-Johnson, W.H.; Münck, E. *J. Biol. Chem.* **1988,** *262,* 12900.

(9) (a) Cramer, S.P.; Hodgson, K.O.; Gillum, W.O.; Mortenson, L.E. *J. Am. Chem. Soc.* **1978**, *100*, 3398. (b) Cramer, S.P.; Gillum, W.O.; Hodgson, K.O.; Morteson, L.E.; Stiefel, E.I.; Chisnell, J.R.; Brill, W.J.; Shah, V.K. *J. Am. Chem. Soc.* **1978**, *100*, 3814.

(10) Conradson, S.D.; Burgess, B.K.; Newton, W.E.; Mortenson, L.E.; Hodgson, K.O. *J. Am. Chem. Soc.* **1987**, *109*, 7507.

(11) Flank, A.M.; Weininger, M.; Mortenson, L.E.; Cramer, S.P. *J. Am. Chem. Soc.* **1986**, *108*, 1049.

(12) Bolin, J.T.; Ronco, A.E.; Mortenson, L.E.; Morgan, W.V.; Williamson, M.; Xuong, N.-H. in *Nitrogen Fixation: Achievements and Objectives*, Gresshoff, P.M.; Roth, E.L.; Stacey, G.; Newton, W.E. Eds.; Chapman and Hall, New York, 1990; pp. 117.

(13) Georgiadis, M.M.; Komiya, H.; Chakrabarti, P.; Woo, D.; Kornuc, J.J.; Rees, D.C. *Science* **1992**, *257*, 1653.

(14) Kim, J.; Rees, D.C. *Biochemistry* **1994**, *33*, 389.

(15) (a) Kim, J.; Rees, D.C. *Science* **1992**, *257*, 1677. (b) Kim, J.; Rees, D.C. *Nature*

1992, *360*, 553. (c) Chan, M.K.; Rees, D.C. *Science* **1993**, *260*, 792.

(16) Campobasso, N. *Ph.D. Thesis*, Purdue U., 1994.

(17) Burgess, B.K. *Chem. Rev.* **1990**, *90*, 1377.

(18) (a) Scott, D.J.; May, H.D.; Newton, W.E.; Brigle, K.E.; Dean, D.R. *Nature* **1990**, *343*, 188. (b) Scott, D.J.; Dean, D.R.; Newton, W.E. *J. Biol. Chem.* **1992**, *267*, 20002.

(19) (a) Bothe, H.; Neuer, G.; Kalbe, I.; Eisenbrenner, G. *Annu. Proc. Phytochem. Soc. Eur.* **1980**, *18*, 80. (b) Yates, M.G. in *The Biochemistry of Plants - Vol 5*, Mifflin, B. ed.; Academic Press, New York, **1980**; pp 1.

(20) Dean, D.R.; Bolin, J.T.; Zheng, L. *J. Bacteriol.* **1993**, *175*, 6737.

(21) Howard, J.B. in *Molybdenum Enzymes, Cofactors and Model Systems,* Steifel, E.I.; Coucouvanis, D.; Newton, W.E. eds.; ACS Symposium Series 535, 1993; pp 271.

(22) (a) Lowery, R.G.; Chang, C.L.; Davis, L.C.; McKenna, M.-C.; Stephens, P.J.; Ludden, P.W. *Biochemistry* **1989**, *28*, 1206. (b) Kim, C.H.; Zhen, L.; Newton, W.E.; Dean, D.R. in *New Horizons in Nitrogen Fixation*; Palacios, R.; Mora, J.;

Newton, W.E. eds.; Kluwer Academic Publishers, Norwell, Massachusetts, 1992; pp 105. (c) Wolle, D.; Kim, C.H.; Dean, D.R.; Howard, J.B. *J. Biol. Chem.* **1992,** *267,* 3667. (d) Seefeldt, L.C. *Prot. Sci.* **1994,** *3,* 2073.

(23) Willing, A; Howard, J.B. *J. Biol. Chem.* **1990,** *265,* 6596.

(24) Lowe, D.J.; Thorneley, R.N.F. in *Metalloproteins, Part I: Metal Proteins with Redox Roles,* Harrison, P.M. ed.; Verlag Chemie, Florida, 1985; pp 207.

(25) Dance, I.G. *Aust. J. Chem.* **1994,** *47,* 979.

(26) Deng, H.; Hoffman, R. *Agnew. Chem. Int. Ed. Engl.* **1993,** *32,* 1062.

(27) (a) Lowe, D.J.; Thorneley, R.N.F. *Biochem. J.* **1984,** *224,* 877. (b) Thorneley, R.N.F.; Lowe, D.J. *Biochem. J.* **1984,** *224,* 887. (c) Lowe, D.J.; Thorneley, R.N.F. *Biochem. J.* **1984,** *224,* 895. (d) Thorneley, R.N.F.; Lowe, D.J. *Biochem. J.* **1984,** *224,* 903.

(28) Thorneley, R.N.F.; Lowe, D.J. *Biochem. J.* **1983,** *215,* 393.

Chapter IV

Iron EXAFS of *A. vinelandii* Nitrogenase MoFe and VFe Proteins

Evidence for Long Fe-S and Fe-Fe interactions[1]

ABSTRACT

The structure of the iron sites of nitrogenase in dithionite-reduced and thionine-oxidized forms of the MoFe and VFe proteins has been investigated using Fe K-edge x-ray absorption spectroscopy. For the dithionite-reduced *A. vinelandii* Mo-Fe protein, the dominant EXAFS Fourier transform peaks are assigned to Fe-S and Fe-Fe interactions at 2.32 and 2.64 Å, as expected for Fe-S clusters. An additional Fe-Mo component at 2.73 Å is required to completely fit the EXAFS in the 1-3 Å region. In the 3-5 Å region, a 3.8 Å Fe-Fe component is identified, with an amplitude corresponding to almost 1 long Fe-Fe interaction, averaged over all the iron in the sample. Features that can

---

be explained as Fe-S and Fe-Fe interactions at 4.3 and 4.7 Å are also observed. A similar pattern of Fe interactions is observed for the reduced *A. vinelandii* V-Fe protein, except that the short Fe-Mo interaction is no longer required. In both Mo-Fe and V-Fe proteins, the first coordination sphere Fe-S distances contract slightly upon thionine oxidation. The long range Fe-S and Fe-Fe interactions are very close (within 0.1 Å) to corresponding distances in Fe_6S_6 prismane clusters. If the amplitudes are adjusted by assuming that only 14 of 30 nitrogenase irons participate in the M center, then they are consistent with recently proposed crystallographic models. String-bag models and fused-cubanes are also compatible with the EXAFS. The strength of the long distance components tends to rule against singly-bridged cubane models, or models with very low symmetry.

Introduction

Biological reduction of dinitrogen to ammonia is catalyzed by the enzyme system nitrogenase, in parallel with hydrogen evolution and ATP hydrolysis [1]:

$$N_2 + 8H^+ + 8e^- + nMgATP \ -> \ 2NH_3 + H_2 + nMgADP + nP_i$$
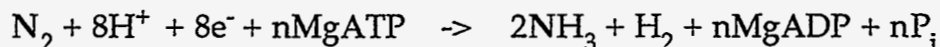
The nitrogenase system contains two proteins, a large (>200,000 dalton) protein referred to as component 1 or dinitrogenase or Mo-Fe protein [2], and a smaller ~55,000 dalton protein known as component 2, dinitrogenase reductase, or simply the Fe protein. The component 1 protein from *Azotobacter vinelandii* (Av1) contains 30 Fe atoms and 2 Mo atoms per $\alpha_2\beta_2$ dimer [1]. Eight metal ions are grouped in an extractable iron-molybdenum cofactor or `FeMo-co', also called the `M-center' [3], which is thought to contain the active site, and for which elemental analysis indicates an Fe:Mo:S ratio of ~7:1:(9±1) [4]. The alternate component 1 from *Azotobacter vinelandii* (Av1') [5,6] possesses a similar cofactor (`FeV-co'), but with vanadium in place of molybdenum. Reported metal analyses find ~23 Fe and 2 V per $\alpha_2\beta_2\gamma_2$ unit [7]. Bishop and coworkers have purified a third type of component 1 [8] from *Azotobacter vinelandii* which lacks Mo and V presumably containing an all iron cofactor. In all of these proteins, the remaining irons that are not part of the FeMo-co are grouped in so-called `P'-clusters, originally thought to be 4Fe-
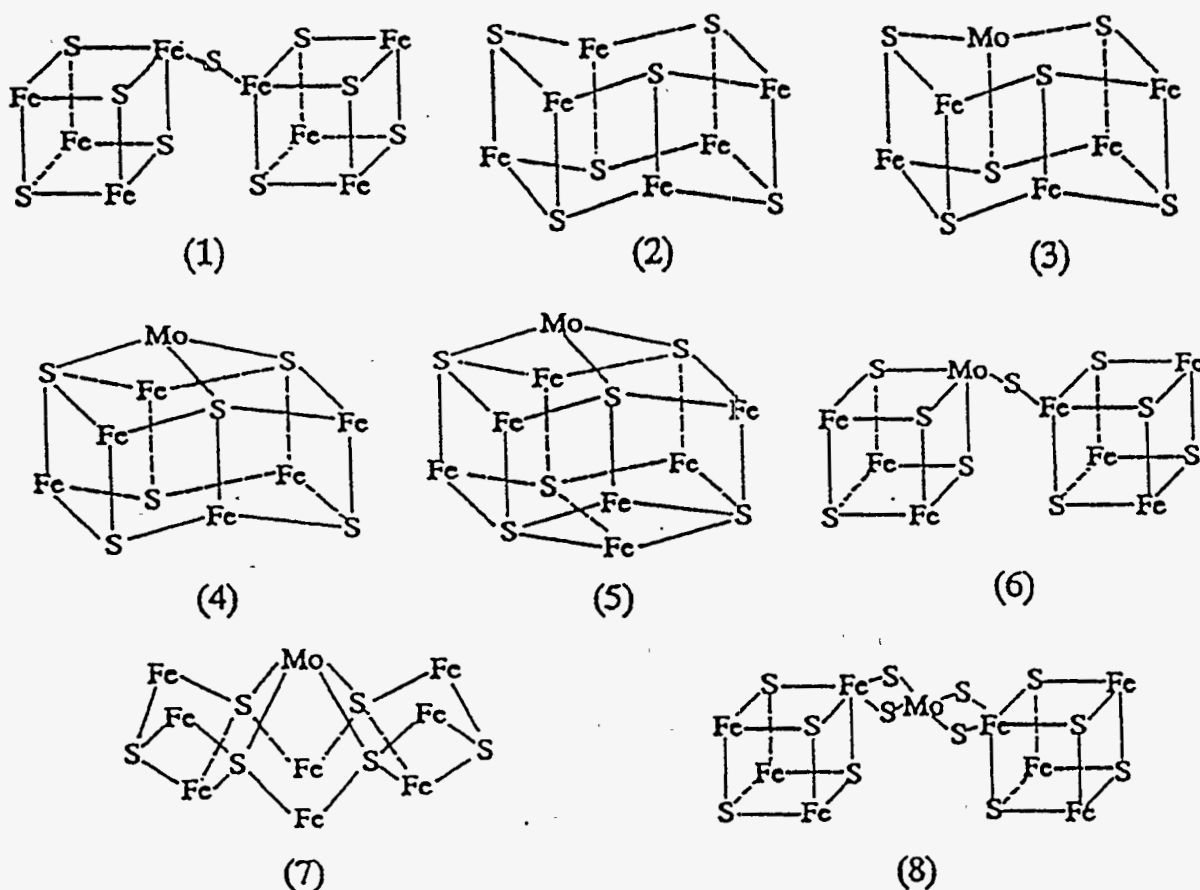
Scheme I: (1) Bridged cubane P-cluster model [21]; (2) normal Fe6S6 prismane [22]; (3) Mo substituted prismane (MoFe5); (4) Mo capped prismane (MoFe6); (5) double capped prismane (MoFe7) [23]; (6) S bridged cubes (MoFe7) [24]; (7) "string bag" model (MoFe8) [25]; (8) Mo bridged cubes (MoFe8) [26].

4S centers. Crystal structures for both the *Clostridium pasteurianum* [9] and *Azotobacter vinelandii* [10] Mo-Fe proteins are progressing rapidly, and structural models for the nitrogenase FeMo-co and P-cluster have been proposed based on 2.7 Å resolution x-ray diffraction data [11].

Many details about the Fe-Mo or Fe-V cofactors in nitrogenase have

already been derived from EXAFS spectroscopy [12]. The Mo EXAFS of both Mo-Fe protein solutions, FeMo-co solutions, and crystals of Mo-Fe protein found average Mo-(O,N), Mo-S and Mo-Fe distances of ~2.1 Å, ~2.4 Å, and 2.7 Å, respectively [13-15]. The V EXAFS of *A. chroococcum* Ac1* [16] and it *A. vinelandii* Av1' [17] proteins shows similar structure, with V-S and V-Fe distances of ~2.3 and 2.75 Å. The Fe EXAFS of isolated FeMo-co [18] and FeV-co [19] reveals not only 2.7 Å Fe-Fe interactions characteristic of Fe-S clusters [20], but 3.7 Å Fe-Fe distances typical of both prismanes and carboxylate-bridged Fe dimers. Over the years, based on these EXAFS results, as well as other spectroscopy and chemical analysis, a wide variety of structures have been proposed (Scheme 1).

The recent x-ray diffraction results from Kim and Rees [10] and Bolin *et al.* [9] have made the models of Scheme 1 obsolete, and the new models for P-clusters and FeMo-co are shown in Scheme 2. Among the surprising features are 1) a number of trigonal, rather than tetrahedral, iron centers, 2) possible bridging by oxygen or nitrogen donors, and 3) the possible presence of a disulfide in the P-cluster. Since exact interatomic distances are not yet available from the crystallography, and since the models are still subject to revision, additional constraints from EXAFS and other methods are still relevant. In this paper, the Fe EXAFS of intact Mo-Fe and V-Fe proteins is reported for the first time. 6 different average Fe-X distances have been observed for the dithionite-reduced state. Furthermore, slight structural

changes are observed in the thionine-oxidized form. Old and new models for
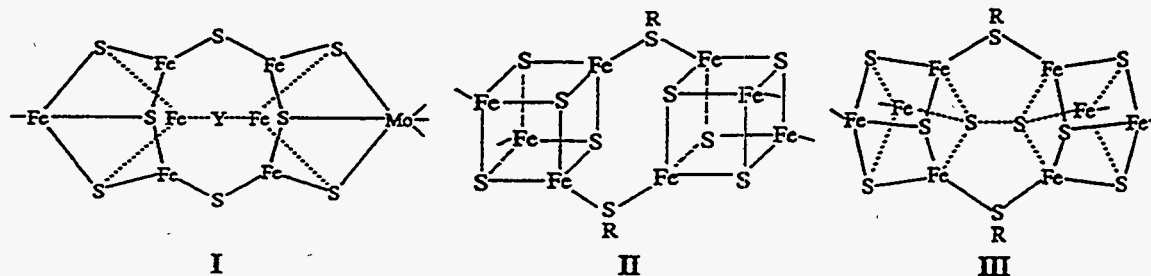
Scheme II: Proposed core structures from crystallography. I and II are the M-center and P-cluster proposed by Kim and Rees [11] while III is the P-cluster proposed by Bolin [27].

the Fe-Mo cofactor structure are discussed.

Experimental

Sample Preparation. The nitrogenase component 1 proteins were extracted from appropriate strains of *A. vinelandii* at LSU by methods previously described [28]. Specific activities were 1800 nmol C_2H_2 reduced min^{-1} (mg of protein^{-1}) protein and 270 nmol C_2H_2 reduced min^{-1}(mg of protein^{-1}) protein for the molybdenum containing (Av1) and vanadium containing proteins (Av1') respectively. For EXAFS measurements, the samples (in 0.025 M Tris-HCl pH 7.4, 0.18 M NaCl, 2 mM $Na_2S_2O_4$) were concentrated to ~200 mg/ml, with 40% glycerol added to prevent ice crystal formation. Thionine oxidized samples were prepared by titration of the protein sample with a 0.22M solution of thionine in 0.025 M Tris-HCl pH 7.4, 0.1 M NaCl until the endpoint, or by brief stirring over a few grains of solid thionine followed by membrane filtration to remove any excess thionine. EPR measurements

confirmed that during these brief exposures to thionine, the M center EPR disappeared and the P-clusters were oxidized to the S=integer state, rather than the S=7/2 state. Specific activities of the prepared oxidized samples were 1800 nmol C_2H_2 reduced min^{-1}(mg of protein^{-1}) and 260 nmol C_2H_2 reduced min^{-1}(mg of protein^{-1}) for Av1 and Av1' respectively. The prismane compounds $(Et_3N)_3(Fe_6S_6Cl_6)CH_3CN$ and $(Et_4N)3[(Fe_6S_6(OC_6H_4\text{-}p\text{ -Me})_6)]$ were synthesized in the Coucouvanis laboratory by methods previously described [22,29], while $Fe_2(O_2CH)_4(BIPhMe)_2$ was provided by Prof. Stephen Lippard of the Massachusetts Institute of Technology [30].

Enzyme EXAFS samples were injected into 2 cm long by 3mm high lucite sample cells with 1 mm pathlength and polypropylene windows. All sample preparation was carried out in a Vacuum Atmospheres glovebox in an Ar atmosphere, with $[O_2] < 1$ ppm. Upon removal from the glovebox, enzyme samples were maintained in liquid nitrogen until data collection. Assays on representative samples found no significant activity loss after 20 hours of beam exposure at 4 K.

Data Collection. The x-ray absorption spectra were recorded at 4-10 K with an Oxford Instruments CF1208 liquid helium flow cryostat using a Si(111) double crystal monochromator at beamline X-19A of the National Synchrotron Light Source. The second crystal was detuned to 50% of maximum intensity to

reduce the transmission of higher order x-rays. The beamline was run unfocussed with slits typically 2x20 mm. Model compounds were run in transmission mode, using finely powdered samples which were diluted with sucrose (1:4 wt:wt). The incidence and transmitted beam intensities were monitored by nitrogen-filled ion chambers.

All protein sample data were measured in fluorescence excitation mode [31]. The fluorescence signal was monitored by a Canberra Industries 13-element Ge solid state array detector [32], with single channel analyzer windows set on the Fe Kα signal. During the measurement, total count rates on each detector were maintained at less than 35 kHz, and an amplifier shaping time of 0.5 μsec was used in most cases. The x-ray absorption spectra were recorded in the form F/I_0 $vs.$ energy. Each scan contains 511 points, spanning about 100 eV below to at least 800 eV above the edge and takes about 40 minutes. The spectra were calibrated by reference to an Fe foil, using the first inflection point as 7111.2 eV.

Long distance interactions are important for cluster characterization, and normally produce very weak modulations of the x-ray absorption. To check the reproducibility of spectral features, each reported spectrum was measured on at least two separate occasions with different samples. The reduced Mo-Fe protein spectrum reported represents the average of 50 scans. 40, 38, and 18 scans were averaged for the oxidized Av1, reduced Av1′, and

oxidized Av1' samples, respectively.

Analysis Procedures. The EXAFS was extracted from the fluorescence excitation (for protein samples) and transmission (for model compounds) spectra by routine methods [33]. An initial E_0 of 7130 eV was used to define the magnitude of the photoelectron wave vector $k = [(8\pi^2 m/h^2)(E-E_0)]^{1/2}$. The EXAFS spectra were Fourier transformed from k-space to R-space, and different regions of the transform were then backtransformed to yield Fourier-filtered spectra. The simulated EXAFS was calculated by using the standard curved-wave functional form for single-scattering EXAFS [34]:

$$\chi(k) = \sum_i \frac{N_i \gamma_i f(k,R_i)}{k R_i^2} e^{-2\sigma_i^2 k^2} \sin[2kR_i + \phi_i(k,R_i)]$$

where $f(k,R_i)$ is the curved-wave backscattering amplitude, $\phi(k,R_i)$ represents the distance-dependent total phase shift, σ_i is the root-mean-square fluctuation in the distance R_i, γ_i is a scaling factor which accounts for the effect of intrinsic processes, and the sum is over all neighbors about the central x-ray absorber [34]. A nonlinear least squares routine was used to minimize the difference between calculated and observed EXAFS.

Phase-corrected Fourier transforms, using the theoretical Fe-Fe phase shift over $k=1-14$ Å^{-1}, were computed for all of the presented radial

distributions. All curve fitting was based on k^3-weighted data over the 3-14Å^{-1} range, and the scale factor γ, was held fixed at 0.9. For Fe-S, Fe-Fe and Fe-O interactions, the threshold energy shifts, ΔE_0, were optimized for the model compounds and held fixed at the same values for the protein fits. For Fe-Mo interaction the ΔE_0 was held fixed at the value obtained from the reduced protein fit.
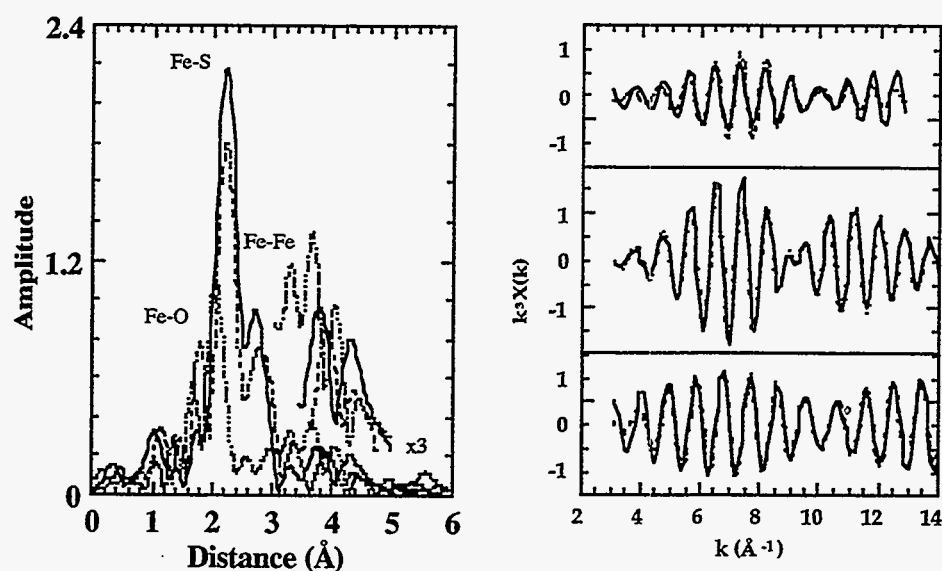
Figure 1: EXAFS Fourier transforms for Fe compounds with long Fe-Fe distances. *(left)* Fourier transform data for [Fe$_6$S$_6$(OC$_6$H$_4$-p-Me)$_6$]$^{3-}$ prismane (dashed), [Fe$_6$S$_6$Cl$_6$]$^{3-}$ prismane (solid), and Fe$_2$(O$_2$CH)$_4$(BIPhMe)$_2$ (dotted). Features beyond 3 Å have been multiplied by 3 in the inset to enhance visibility. *(right)* Filtered data (solid) and fits (dashed) in the 3-5 Å region for [Fe$_6$S$_6$(OC$_6$H$_4$-p-Me)$_6$]$^{3-}$ prismane (top), [Fe$_6$S$_6$Cl$_6$]$^{3-}$ prismane (middle) and Fe$_2$(O$_2$CH)$_4$(BIPhMe)$_2$ (bottom).

Results

Model Compounds. EXAFS analysis of long distance metal-metal interactions may involve complications from multiple scattering and mean

free path effects [35]. To calibrate and check the curve-fitting analysis procedures, we recorded spectra of several iron complexes with long Fe-Fe distances, including two sulfido-bridged Fe_6S_6 prismane clusters and a formate-bridged dinuclear Fe complex, $Fe_2(O_2CH)_4(BIPhMe)_2$ [30]. The Fourier transforms of these data are illustrated in Figure 1. To simulate the EXAFS, the 1-3 and 3-5 Å regions were first separately backtransformed
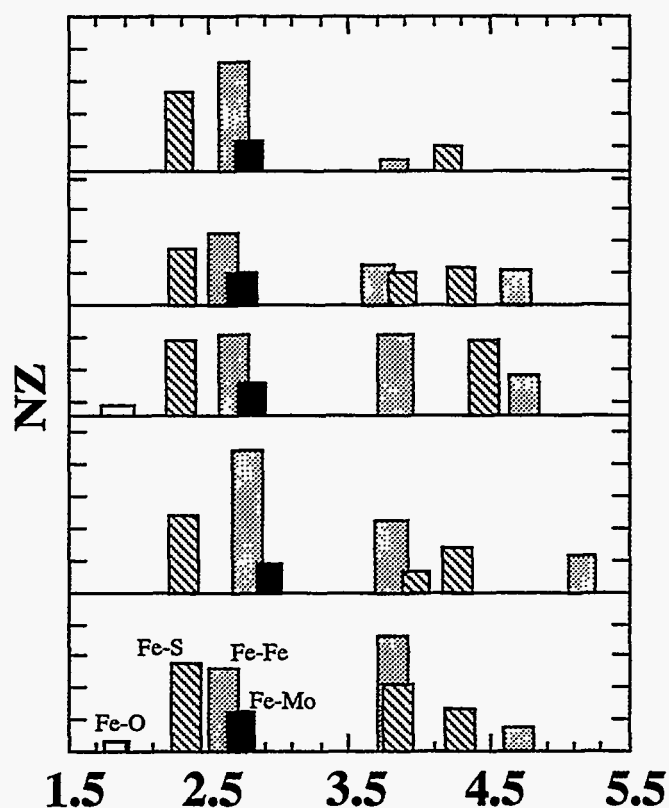
Figure 2: Structure and radial distributions around Fe for different structures. Top to bottom, in order: singly bridged double cube, "string-bag", capped prismane, Kim and Rees model [11], and MoFe protein (EXAFS results). For the ordinate, the number of atoms (N) is multiplied by the atomic number (Z). Hatching patterns for all Fe-X pairs are indicated in the bottom panel.

(Figure 1). Optimization proceeded by starting with fixed coordination numbers, and varying the distances R_i, the threshold energy shift ΔE_0, and

mean square deviations σ^2 for each component. This procedure, totally within the single-scattering formalism, gave distances within 0.02 and 0.06 Å of the crystallographic values for 1-3 and 3-5 Å regions respectively, as shown in Tables 1 and 2.

The high symmetry of the $[Fe_6S_6Cl_6]^{3-}$ prismane complex core (Scheme 1, cluster 2) allows easy observation and interpretation of EXAFS interactions out to 4.7 Å. The strongest peak at ~2.3 Å corresponds to overlapping first
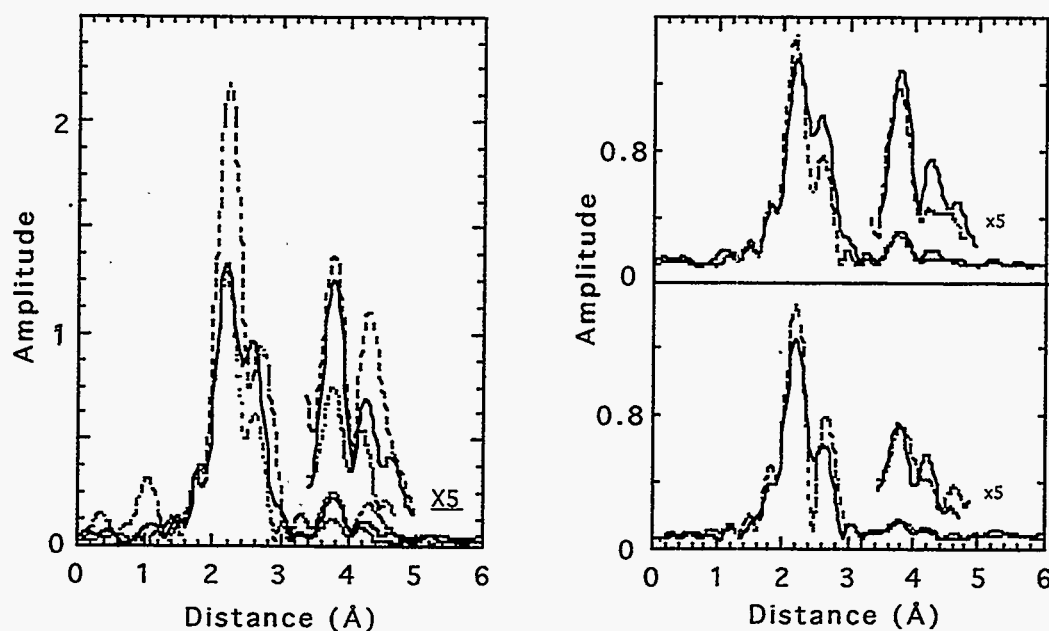
Figure 3: Fe EXAFS Fourier transforms for nitrogenase. *(a, left)* Comparison of Fourier transforms for $[Fe_6S_6Cl_6]^{3-}$ prismane (dashed), reduced Av1 protein (solid), and reduced Av1' (dotted). *(b, right)* (top) reduced (solid) vs. oxidized (dashed) Av1; (bottom) reduced (solid) vs. oxidized (dashed) Av1'. Features beyond 3Å have been multiplied by 5 in the insets to enhance visibility.

shell Fe-S and Fe-Cl interactions. The Fe-Cl component at 2.22 Å adds constructively to the 2.28 Å Fe-S component. By reference to the radial

distribution function in Figure 2, the peaks at 2.76 and 3.8 Å can be assigned

respectively to a pair of short di-μ-sulfido bridged iron-iron interactions and

to three long Fe-Fe interactions with single sulfur bridges. A shoulder at 4.7

Å, although totally nonconvincing in magnitude, can be adequately
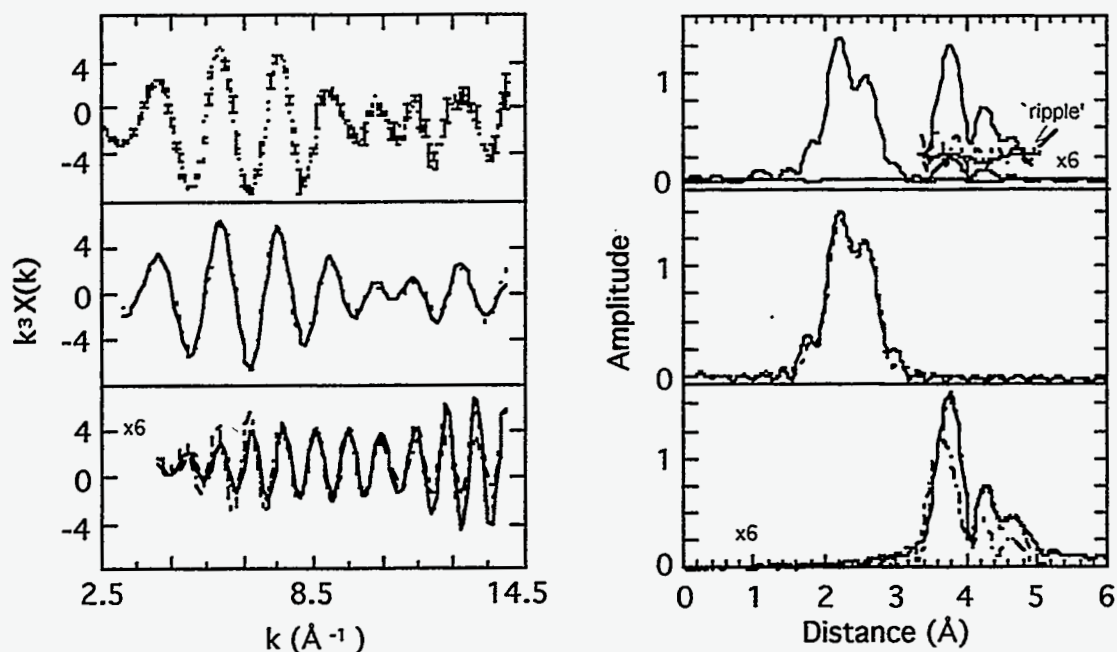
Figure 4: Fourier transform filtering of nitrogenase Fe EXAFS. *(a, left)* (top) Raw data and error bars; (middle) filtered data (solid) and fit (dashed) for the 1-3 Å region. (b, right) Fe-Fe phase corrected Fourier transforms for the data sets shown in a. (top) Reduced MoFe protein vs. estimated noise level and Fourier transform ripple. Features in the 3-5 Å region have been multiplied by 6 in the inset. (middle) Data (solid) vs. best fit (dashed) with and without (dotted) the ~4 Å Fe-X component.

simulated as a single cross-prismane Fe-Fe interaction. The peak at 4.4 Å

arises from three cross-cluster Fe-S interactions.

The Fourier transform for the $[(Fe_6S_6(OC_6H_4\text{-}p\text{-}Me)_6)]^{3-}$ prismane

requires additional interpretation, because of the phenolate ligand

contribution to the EXAFS. In the first coordination sphere region, replacement of chlorine by oxygen results in a smaller 2.3 Å peak and a new feature at ~1.9 Å, the Fe-O component. The average Fe-O-C bond angle is 133°, and the direct Fe-C distance is 2.95 Å. This component may interfere with the 2.8 Å Fe-Fe component. Multiple scattering along the Fe-O-C path may contribute to the transform peak at ~3.3 Å, which is merely a sidelobe artifact in the $[Fe_6S_6Cl_6]^{3-}$ data. The next shells of carbons occur at 3.5 and 4.2 Å, and these direct interactions along with multiple scattering paths, presumably interfere with the longer distance Fe-Fe and Fe-S components at 3.9 and 4.4 Å. Thanks to these interferences, the discrepancies between the crystallographic and EXAFS results are consistently larger for this compound.

Interference between Fe outer shell light atoms and long Fe-Fe components is even more pronounced in the $Fe_2(O_2CH)_4(BIPhMe)_2]$ spectrum. The crystallographic Fe-Fe distance is 3.57 Å, between the first shell of imidazole carbons at 3.13 Å, and the second C,O shell at an average distance of 3.70 Å [30]. The Fe-O-Fe angle is 113°, which is small enough that multiple scattering should not be significant. Still, the Fe-Fe distance obtained by curve-fitting is 3.52 Å; the discrepancy of 0.05 Å is one of the largest errors observed for such metal-metal distance estimation. Bearing in mind the dangers of fitting long Fe-Fe interactions in the presence of other outer shell components, we now present and interpret the nitrogenase Fe EXAFS data.

Nitrogenase and Model Comparisons. The Fe EXAFS Fourier transforms for resting Av1 and Av1' are compared with the $[Fe_6S_6Cl_6]^{3-}$ prismane model in Figure 3a, while transforms for the oxidized *vs.* reduced protein samples are compared in Figure 3b. The features for distances less than 3 Å are much stronger than the longer distance interactions. Since some of the transform peaks might be affected by the statistics of the EXAFS experiment, the noise level was assessed by finding the root-mean-square deviation between 3 EXAFS data sets (Figure 4a). The deviations from the mean for these 3 independent data sets were Fourier transformed separately, and the average magnitude of this 'error transform' is compared with the final data transform in Figure 4b. The transform trancation ripple level was assessed by Fourier filtering and backtransforming the 1-3 Å features, then retransforming the data from 0 to 6 Å. Although the long distance features are small, they are still above the noise and Fourier transform ripple level (Figure 4b).

To reduce the number of adjustable parameters, and to allow the long distance interactions to be modelled with sufficient sensitivity, the region between 3 and 5 Å was backtransformed separately from the 1-3 Å data. The raw and filtered data from this process, are compared with simulations in Figure 4.

Resting (Dithionite-Reduced) Mo-Fe Protein (1-3 Å Region). The two distinct transform peaks in the 1-3 Å region are modelled as Fe-S and Fe-Fe

interactions at ~2.32 and ~2.64 Å respectively. If σ^2 for Fe-S and Fe-Fe are fixed

at values found in the prismane model, then coordination numbers of 2.3

and 1.9 are found for these components. However, a better fit can be gained

by fixing these coordination numbers at 3.5 and 2 while optimizing σ^2 (Table
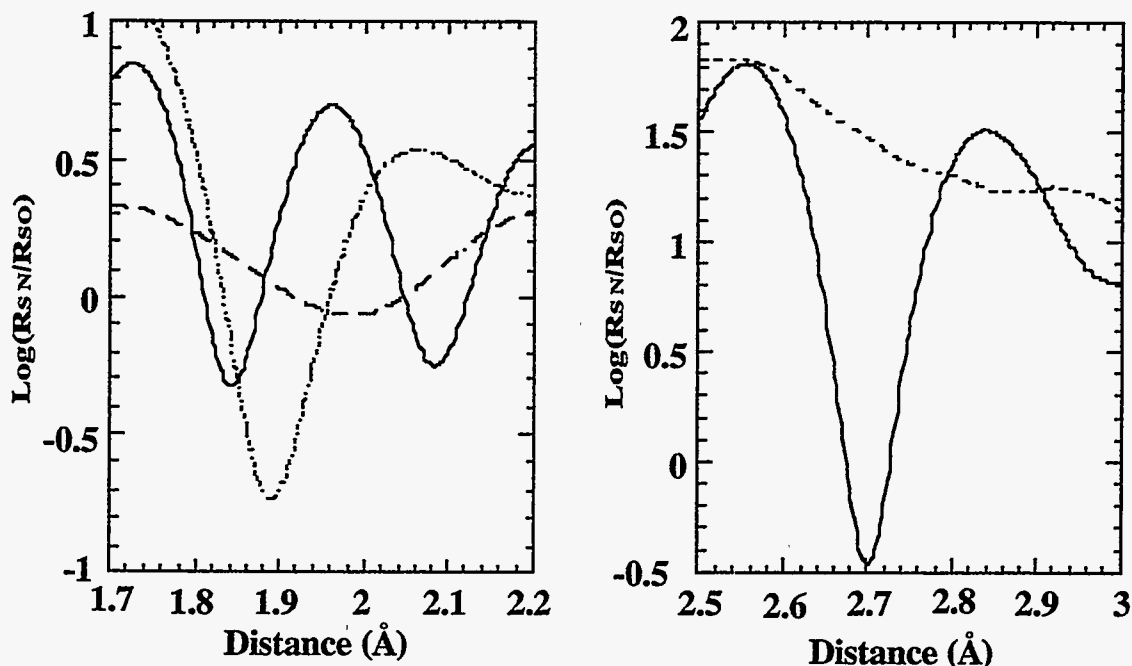
Figure 5: EXAFS search profiles. *(a, left)* Search for Fe-O interaction in $[(Fe_6S_6(OC_6H_4\text{-}p\text{-}Me)_6)]^{3-}$ prismane (dotted), $[Fe_6S_6Cl_6]^{3-}$ prismane (dashed), and the reduced Av1 protein (solid). *(b, right)* Search for Fe-Mo interaction in $[(Fe_6S_6(OC_6H_4\text{-}p\text{-}Me)_6)]^{3-}$ prismane (dashed) and the reduced Av1 protein (solid). Note that the zero level corresponds to no improvement in the quality of fit. The search profiles were drawn for adding 1 Fe-O (left) or 0.3 Fe-Mo (right) interactions.

1). The correlation between N and σ^2 is well known in EXAFS and limits the

precision with which these numbers can be defined [33].

Two other components can be added to further improve the

simulation quality, as illustrated by `search profiles' [36] for Fe-O and Fe-Mo

interactions (Figure 5b). After Fe-S and Fe-Fe components have been included, addition of Fe-Mo at 2.73 Å reduces the fit residual σ^2 by 32%. There is a sharp minimum in this search profile, which is absent for the model
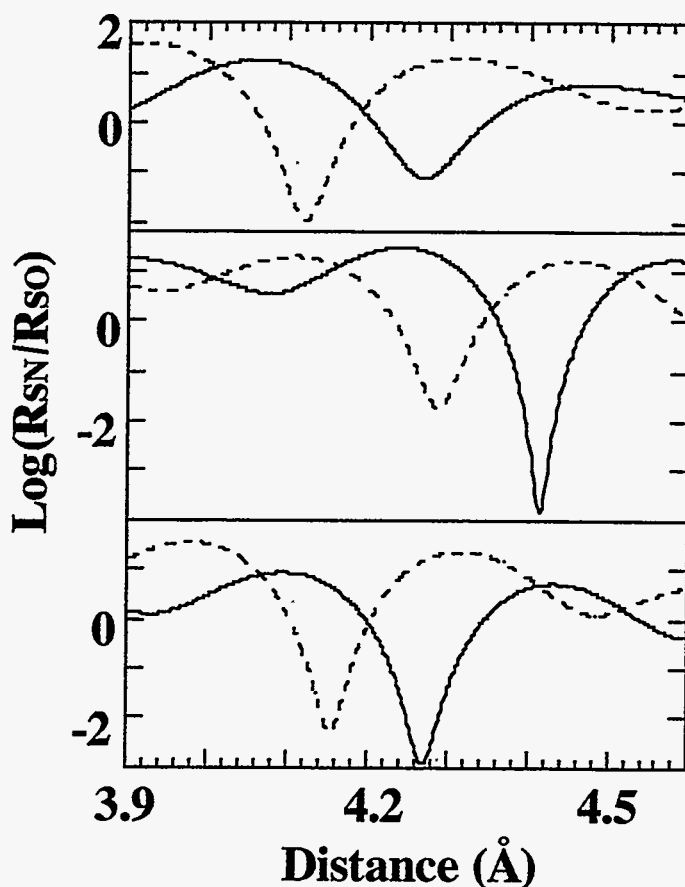
Figure 6: EXAFS search profiles. Search for Fe-C and Fe-S interactions in (top) Fe2[(O2CH)4(BIPhMe)2], (middle) [Fe6S6Cl6]3- prismane, and (bottom) the reduced Av1 protein. The solid curve corresponds to adding 3 Fe-S interactions at the given distance; the dashed curve is for the addition of 4.5 Fe-C interactions.

without Fe-Mo interactions. The 2.73 Å distance is close to previously reported 2.68-2.72 Å Mo-Fe distance for the protein and the 2.70 Å Fe-Mo distance found in the isolated cofactor [13,18].

Subsequent inclusion of Fe-O at 1.84 Å produces a further 31% improvement [37]. However, the search profile for this Fe-O component in the Mo-Fe protein data does not yield the same degree of improvement as in the search profile for $[(Fe_6S_6(OC_6H_4\text{-}p\text{ -Me})_6)]^{3-}$. As seen in Figure 5a, almost as good a fit can also be obtained by adding an Fe-O interaction at 2.1 Å. Furthermore, even a structure without oxygen ligands shows a slight
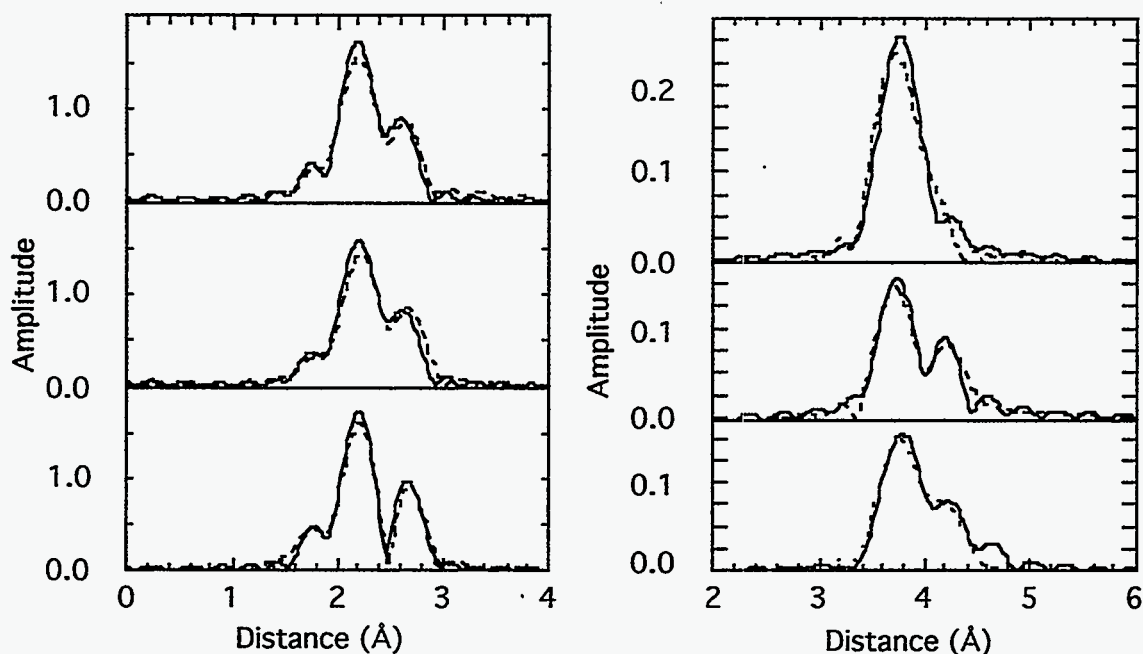
Figure 7: EXAFS data transforms (solid) and fit transforms (dashed) for other nitrogenase forms in the 1-3 Å (a, left) and 3-5 Å (b, right) regions. (top) Oxidized Av1 protein. (middle) Reduced Av1' protein. (bottom) Oxidized Av1' protein.

improvement in fit when a small oxygen component is added, perhaps due to small systematic errors in the theoretical fitting functions. Although some Fe-(O,N) ligands may be distributed among the 15 different irons in the Mo-Fe protein, they cannot be well discerned in the EXAFS.

Resting (Dithionite-Reduced) Mo-Fe Protein (3-5 Å Region). The dominant feature in this region is well-modelled as an Fe-Fe interaction at 3.78 Å. The Fourier transform magnitude is similar to the $[Fe_6S_6Cl_6]^{3-}$ prismane spectrum, as shown in Figure 3. The Fourier transform peak is weaker in the Av1' data. Additional transform features at 4.3 and 4.7 Å are evident, and based on analogy with the prismane radial distribution, they were tentatively identified as Fe-S and Fe-Fe distances, respectively.

In the long distance fits, summarized in Table 2, the σ^2 for Fe-Fe and long Fe-S were fixed at model compound values, and coordination numbers were allowed to vary. To confirm the Fe-S assignment for the 4.3 Å feature, search profiles for Fe-S and Fe-C interactions have been checked for nitrogenase and the previously described model compounds, and the results are plotted in Figure 6. Since Fe-S and Fe-C phase shifts are approximately π out of phase throughout the simulation range, a minimum in the Fe-S search profile will yield a maximum in the Fe-C search. The absolute minima for the model compound search profiles are found with the correct ligand type. The nitrogenase search profile clearly favors a Fe-S assignment for the 4.28 Å feature.

Although not evident as a separate peak in the Fourier transforms, an additional component near 4 Å improves the fit to the data in this region.

After Fe-Fe (3.8 Å), Fe-S (4.3 Å), and Fe-Fe (4.7 Å) features have been included, the fit residual σ^2 is reduced from 7 to 0.3 by adding an Fe-Fe component at 4.0 Å. An almost equally good fit can also be achieved by adding an Fe-S component at 3.9 Å, if we allow ΔE_0 and σ^2 to float. Although it is not clear that wether this feature is due to Fe-Fe, Fe-S, or mix of them, both these interactions are chemically expected. In fact, cross-cube Fe-S distances in the range of 3.849-3.912 Å were reported for synthetic Fe-S cubanes [38], and an average 3.9 Å Fe-S distance was found in a 4Fe-4S protein [39].
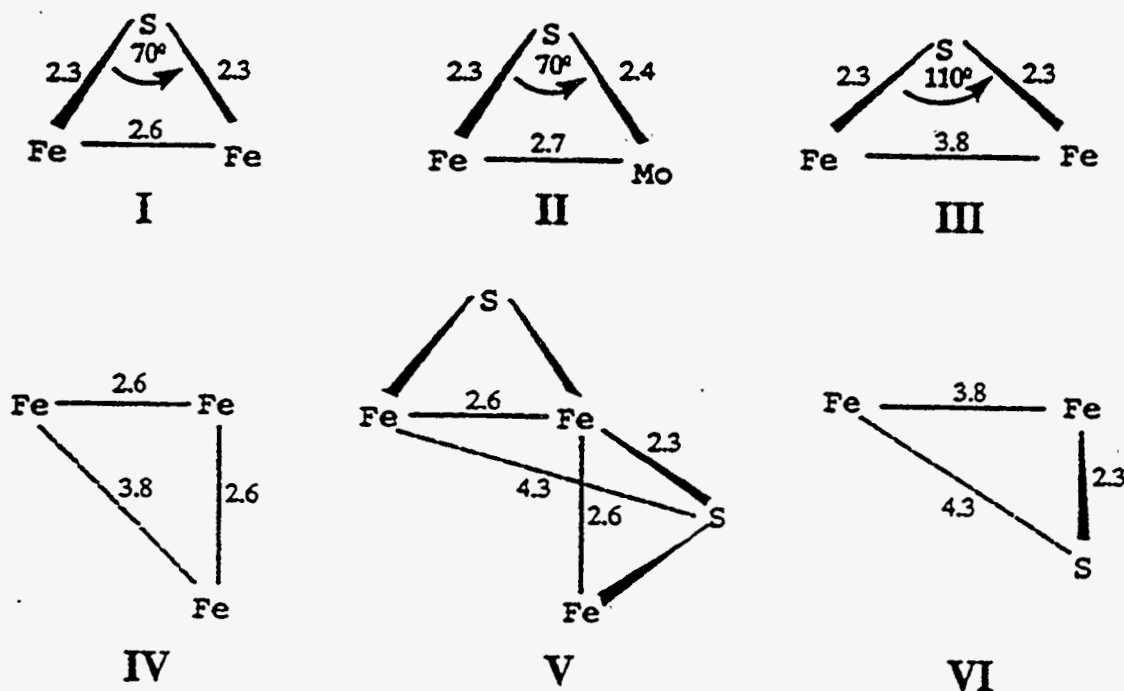
Scheme III: Structural fragments inferred from EXAFS distances (fragments IV and V are insights from the diffraction models.

Thionine-Oxidized Mo-Fe Protein. Although all the features present in the 1-

3 Å region of the reduced Av1 Fe EXAFS are also observed in the oxidized spectrum, thionine oxidation of Mo-Fe or V-Fe proteins produces reproducible changes in intensities of Fourier transform features. The observed Fe-S and Fe-Mo distances derived from curve fitting contract from 2.32 and 2.73 Å to 2.29 and 2.70 Å respectively, while the observed Fe-Fe distance expands slightly, from 2.64 Å to 2.66 Å in the oxidized sample. Although the appearance of the Fourier transform changes, this may be due to a change in interference between overlapping components. If the coordination numbers are held fixed, the optimized values for the mean square deviation of R (σ^2) are very similar for both oxidized and reduced samples. Conversely, if σ^2 values are fixed, the optimized numbers of Fe-S and Fe-Fe interactions change from 3.5 and 2.0 in reduced sample to 3.7 and 1.7 in the oxidized sample. For the 1-3 Å region, the changes in the appearance of the EXAFS Fourier transform are therefore ascribed to slightly different interferences between overlapping shells, rather than dramatic changes in coordination number.

Similar to the reduced sample data, the oxidized spectrum in the 3-5 Å region is dominated by a long Fe-Fe component, now at 3.74 Å, slightly shorter than the 3.78 Å reduced protein value. However, the distances depend on strength of tentative Fe-S component, and the change is within our estimated error of 0.06 Å for these long interactions. The amplitude of this feature is almost unchanged. A ~3.85 Å Fe-S interaction is still required

to fit the region, and the amplitude of this feature is only slightly smaller than the reduced sample (Table 2). The longer Fe-S and Fe-Fe features at 4.3 and 4.7 Å are much less pronounced, and the simulations do not adequately model this region. In Figure 7b, we only show the data and the fit for the 3-4 Å region. Fewer oxidized spectra were recorded, and although we cannot exclude some changes in the longer range structure, we defer further speculation until better data can be obtained.

V-Fe Protein. Most of the features observed in the Mo-Fe protein Fe EXAFS are also observed in the spectra of the V-Fe protein. The first Fe-S and the second Fe-Fe distances both agree within 0.01 Å. Although a Fe-Mo near 2.7 Å is no longer needed, a distinct Fe-V interaction cannot be identified. Since the electron back-scattering phase shifts and amplitudes for vanadium and iron are quite similar, discrimination between Fe-V and Fe-Fe interactions is not expected. Presumably, the Fe-V distances at ~2.7 Å are included in the
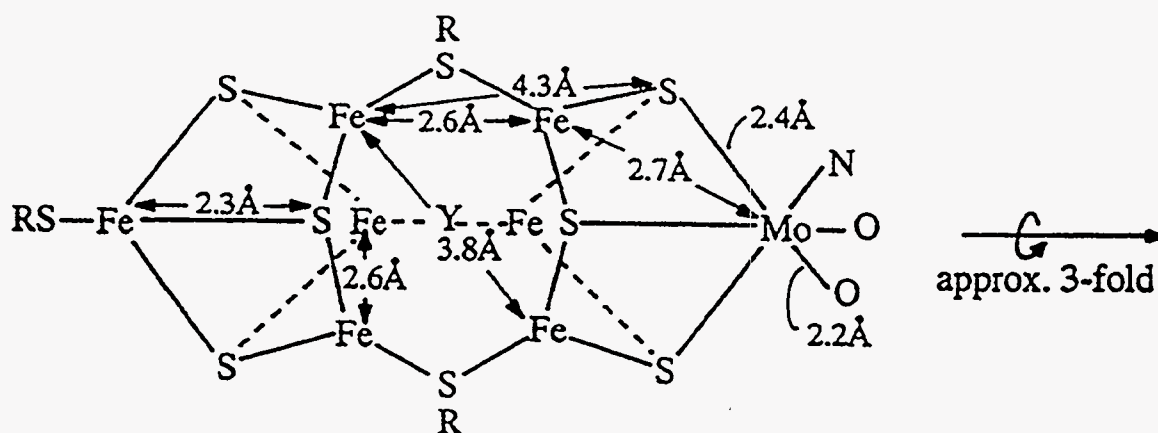
Scheme IV: A plausible assignment of the Fe-X distances observed by EXAFS to the crystallographic model for the M-center. Previous Mo-X distances are also included.

weighted average of Fe-Fe distances. In fact, the calculated first Fe-Fe distances in both oxidized and reduced forms increase from 2.66 and 2.64 Å in the Mo-Fe protein to 2.69 and 2.67 Å in the V-Fe protein.

In the 3-5 Å range, the major component is a 3.74 Å Fe-Fe interaction. The amplitude of this feature is almost unchanged from the reduced Mo-Fe protein. There is also a clear Fe-S component at 4.35 Å. Again, a 3.85 Å Fe-S interaction is needed to complete the fit; the amplitude of this Fe-S interaction is slightly smaller than that in the Mo-Fe sample.

Upon oxidation of the V-Fe protein, there are small changes in both Fe-S and Fe-Fe distances. Just as with the Mo-Fe protein, the average Fe-S distance contracts from 2.32 Å in the reduced sample to 2.29 Å in the oxidized case. The average short Fe-Fe distance expands from 2.67 Å in the reduced protein to 2.69 Å in the oxidized protein. The long Fe-Fe interaction changes from 3.78 Å in the reduced form to 3.74 Å in the oxidized sample. Features consistent with longer Fe-S interaction near 4.4 Å are evident in the transforms, but further analysis awaits higher quality data. The fits and transforms are summarized in Figure 7.

Discussion

Given the presence of 30 Fe per $\alpha_2\beta_2$ protein molecule [1] there are, in

principal, 15 distinct types of iron in the Mo-Fe protein αβ half-molecule. Since solution EXAFS only provides distances and approximate coordination numbers, other data and considerable inference are required to draw structural conclusions from the current results. Some of the assumptions we have made are 1) the P-clusters consist of 2 merged Fe_4S_4 clusters that primarily contribute short Fe-S and Fe-Fe interactions to the EXAFS, 2) the M center contains 7 Fe, bridged by sulfides and/or thiolates, and a single Mo or V atom, 3) multiple scattering effects are not significant, and 4) contributions from ligand outer shell C,N,O atoms (for example, in homocitrate, cysteine, histidine ligands) are small compared to intra-cluster Fe-Fe, Fe-Mo, and Fe-S EXAFS. Although these assumptions were made before publication of recent x-ray diffraction results [11], they are consistent with the Kim and Rees models. With these assumptions, and independent of the crystallography, the interatomic distances observed in the EXAFS can be used to infer the
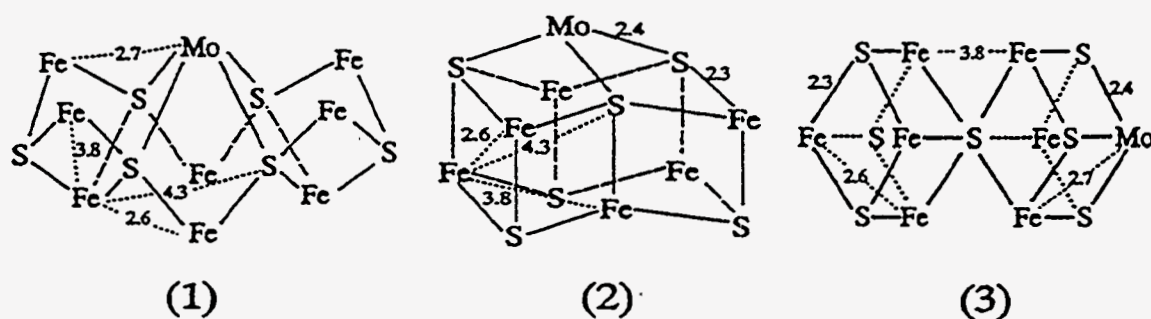
Scheme V: Other hypothetical Fe-Mo-S clusters that were consistent with the EXAFS analysis.

presence of numerous structural fragments, as illustrated in Scheme III.

The Fe-S-Fe and Fe-S-Mo angles in fragments I through III are deduced assuming all Fe-S distances are the same (2.3 Å), using the 2.4 Å Mo-S distance observed in the Mo EXAFS [15], and using a 2.7 Å Fe-Mo distance. This is the first time distances from the iron point of view have been reported for the intact protein, but similar distances have been reported for the isolated Fe-Mo or Fe-V cofactors [18,19]. Note that a 3.8 Å Fe-Fe distance could be sulfur-bridged as in III, or simply the result of arranging 2 perpendicular 2.64 Å Fe-Fe interactions as in IV. Adding sulfurs to IV leads to fragment V, which after duplication and merging leads to core of the Kim and Rees model.

The Fe-S distance at ~4.3 Å is a new interaction, which has not been previously observed in nitrogenase or FeMo-co EXAFS. In the Fe_6S_6 prismane models [22], Fe-S shells occur at ~4.4 Å, and these distances are accurately derived from the EXAFS. In the M center, the Fe and its distant sulfur neighbor could be held together by either two acute Fe-S-Fe angles, in Fe-S-Fe-S chains that occur as in Scheme 3-V, or between one Fe and the sulfur on another Fe that is bridged as in Scheme 3-VI. Since EXAFS is extremely sensitive to variation in absorber-scatterer distances, either through thermal motion or static disorder, there must be considerable rigidity and symmetry in nitrogenase for these interactions to be observed.

The fragment distances derived from EXAFS can be combined with the global geometry revealed by crystallography to build a very precise model for the M center (Scheme 4). The Fe-Fe distances in the planes perpendicular to the approximate 3-fold axis are assigned as 2.64 Å interactions. As seen in the model, another 2.64 Å Fe-Fe can be accomodated parallel to the 3-fold axis. This pair of constraints generates longer 3.8 Å Fe-Fe distances, diagonal to the 3-fold axis. With the Fe framework so defined, the 4.3 Å component can be attributed to interactions between a central iron and two sulfurs near the ends of the structure (Scheme 3- V and Scheme 4). The long 4.7 Å distance can be interpreted as interaction between the iron at the end of the cluster and the far end Fe-plane. These assignments are illustrated in Scheme 4. Distances from previous Mo EXAFS analyses are included for completeness.

In prismane complexes, very long (4.7 Å) Fe-Fe interactions occur between irons on opposite sides of the cluster. On the range of $k=1\text{-}14 \text{ Å}^{-1}$, the long Fe-Fe is not resolved in the model transforms, although it can be separated using a wider range of data. A weak feature in this range is consistently seen in the reduced Av1 data, but it is very close to the noise and truncation ripple level. Attempts to enhance this feature using single crystal EXAFS are in progress.

The strengths and limitations of the EXAFS technique can be appreciated by noting some of the other models consistent with the reported

distances and amplitudes. For example, although synthetic models for the 'string-bag' proposal (Scheme 1, structure 7) [25] are not available, a candidate 'modified string-bag' structure can be generated by using the current set of distances (Scheme 5). We find this model not only has common Fe-S, Fe-Fe and Fe-Mo distances at 2.3, 2.6, and 2.7 Å, but also has longer Fe-Fe, Fe-S and Fe-Fe interactions at 3.8, 4.3 and 4.7 Å. As seen in the radial distribution plot (Figure 2), the radial distribution pattern for this model is very similar to that of Mo-Fe protein.

The prismane class of models, first proposed by analogy with the pendlandite structure by Christou *et al.* [41], and developed synthetically as Mo-capped Fe-S prismanes by Coucouvanis and coworkers [42], was also consistent with the current data. Although the shortest Fe-Mo distances in the low valent synthetic models are in the range of 2.9-3.0 Å [42], much longer than the observed 2.7 Å Fe-Mo interaction, a cluster with a higher oxidation state Mo would presumably have shorter Mo-S and Mo-Fe distances, and would be consistent with all of the current EXAFS data, as illustrated in Scheme V. Finally, a third model displayed in Scheme V, which has not been proposed or synthesized before, consists of one Mo atom and seven Fe atoms, arranged to form two fused cubes with a common central S atom. This structure, a 'fused-cubane', would also satisfy all the restrictions from the current EXAFS analysis.

The EXAFS data on the oxidized Mo-Fe protein, as well as the reduced and oxidized V-Fe protein, show that the core of the M center is nearly unchanged upon oxidation, or even after replacing Mo with V. In both Mo-Fe and V-Fe proteins, there is a slight contraction in Fe-S distances (averaged with P-cluster changes). However, there is no dramatic change in Fe-Fe distances that might indicate a major cluster reorganization. The features that changed the most were the long Fe-S components at ~4.3 Å. If the oxidized M centers are slightly less symmetric, this could explain the weakening of the very long Fe-S component.

Summary

The Fe K-edge EXAFS has been investigated for reduced and oxidized Mo-Fe and V-Fe protein samples. The results demonstrate the unique ability to determine the local distances of metal centers in biological systems, as well as the limitations for inferring longerrange geometry. EXAFS has truly atomic resolution (0.15 Å) and gives very accurate distances (~1% out to 4 Å). It thus provides an important check on x-ray crystal structures, and the EXAFS spectra of *A. vinelandii* nitrogenase has helped define the better structure of the Fe-Mo cluster. For the dithionite-reduced Mo-Fe protein the EXAFS is dominated by Fe-S and Fe-Fe interactions at 2.32 and 2.64 Å. A Fe-Mo interaction is apparent at 2.71 Å. Longer Fe-Fe interactions at 3.8 Å and 4.7 Å as well as a Fe-S distance at 4.3Å are also observed. A similar pattern of

interactions is observed for the reduced V-Fe protein. Thionine oxidation causes a small contraction in Fe-S and possible Fe-Mo distances. The longer distance (3.8 Å Fe-Fe and 4.3 Å Fe-S) interactions are still evident, indicating that much of the basic geometry is unchanged. The distances are consistent with models modified from that recently derived using X-ray crystallography. Additional studies to search for structural changes after reduction or inhibition are in progess.

Table I: Nitrogenase and Model Compound 1-3 Å Curve Fitting.

Sample	Fe-S(Cl) ΔE_0=-3 eV N^a	R^b, Å	$10^5\sigma^2$, Å^{2e}	Fe-Fe ΔE_0=-8 eV N^a	R^b, Å	$10^5\sigma^2$, Å^{2e}	Fe-Mo ΔE_0=-3 eV N^a, N'^d	R^b, Å	$10^5\sigma^2$, Å^{2e}	Fe-O(N,C) ΔE_0=-3 eV N^a	R^b, Å	$10^5\sigma^2$, Å^{2e}	$R_s{}^e$
$(Fe_6S_6Cl_6)^{3-}$	4.0	2.277	304	2.0	2.757	355							30
$(Fe_6S_6Cl_6)^{3-f}$	4.0	2.276		2.0	2.765								
$(Fe_6S_6Cl_6)^{2-f}$	4.0	2.259		2.0	2.757								
$(Fe_6S_6(OC_6H_4\text{-}p\text{-}Me)_6)^{3-}$	3.0	2.298	568	2.0	2.798	568				1.0	1.890	303	54
$(Fe_6S_6(OC_6H_4\text{-}p\text{-}Me)_6)^{3-g}$	3.0	2.295		2.0	2.781					1.0	1.870		
$Fe_2[(O_2CH)_4(BIPhMe)_2]$										5.5	2.136	609	19
$Fe_2[(O_2CH)_4(BIPhMe)_2]^h$										5.5	2.120		
dithionite reduced Av1	3.5	2.317	576	2.0	2.641	535	0.3 (0.6)	2.732	179	0.5	1.842	7797	22
FeMo-co^i	3.0	2.20		2.2	2.64		0.8	2.70					
thionine oxidized Av1	3.5	2.291	513	2.0	2.657	465	0.3 (0.6)	2.696	34	0.5	1.833	7797	20
dithionite reduced Av1'	3.5	2.322	608	2.3	2.674	773				0.5	1.864	7041	42
FeV-co^i	3.0	2.24		2.0	2.65								
thionine oxidized Av1'	3.5	2.289	542	2.3	2.690	688				0.5	1.869	7041	20

[a] Coordination number; held fixed during refinement. [b] Interatomic distance; systematic errors were ca. 0.02Å for the 1-3 Å region and ca. 0.06 Å for the 3-5 Å region. [c] Mean square deviation of R; negative values arise if the postulated N is low or if the amplitude function is inaccurate. [d] Multiplied by 15/7 for comparison with cofactor data. [e] Fit residual; defined as $(\Sigma(\chi_{exp}-\chi_{calc})^2 k^6)/N$ [f] Reference [19]; [g] Reference [25]; [h] Reference [26]; [i] Reference [16]; [j] Reference [17]

Table II: Nitrogenase and Model Compound 3-5Å Curve Fitting.

Sample	Fe-Fe' ΔE_0=-10 eV			Fe-X ΔE_0=-10 eV			Fe-S'(C) ΔE_0=-16 eV			Fe-Fe'' ΔE_0=-13 eV			$R_s^{[e]}$
	$N^{[a]},N'^{[d]}$	$R^{[b]}$, Å	$10^5\sigma^2$, Å$^{2[e]}$	$N^{[a]}$	$R^{[b]}$, Å	$10^5\sigma^2$, Å$^{2[e]}$	$N^{[a]}$	$R^{[b]}$, Å	$10^5\sigma^2$, Å$^{2[e]}$	$N^{[a]}$	$R^{[b]}$, Å	$10^5\sigma^2$, Å$^{2[e]}$	
$(Fe_6S_6Cl_6)^{3-}$	2.0	3.82	613				3.0	4.41	386	1.0	4.68	487	0.3
$(Fe_6S_6Cl_6)^{3-[f]}$	2.0	3.790					3.0	4.440		1.0	4.70		
$(Fe_6S_6Cl_6)^{2-[f]}$	2.0	3.791					3.0	4.4		1.0	4.7		
$(Fe_6S_6(OC_6H_4\text{-}p\text{-}Me)_6)^{3-}$	2.0	3.90	1051				3.0	4.42	1756	1.0	4.69	725	2.2
$(Fe_6S_6(OC_6H_4\text{-}p\text{-}Me)_6)^{3-[g]}$	2.0	3.836					3.0	4.455		1.0	4.732		
$Fe_2[(O_2CH)_4(BIPhMe)_2]$	1.0	3.519	428				4.5	4.13$^{[k]}$	339				
$Fe_2[(O_2CH)_4(BIPhMe)_2]^{[h]}$	1.0	3.574					4.5	4.263					
dithionite reduced Av1	*1.4 (3)	3.78	613	*1.6	4.00	487	*2.2	4.28	386	*0.4	4.68	487	0.3
FeMo-co$^{[i]}$	1.3	3.68											
thionine oxidized Av1	*1.4 (3)	3.74	613	*0.7	3.99	487	[l]			[l]			1.2
dithionite reduced Av1'	*1.0(2.1)	3.76	613	*0.8	3.99	487	*0.8	4.30	386	[l]			0.5
FeV-co$^{[i]}$	1.0	3.69											
thionine oxidized Av1'	*0.8(1.7)	3.76	613	*0.5	4.02	487	*0.5	4.38	386	[l]			0.4

[a] Coordination number; held fixed during refinement; Those with * were found by optimization. [b] Interatomic distance; systematic errors were ca. 0.02Å for the 1-3 Å region and ca. 0.06 Å for the 3-5 Å region. [c] Mean square deviation of R; negative values arise if the postulated N is low or if the amplitude function is inaccurate. [d] Multiplied by 15/7 for comparison with cofactor data. [e] Fit residual; defined as $(\Sigma(\chi_{exp}\text{-}\chi_{calc})^2k^6)/N$ [f] Reference [19]; [g] Reference [25]; [h] Reference [26]; [i] Reference [16]; [j] Reference [17] [k] The large error (0.13 Å) for the Fe-C distance is due to the complex structure of the compound; the average 4.26 Å distance is the mean value of nine different O,C,N shells between 4.170 and 4.313. [l] Because of limited statistics, only 3-4.5 Å region was fit.

References

(1) a) Orme-Johnson, W. H. *Ann. Rev. Biophys. Biophys. Chem.* **1985**, *14*, 419-459. b) Eady, R. R. *Adv. Inorg. Chem.* **1991**, *36*, 77-102.

(2) Hageman, R. V.; Burris, R. H. *Proc. Nat. Acad. Sci. USA* **1978**, *75*, 2699-2702. Thorneley and coworkers have objected to this nomenclature, since they consider N_2 reduction a property of the complex between components 1 and 2.

(3) Burgess, B. K. *Chem. Rev.* **1990**, *90*, 1377-1406.

(4) a) McLean, P. A.; Wink, D. A.; Chapman, S. K.; Hickman, A. B.; McKillop, D. M.; Orme-Johnson, W. H.*Biochemistry* **1989**, *28*, 9402-9406. b) Frank, P.; Gheller, S. F.; Newton, W. E.; Hodgson, K. O. *Biochem. Biophys. Res. Comm..* **1989**, *163*, 746-754.

(5) Hales, B. J.; Case, E. E.; Morningstar, J. E.; Dzeda, M. F.; Mauterer, L. A. *Biochemistry*, **1986**,*25*, 7251-7255.

(6) Robson, R. L.; Eady, R. R.; Richardson, T. H.; Miller, R. W.; Hawkins, M.; Postgate, J. R. *Nature*, **1986**, *322*, 388-396.

(7) Eady, R. R.; Robson, R. L.; Richardson, T. H.; Miller, R. W.; Hawkins, M.*Biochem. J.* **1987**,*244*, 197-207.

(8) Chisnell, J. R.; Premakumar, R.; Bishop, P. E. *J. Bact.,* **1988**,*170*, 27-33.

(9) a) Bolin, J. T.; Ronco, A. E.; Mortenson, L. E.; Morgan, T. V.; Williamson, M.; Xuong, N.-H. in ``Nitrogen Fixation: Achievements and Objectives" Gresshoff, Roth, Stacey, Newton, eds. Chapman and Hall, New York (1990) pp. 117-124. b) Bolin, J. T.; Ronco, A. E.; Morgan, T. V.; Mortenson, L. E.; Xuong, N.-H. *Proc. Nat. Acad. Sci. USA,* **1993**,*90*, 1078-1082.

(10) Kim, J; Rees, D. C.*Nature,* **1992**, *360*, 553-560.

(11) a) Kim, J.; Rees, D. C. *Science* **1992**,*257*, 1677-1682. b) The histogram for the Kim-Rees model in Figure 2 used distances from coordinates at 2.7 Å resolution, supplied to us by Prof. Rees and also available from the Brookhaven Protein Data Bank.

(12) Cramer, S. P. ``Biochemical Applications of X-ray Absorption Spectroscopy" in ``Extended X-ray Absorption Fine Structure," D. Konigsberger and R. Prins, Eds. Plenum, New York (1988) pp. 257-320.

(13) a) Cramer, S. P.; Hodgson, K. O.; Gillum, W. O.; Mortenson, L. E. *J. Am.*

Chem. Soc. **1978,** *100,* 3398-3407. b) Cramer, S. P., Gillum, W. O.; Hodgson, K. O.; Mortenson, L. E.; Stiefel, E. I.; Chisnell, J. R.; Brill, W. J.; Shah, V. K. *J. Am. Chem. Soc.* **1978,** *100,* 3814.

(14) Conradson, S. D.; Burgess, B. K.; Newton, W. E.; Mortenson, L. E.; Hodgson, K. O. *J. Am. Chem. Soc.* **1987,** *109,* 7507.

(15) Flank, A. M.; Weininger, M.; Mortenson, L. E.; Cramer, S. P. *J. Am. Chem. Soc.* **1986,** *108,* 1049-1055.

(16) Arber, J. M.; Dobson, B. R.; Eady, R. R.; Hasnain, S. S.; Garner, C. D.; Matsushita, T.; Nomura, M.; Smith, B. E. *Biochem. J.* **1989,** *258,* 733-737.

(17) George, G. N.; Coyle, C. L.; Hales, B. J.; Cramer, S. P. *J. Am. Chem. Soc.* **1988,** *110,* 4057-4059.

(18) Arber, J. M.; Flood, A. C.; Garner, C. D.; Gormal, C. A.; Hasnain, S. S.; Smith, B. E. *Biochem. J.* **1988,** *252,* 421-425.

(19) Harvey, I.; Arber, J. M.; Eady, R. R.; Smith, B. E.; Garner, C. D.; Hasnain, S. S. *Biochem. J.* **1990,** *266,* 929-931.

(20) Antonio, M. R.; Teo, B. K.; Orme-Johnson, W. H.; Nelson, M. J.; Groh, S.

E.; Lindahl, P. A.; Kauzlarich, S. M.; Averill, B. A. *J. Am. Chem. Soc.* **1986**, *108*, 1049-1055. This study did not report the 3.7 Å Fe-Fe interaction, but did see ~1 Fe-(O,N) near 1.8Å.

(21) a) Zimmerman, R.; Münck, E.; Brill, W. J.; Shah, V. K.; Henzl, M. T.; Rawlings, J.; Orme-Johnson, W. H. *Biochem. Biophys. Acta*, **1978**, *537*, 185-207. b) Kurtz, D. M.; McMillan, R. S.; Burgess, B. K.; Mortenson, L. E.; Holm, R. H. *proc. Natl. Acad. Sci. USA*, **1979**, *76*, 4986-4989. In addition to the 4Fe/S cube model, a 8Fe cluster model has been proposed by Hagen *et al.* based on their EPR analysis.

(22) Coucouvanis, D.; Kanatzidis, M. G.; Dunham, W. R.; Hagen, W. R. *J. Am. Chem. Soc.* **1984**, *106*, 7998-7999.

(23) Holm; R.H. *Chem. Soc. Rev.* **1981**, *10*, 455.

(24) Challen, P. R.; Koo, S. -K.; Dunham, W. R.; Coucouvanis, D. a) *J. Am. Chem. Soc.* **1990**, *112*, 8606-8607. b) Coucouvanis, D.; Challen, P. R.; Koo, S. -K.; Davis, W. M.; Butler, W.; Dunham, W. R. *Inorg. Chem.* **1989**, *28*, 4181-4183.

(25) Lu, J. in ``Nitrogen Fixation'', Newton, W. E.; Orme Johnson, W. H. eds. University Press, Baltimore (1980) v.1. p. 343.

(26) Teo, B. -K, Averill, B. A. *Biochem. Biophy. Res. Commun.* **1979,** *88,* 1454.

(27) Bolin, J. personal communication.

(28) Hales, B. J.; Langosch, D.J., and Case, E. E. *J. Bio. Chem.* **1986,** *261,* 15301-15306.

(29) Al-Ahmad, S. A.; Salifoglou, A.; Kanatzidis, M. G.; Dunham, W. R.; Coucouvanis, D. *Inorg. Chem.* **1990,** *29, 927.*

(30) Tolman, W. B.; Liu, S.; Bentsen, J. G.; Lippard, S. J. *J. Am. Chem. Soc.* **1991,** *113,* 152-164.

(31) Jaklevic, J.; Kirby, J. A.; klein, M. P.; Robertson, A. S.; Brown, G. S.; Eisenberger, P. *Sol. State Comm.* **1977,** *23, 679.*

(32) Cramer, S. P.; Tench, O.; Yocum, M.; George, G. N. *Nucl. Inst. Meth.* **1988,** *A266,* 586-591.

(33) Cramer, S. P.; Hodgson, K. O.; Stiefel, E. I.; Newton, W. O. *J. Am. Chem. Soc.* **1978,** *100,* 2748-2760.

(34) McKale, A. G.; Knapp, G. S.; Chan, S. -K. *Phys. Rev. B,* **1986,** *33,* 841-846.

(35) ``X-Ray Absorption: Principles, Applications, Techniques of EXAFS, SEXAFS, and XANES''; Prins, R.; Königsberger, D., Eds.; Wiley, New York, 1988.

(36) Cramer, S. P.; Hille, R. *J. Am. Chem. Soc.* **1985**, *107*, 8164-8169.

(37) During the fit, the total coordination number N for directly bonded Fe-X is fixed at 4, and σ is allowed to float. The best fit was obtained with 3.5 Fe-S bond and 0.5 Fe-O bond. The coordination number of Fe-Mo interaction was fixed at 0.3.

(38) Christou, G.; Mascharak, P. K.; Armstrong, W. H.; Papaefthymiou, G. C.; Frankel, R. B.; Holm, R. H. *J. Am. Chem. Soc.* **1982**, *104*, 2820-2831.

(39) Adman, E. T.; Sieker, L. C.; Jensen, L. H. *J. Bio. Chem.* **1973**, *218*, 3987-3996.

(40) Eldredge, P. A.; Bose, K. S.; Barber, D. E.; Bryan, R. F.; Sinn, E.; Rheingold, AA.; Averill, B. A. *Inorg. Chem.* **1991**, *30*, 2365-2375.

(41) Christou, G.; Hagen, K. S.; Holm, R. H. *J. Am. Chem. Soc.* **1982**, *104*, 1744-1745.

(42) Coucouvanis, D. *Accts. Chem. Res.* **1991,** *24,* 1-8.

Chapter V

Refinement of a Model for the Nitrogenase Mo-Fe Cluster Using Single

Crystal Mo and Fe EXAFS[1]

ABSTRACT

We have measured the Fe and Mo K-edge EXAFS of nitrogenase solutions and crystals. We have been able to observe a long distance (~5 Å) feature in the Fourier transform of the single crystal Mo EXAFS which we successfully fit using multiple scattering calculations. Examination of model compounds and in light of the newly derived crystallographic structure, we have been able to refine the current model of the M-center to its highest degree of accuracy to date.

Introduction

The enzyme nitrogenase catalyzes the reduction of dinitrogen to ammonia [1]. Substrate conversion is thought to occur at the M-centers, which are two $MoFe_7S_9$ clusters embedded in the α subunits of the 220,000 Dalton $\alpha_2\beta_2$ Mo-Fe protein [2]. Each M-center presumably receives electrons from a companion P-cluster, an Fe_8S_8 structure located at the α–β subunit interface. Accurate dimensions for these clusters are important for synthetic modelling, for theoretical calculations, and to permit observation of possible structural changes during the catalytic cycle. X-ray diffraction structures for Mo-Fe proteins from *C. pasteurianum* [3] and *A. vinelandii* [4] are now progressing rapidly, and models for the M-center and P-cluster structures have been presented. However, given the limited resolution of the diffraction data (2.2 Å), it is likely that the r.m.s. error in the atomic positions of these models is on the order of 0.2-0.3 Å, and that errors in atom-to-atom distances are somewhat larger. Since changes of metal-metal distances on the 0.1 Å scale are chemically significant, more accurate cluster dimensions are important. Now that the cluster frameworks have been established by the diffraction experiments, greatly improved metric information can be obtained from solution and especially single crystal EXAFS spectra.

We report here the first single crystal Fe and Mo EXAFS spectra of nitrogenase at low temperature. A new ~5 Å Mo-Fe component is observed,

along with 7 other metal-neighbor distances. These data are combined with previous Fe [5] and new solution Mo EXAFS to refine the current model for the M-center. The model is compared with a current 2.3 Å resolution electron density map for *C. pasteurianum* [3]. Although the spectroscopic results are qualitatively in complete agreement with the Kim and Rees model for the M-center, some average distances differ by ~0.2 Å. The EXAFS also suggests less variation in individual Fe-Fe or Mo-Fe distances than seen in the published Kim and Rees model - a more symmetrical Mo-Fe cluster.

Experimental

Nitrogenase Mo-Fe protein was purified from *A. vinelandii* at LSU by methods previously described [6]. Specific activities were 1800 nmol C_2H_2 reduced $min^{-1}mg^{-1}$ protein. Mo-Fe protein crystals were prepared and mounted at Purdue University [3]. The crystals are in space group P_{21} with unit cell parameters a = 69.9 Å, b = 151.2 Å, c = 121.8 Å, and β = 110.3°. The experiments were performed on beamlines 7-3 and 10-2 at SSRL, X10C and X19A at NSLS. The x-ray absorption spectra were measured at 4 K in the fluorescence excitation mode using a 13-element Ge solid state array detector [7]. The EXAFS fits were done using FEFF5 curved-wave multiple-scattering (MS) analysis software [8]. The geometry information is taken from the crystallographic results [4,9]. In the capped-prismane compound, multiple-scattering is significant for the ~3 Å feature because of the focusing effect arising from three almost linear Mo-C-O (~177°) interactions. However,

FEFF5 calculations found that multiple scattering is not significant for the nitrogenase cluster metal-metal EXAFS.

Results and Discussion

Fourier transforms of Mo and Fe K-edge EXAFS for an Av1 solution, a Cp1 crystal, and the capped-prismane $(Et_4N)_3Fe_6S_6Cl_6[Mo(CO)_3]_2$ compound [9], are shown in Figure 1. The model transform shows the expected 2.0, 2.6, and 2.9 Å first shell Mo-C, Mo-S, and Mo-Fe distances, as well as a long Mo-Fe interaction at 4.28 Å. Buried under the shorter Mo-Fe component is a multiple-scattering contribution from a Mo-C-O interaction. Fitting the EXAFS yields distances within 0.05 Å of the crystallographic values [9] (Table 1).

The Av1 solution Mo EXAFS transform exhibits two main peaks, which fit (Figure 1) as Mo-S and Mo-Fe interactions at 2.37 and 2.70 Å, along with an unresolved Mo-O,N component at 2.20 Å (Table 1). The Mo-S and Mo-Fe distances, like previous EXAFS results [10-12], are clearly shorter than both the capped-prismane model and the respective average distances of 2.46 and 2.92 Å in the Kim and Rees M-center model. As shown in the Figure, Mo EXAFS generated from the diffraction distances has different frequencies and beats (because of different distances) and damps out more rapidly (because of the greater spread in Mo-neighbor distances). In the 3-5 Å region of the Fourier transform, a number of smaller peaks are observed, which may arise
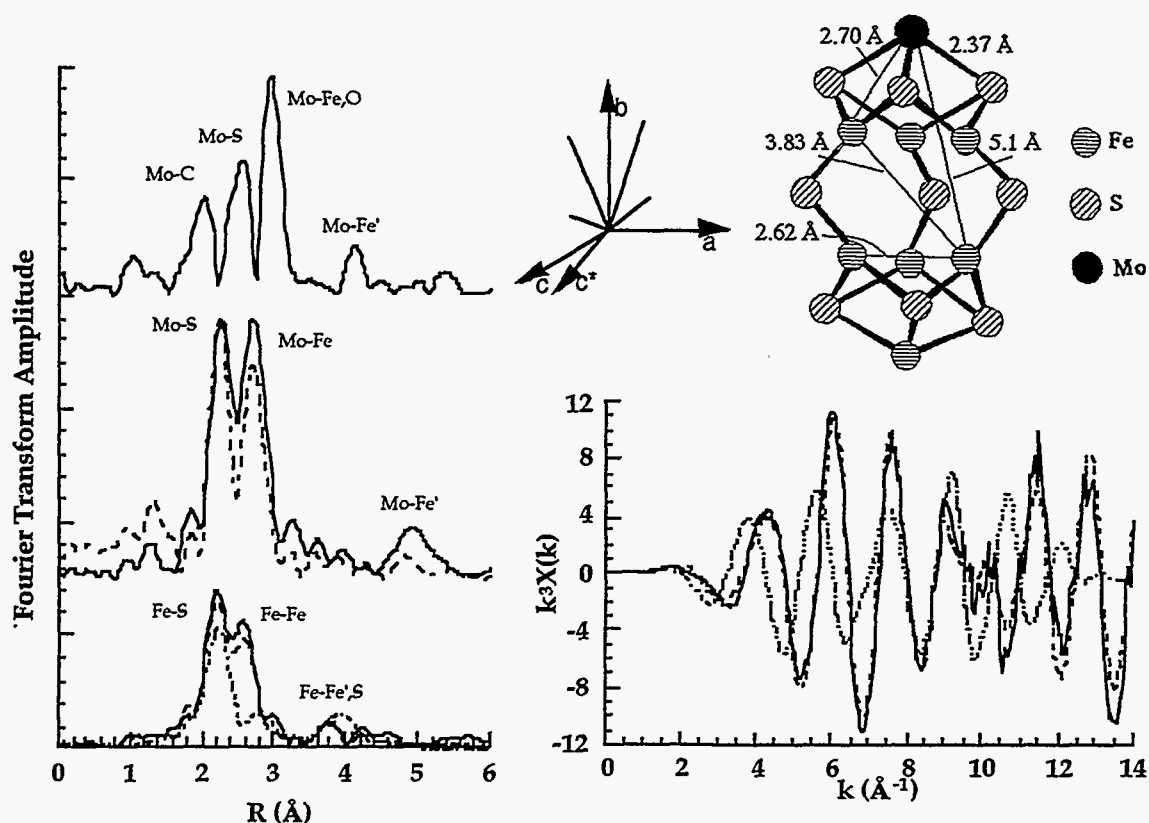
Figure 1: Left: (top) Phase corrected Fourier transforms of k^3 Mo EXAFS for $(Et_4N)_3Fe_6S_6Cl_6[Mo(CO)_3]_2$; Fourier transforms of Mo (middle) and Fe (bottom) EXAFS for Av1 protein solution (dashed) and Cp1 single crystals (solid). Right: (top) Approximate orientation of the 3-fold axes in the M-centers of MoFe protein unit cell and an assignment of EXAFS distances in the M-center; (bottom) Experimental (solid) and fitted (dashed) Mo K-edge EXAFS for MoFe protein solution. The Mo EXAFS (right bottom, dotted) and Fourier transform of Fe EXAFS (left bottom, dotted) generated from 2.2 Å crystallographic models are also shown for comparison.

from homocitrate and histidine ligand Mo-C interactions, as well as Fourier transform truncation ripple. We do not interpret these features at this time. There is also a modest peak at ~5 Å, where a second Mo-Fe interaction is expected. However, the feature is quite weak, and numerous other interactions might occur at such a distance.

We have used single crystal EXAFS to enhance this ~5 Å signal and confirm the Mo-Fe assignment. The strength of specific metal-neighbor EXAFS components varies by $\cos^2\theta$, where θ is the angle between the photon polarization vector **E** and the metal-metal vector [12]. Although there are 4 M-centers in the unit cell, their long axes tend to lie near the **bc*** plane, as shown in the Figure. Furthermore, the longer Mo-Fe vectors are only about 15° ($\cos^2 15° = 0.93$) away from these approximate 3-folds [3]. Thus, by orienting a crystal with the **E** vector parallel to the **b**-axis in the **bc*** plane, the amplitude of the ~5 Å interaction should be enhanced. In fact, a nearly twofold increase is observed (Table 1 and Figure 1). Fourier-filtering and fitting this peak yields a good fit for several Mo-Fe at 5.1 Å, close to the crystallographic value of 5.2 Å. The 2.7 Å Mo-Fe interaction also gets stronger in this orientation, while the Mo-S signal intensity is isotropic, consistent with 3 Mo-S bonds at nearly right angles to each other in each M-center.

Solution EXAFS spectra from the Fe point of view reveal Fe-Fe components at 2.63 and 3.75 Å. These values change little with orientation in the single crystal spectra, and similar Fe-Fe distances were found for isolated FeMo-cofactor [13]. The crystallographic model can be divided into two groups of Fe-Fe distances averaging 2.87 and 3.73 Å (averaging over both P-clusters and M centers). However, the 2.87 Å group has an r.m.s deviation (σ) of 0.22

Å, which does not include thermal disorder. Using the crystallographic average coordination number, the EXAFS simulation finds an r.m.s deviation (σ) of 0.09 Å, including thermal disorder. As shown in Figure 1, larger disorder in the short Fe-Fe group would result in drastically damped Fe-Fe EXAFS. We conclude that most of the short Fe-Fe distances lie within 0.1 Å of the 2.62 Å average distance. This is significantly shorter than the ~2.69-2.85 Å range seen in Fe-S clusters with 4-coordinate Fe [9,14].

Table 1: Comparison of interatomic distances found by diffraction and EXAFS for Nitrogenase Mo-Fe protein and $(Et_4N)_3Fe_6S_6Cl_6[Mo(CO)_3]_2$.

| | Mo-Fe Protein | | | | | | | | | $(Et_4N)_3Fe_6S_6Cl_6[Mo(CO)_3]_2$ | | | |
| | Avl Sol'n EXAFS[1] | | | Cpl Cryst. EXAFS[2] | | Diffr. Avl[3] | | | EXAFS[1] | | | Diff.[4] |
	N	R(Å)	σ_{tot}[5]	N′	R(Å)	R(Å)	σ_{sta}[6]		N	R(Å)	σ_{tot}[5]	R(Å)
Mo-O,N	3.0	2.21	0.075	3.9	2.20	2.24	0.012		3.0	1.97	0.048	2.020
Mo-S	3.0	2.35	0.043	3.0	2.39	2.46	0.041		3.0	2.60	0.044	2.582
Mo-Fe	3.0	2.69	0.048	3.9	2.70	2.91	0.066		3.0	2.95	0.070	2.930
Mo-Fe′	3.0	5.09	0.066	5.8	5.10	5.22	0.095		3.0	4.28	0.073	4.241
Fe-S	2.9	2.29	0.071	2.8	2.27	2.34	0.070					
Fe-Fe	3.2	2.62	0.087	3.4	2.61	2.87	0.220					
Fe-Mo	0.2	2.74	0.035	0.4	2.71	2.91	0.066					
Fe-Fe′	1.3	3.75	0.074	1.0	3.68	3.73	0.440					

1 The appropriate coordination number N was derived from the Kim and Rees model averaging over both P-clusters and M-centers.
2 The relative amplitude N' was obtained by fixing σ_{tot} at the value derived from the solution fit, and optimizing N'. This is not a coordination number, since the appropriate polarization effects have not been factored out.
3 The crystallographic value. Reference [4].
4 The crystallographic value. Reference [6].
5 Total standard deviation $\sigma_{tot.} = \sigma_{stat.} + \sigma_{thermal}$.
6 Statistical standard deviation.

In the diffraction model, the long Fe-Fe distances average to 3.73 Å with a σ of 0.442 Å. Most of the diagonal interactions among M-center Fe atoms lie near 3.85 Å (see Figure), and this is no doubt the group that the EXAFS fits find with an average distance of 3.72 Å. Although there are numerous other long Fe-Fe vectors in the 3.0 to 4.4 Å range, the EXAFS analysis cannot deal with a large number of minor components.

Altogether, the single crystal Mo and Fe EXAFS provide 8 predictions for metal-neighbor distances. Combining all the values from EXAFS, and using the geometry provided by the Kim and Rees M-center model, allows a refined model to be constructed, as shown in Figure 1. We have compared our refined model with an unbiased 2.3 Å resolution Cp1 electron density map from an ongoing x-ray diffraction study [3]. The comparison was done by refining our model as a rigid body against the Cp1 diffraction data using the program TNT [15]. This process gives a very good fit to the diffraction data, as shown by Figure 2 and a quantitative evaluation of electron density values at the atomic positions. The mean interpolated electron density values (on an arbitrary scale) in the Cp1 density map for the 7Fe and 9S atoms in the refined EXAFS model are 1886 (σ=182) and 969 (141). For comparison, the values for the current Cp1 crystallographic model, which has been refined against 2.3 Å data to R=0.17, are 1903 (191) and 928 (174). Clearly, the positions of atoms in

our model are in excellent agreement with the electron density map and in fact fit the map as well as those in crystallographic model.
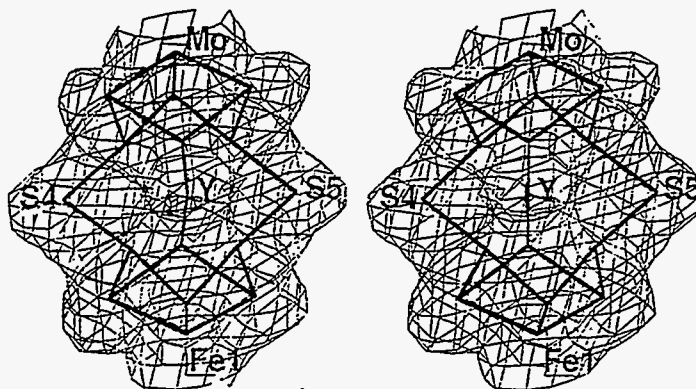
Figure 2: Comparison of the refined EXAFS model for the M-center in MoFe protein (red) and electron density map (blue). This stereo pair is oriented so that the Fe-Y-Fe bridge is towards the viewer. The electron density is from a 2.3Å resolution map calculated with experimentally determined phases (model unbiased). The contour level of the map is set at the r.m.s. value of the electron density in the asymmetric unit.

In conclusion, the structure of the intact Mo-Fe protein has been studied by single crystal Mo and Fe EXAFS spectroscopy. We observed orientation-dependence not only in the 'well-known' 2.7 Å Mo-Fe interaction, but also in a new 5.1 Å Mo-Fe component. Fe-Fe components at 2.6 Å and 3.7 Å are also stronger in the single crystal data. Combining the Mo and Fe EXAFS results with crystallographic information allows us to propose a more symmetrical M-center structure with unprecedented precision.

References

(1) B. K. Burgess in *Advances in Nitrogen Fixation Research*, (Eds.: C. Veeger, W. E. Newton), Nijhoff, Boston, **1984**, p. 103; W. Orme-Johnson, *Annu. Rev. Biophy. Chem.* **1985**, *14*, 419.

(2) V. K. Shah, W. J. Brill, *Proc. Natl. Acad. Sci. U.S.A.* **1977**, *74*, 3249.

(3) a) J. T. Bolin, A. E. Ronco, L. E. Mortenson, T. V. Morgan, M. Williamson, N.-H. Xuong in *Nitrogen Fixation: Achievements and Objectives*, (Eds.: P. Gresshoff, C. Roth, G. Stacey, W. Newton), Chapman and Hall, New York, **1990**, p. 111; b) J. T. Bolin, A. E. Ronco, T. V. Morgan, L. E. Mortenson, N. -H. Xuong, *Proc. Natl. Acad. Sci. USA*, **1993**, *90*, 1078; c) J. T. Bolin, N. Camposso, S. W. Muchmore, T. V. Morgan, L. E. Mortenson in *Molybdenum Enzymes, Cofactors and Model Systems* ACS Symposium Series, (E. Stiefel, D. Coucouvanis, W. Newton, Eds.) ACS Symposium Series 535, New York; 1993, pp 231.

(4) a) J. Kim, D. C. Rees, *Science,* **1992,** *257,* 1677; b) J. Kim, D. C. Rees, *Nature,*

1992, *360,* 553; c) M. K. Chan, J. Kim, D. C. Rees, *Science,* **1993,** *260,* 792; d) J.

Kim, D. C. Rees, pre-release entry 1MIN to the Brookhaven Protein Data

Bank.

(5) J. Chen, J. Christiansen, R. C. Tittsworth, B. J. Hales, S. J. George, D.

Coucouvanis, S. P. Cramer, *J. Am. Chem. Soc.* **1993,** *115,* 5504.

(6) B. J. Hales, D. J. Langosch, E. E. Case, *J. Bio. Chem.* **1986,** *261,* 15301.

(7) S. P. Cramer, O. Tench, M. Yocum, G. N. George, *Nucl. Inst. Meth.* **1988,**

A266, 586.

(8) J. J. Rehr, R. C. Albers, *Phys. Rev. B* **1991,** *41,* 8139; J. J. Rehr, J. Mustree de

Leon, S. I. Zabinsky, R. C. Albers, *J. Am. Chem. Soc.* **1991,** *113,* 5153.

(9) D. Coucouvanis, A. Salifoglou, M. G. Kanatzidis, W. R. Dunham, A.

Simopoulos, A. Kostikas, *Inorg. Chem.* **1988,** *27,* 4066.

(10) S. P. Cramer, K. O. Hodgson, W. O. Gillum, L. E. Mortenson, *J. Am. Chem. Soc.* **1978,** *100,* 3398.

(11) S. D. Conradson, B. K. Burgess, W. E. Newton, L. E. Mortenson, K. O. Hodgson, *J. Am. Chem. Soc.* **1987,** *109,* 7507.

(12) A. M. Flank, M. Weininger, L. E. Mortenson, S. P. Cramer, *J. Am. Chem. Soc.* **1986,** *108,* 1049.

(13) J. M. Arber, A. C. Flood, C. D. Garner, C. A. Gormal, S. S. Hasnain, B. E. Smith, *Biochem. J.* **1988,** *252,* 421.

(14) a) R. E. Palermo, R. Singh, J. K. Bashkin, R. H. Home, *J. Am. Chem. Soc.* **1984,** *106,* 2600; b) E. T. Adman, L. C. Sieker, L. H. Jensen, *J. Bio. Chem.* **1973,** *248,* 3987.

(15) D. E. Tronrud, L. F. Ten Eyck, B. W. Matthews, *Acta Crystallogr. Sect. A.* **1987**, *43*, 489.

Chapter VI

Fe and Mo EXAFS of *Azotobacter vinelandii* Nitrogenase in Partially Oxidized and Singly Reduced Forms[1]

ABSTRACT

The Fe and Mo K-edge EXAFS of the nitrogenase MoFe protein in the indigo disulfonate (IDS) oxidized form and under slow turnover conditions have been recorded. The EXAFS of the one electron reduced form E_1 was obtained as a difference spectrum between the slow turnover and resting (E_0) spectra. Average Fe-S, Fe-Fe and Fe-Mo distances of 2.33Å, 2.60Å and 2.66Å respectively, along with a second Fe-Fe distance at 3.72Å were found for E_1. The IDS-oxidized MoFe protein contains partially oxidized 'P-clusters'. For

---

this sample, average Fe-S, Fe-Fe and Fe-Mo interactions at 2.31Å, 2.65Å and 2.71Å respectively, along with the long Fe-Fe interaction at 3.74Å. Combination of the current results with previous data on resting and thionin-oxidized nitrogenase shows a general trend - a significant number of the metal-metal distances tend to contract as the enzyme becomes more reduced.

Introduction

The enzyme nitrogenase catalyzes the reduction of dinitrogen to ammonia, along with hydrogen evolution and ATP hydrolysis [1, 2, 3]. X-ray crystallography has shown that the nitrogenase MoFe protein is an $\alpha_2\beta_2$ tetramer with two unique types of metal clusters [4]. One of these, the 'P-cluster', is proposed to consist of two [Fe$_4$S$_4$] clusters bridged by two cysteinyl sulfurs and a disulfide bond formed between two of the cluster sulfurs [5], although another crystallographic model has been proposed which links the two cubes at a single sulfur [6]. The other cluster, can be viewed as a [MoFe$_3$S$_3$] fragment bridged by three inorganic sulfides to another [Fe$_4$S$_3$] cluster (Figure 1) [4,6]. This cluster, first spectroscopically identified as the 'M-center' [7], is thought to be the site of enzymatic activity, and it is extractable as the [MoFe$_7$S$_9$ + homocitrate] 'FeMo-cofactor' [8].

Along with valuable magnetic resonance and Mossbauer studies [1,2,3,7], there have been numerous EXAFS studies of MoFe protein solutions [9], crystals [10], and extracted FeMo-cofactor [11]. Since there is only one type of Mo present, the Mo EXAFS has been relatively easy to interpret, and components corresponding to Mo-O,N, Mo-S, Mo-Fe interactions at ~2.1, 2.4, 2.7 Å have been reported and assigned (Figure 1). On the other hand, the Fe EXAFS of the nitrogenase MoFe protein is complicated by the presence of 15 different types of Fe distributed over two metal clusters. The Fe EXAFS of intact nitrogenase yielded average Fe-S, Fe-Fe and Fe-Mo distances of 2.29Å,

2.62Å and 2.74Å, as well as a long Fe-Fe interaction of 3.75Å. Combination of the Fe and Mo EXAFS data with the crystallographic results recently allowed refinement of a model for the 'M center' [9].

Despite rapid progress in characterization of the resting nitrogenase system, there have not been any reports on the cluster structures once electrons are put into the 'M center'. One obstacle to characterization of the reduced enzyme is H_2 evolution by the 2-electron reduced form E_2, which returns the reduced enzyme back to the resting state E_0 [12]. The E_1 form may also be capable of reverting back to E_0 via oxidation by sulfite [13]. Information about the reduced structures is important, because most substrates or inhibitors seem to bind only after electrons are added to the 'M center'. For example, irreversible dinitrogen binding is proposed to occur at the E_3 reduction level [12]. In this current paper, we use EXAFS to examine how the average Fe-X and Mo-X distances change upon reduction to E_1, and we also investigate changes with 'P-cluster' or 'M-center' oxidation.

Experimental

Sample preparation. Nitrogenase MoFe protein was extracted from strains of *Azotobacter vinelandii* and purified by previously published methods [14]. Specific activities of purified enzyme ranged from 1800-2000 nmol C_2H_2 reduced min^{-1} mg protein^{-1} for the MoFe protein and 1400-1600 nmol C_2H_2

reduced min^{-1} mg protein^{-1} for the Fe protein. All purification steps were done under strictly anaerobic conditions. Purified fractions were stored frozen in liquid nitrogen. Protein concentration was determined by the biuret method.

To obtain a pure one-electron reduced spectrum, we examined a steady state mixture of resting and one-electron reduced MoFe protein from *Azotobacter vinelandii*, in the presence of a small amount of Fe protein. Under these conditions, all protein in the two-electron reduced state E_2, by the scheme of Lowe and Thorneley [12,15], will rapidly evolve hydrogen and be oxidized back to the resting state, E_0. Thus, a steady-state sample of nearly 50% E_0 and E_1 states can be obtained that has a negligible background contribution from the Fe protein. We measured the Fe K-edge EXAFS of these E_0+E_1 steady state samples and subtracted the 50% E_0 contribution, thus isolating an E_1 spectrum. Specifically, steady state mixtures were prepared by incubating a 5:1 molar ratio of MoFe protein:Fe protein, along with excess sodium dithionite and an ATP regenerating mixture at room temperature in a Vacuum Atmospheres glove box with an argon atmosphere. The O_2 level was held at <1.5 ppm throughout the entire procedure. The regenerating mixture consisted of 0.025 M Tris-HCl pH 7.4, with 10 mM sodium dithionite, 10 mM Mg-ATP, 150 mM creatine phosphate and 0.625 mM creatine phosphokinase. Purified MoFe protein was added to the reaction mixture first, followed by the Fe protein to start the reaction. The reaction was

allowed to proceed in the glove box for 8 minutes, at which time ethylene glycol (as a glassing agent) was added to the reaction mixture, for a final concentration of 40% ethylene glycol, and 20 mg/ml MoFe protein. Samples and simultaneously run controls were loaded into lucite EXAFS cuvettes and quartz EPR tubes simultaneously. Samples were then frozen, typically at 15 minutes from the point of addition of the Fe protein.

The sample condition was verified by EPR spectroscopy. Steady state mixture samples all showed $50 \pm 2.5\%$ reduction in the amplitude of the $S=3/2$ FeMo-cofactor signal compared to the control samples in spectra recorded at 3.2 K. EPR spectra were recorded on a computer-interfaced Bruker ER300D spectrometer with ESP 200 data collection software and an Oxford Instruments ESR-900 helium flow cryostat. Temperature was monitored with an FeAu/Chromel thermocouple positioned directly below the sample tube and monitored with and Oxford Instruments ITC-4 temperature controller.

MoFe protein with oxidized 'P-clusters' was prepared by oxidation with indigodisulfonate (IDS) [16]. EPR spectroscopy has shown that the $S=3/2$ signal, attributed to the FeMo-cofactor resting state persists [17], while signals that are attributed to 'P-cluster' oxidation appear [18]. 'P-cluster' oxidation by IDS was effected by titrating dithionite-free MoFe protein with anaerobic IDS solution prepared in 0.025 M Tris-HCl pH 7.4 and 0.2 M NaCl. The titration

proceeded until the endpoint, indicated by a persistent blue-green color. Sodium dithionite was removed from the MoFe protein by gel filtration with Sephadex G-25 (Pharmacia), eluting with anaerobic, dithionite free, 0.026 M Tris-HCl pH 7.4 and 0.2 M NaCl buffer. Eluted MoFe protein fractions were checked for residual dithionite with methyl violagen indicator. IDS oxidized samples were concentrated with Minicon membrane concentrators to a final concentration of 90-140 mg/ml. EXAFS cuvettes and quartz EPR tubes were loaded and frozen in liquid nitrogen simultaneously. All of the above procedures were done in a glove box with the O_2 level held at <1.5 ppm throughout the entire procedure. EPR spectra showed no attenuation of the S=3/2 FeMo-cofactor signal when compared to untitrated control samples. The S≥3 signal (at g=11.6 in perpendicular mode) which has been assigned to 2-equivalent oxidized 'P-clusters' was present in IDS oxidized samples [19]. Other EPR signals that are assigned to different 'P-cluster' oxidation states (S=1/2, 5/2 or 7/2) [18c,17] were not present.

Data Collection. The EXAFS spectra were measured in fluorescence mode using a Canberra Instruments 13-element Ge solid-state array detector [20]. During the measurement, the samples were maintained at 8-10K in an Oxford Instruments CF1208 liquid helium flow cryostat. Amplifier shaping times were set at either 0.5ms or 1ms, with total count rates for each channel kept below 35 Khz and 20 Khz respectively. Single channel analyzer windows were set to collect the Fe or Mo Kα signal. The spectra were calibrated by

simultaneously collecting transmission spectra of a pure metal foil, setting the first inflection point energy to be 7111.2 eV for Fe and 20,000 eV for Mo.

X-ray absorption spectra were recorded on several different beamlines. Steady state turnover MoFe protein Fe XAS data was collected on NSLS beamline X-10C, running in focused mode with Si(220) and Si(111) monochromator configurations; SSRL beamline 6-2 in focused mode and Si(111) monochromator configuration; and NSLS beamline X-19A, in unfocused mode with Si(220) monochromator configuration. IDS oxidized data was collected on NSLS beamline X-19A, in unfocused mode with a Si(111) monochromator configuration; NSLS beamline X-10C, running in focused mode with a Si(111) monochromator configuration; SSRL beamline 6-2, focused mode with a Si(111) monochromator configuration. For beamlines X-19A and 6-2, the second monochromator crystal was detuned to minimize the transmission of harmonics. For beamline X-10C, a mirror feedback system was used for rejection of harmonics [21]. Beam spot size was maintained at a maximum of ~2x12mm with focusing optics and/or tantalum slits placed at the beam exit port. The incident beam intensity was monitored with a nitrogen-filled ion chamber. Mo x-ray absorption spectra were recorded at SSRL beamline 7-3, operating in unfocused mode with a Si(220) monochromator, and at NSLS beamline X19A, in unfocused mode with a Si(220) monochromator. For Mo samples, the beam intensity was monitored with argon filled ion chambers and the spot size was maintained

by slits placed at the beam exit port.

Analysis Procedures. The use of different beamlines and monochromator crystals helped reduce systematic experimental errors associated with monochromator glitches and the overall spectral baseline. Reproducibility was checked by overlaying the data sets and comparing the EXAFS over the full range of data. The individual scans were deglitched, if necessary, using single point removal. All deglitching was performed prior to isolation of the EXAFS oscillations, so as not to induce any spline errors. The EXAFS oscillations were extracted from the raw data with a cubic spline and normalized with a Victoreen function using routine methods [22]. Values of 7131 eV for Fe and 20020 eV for Mo were used to initially define the magnitude of the photoelectron wave vector $k=[(8\pi^2 m/h^2)(E-E_o)]^{1/2}$. The EXAFS spectra were interpolated onto identical k-space grids with $\Delta k=0.05$ Å^{-1} and then averaged to form a single data set for both the singly reduced mixture (E_0+E_1) and IDS oxidized MoFe protein. The EXAFS spectrum of resting E_0 MoFe protein was also interpolated onto the same k-space grid and subtracted from the E_0+E_1 mixture to yield the EXAFS of the E_1 state.

The EXAFS spectra were Fourier transformed from k-space to R-space, and specific regions of the resulting transforms were then Fourier filtered and back-transformed as will be described later. The resulting filtered EXAFS

spectra were then fit to the single-scattering, curved-wave functional form of the EXAFS equation [23] using the McKale functions and a Levenberg-Marquardt curve fitting algorithm [24]:

$$\chi(k) = \sum_{i} \frac{N_i \gamma_i f_i(k, R_i)}{kR_i^2} e^{-2\sigma_i^2 k^2} \sin[2kR_i + \phi_i(k, R_i)]$$

where the summation is over all backscatterers at a distance R_i, with root-mean square distance deviation σ^2 and coordination number N_i. The functions $f(k,R_i)$ and $\phi(k,R_i)$ represent the distance and energy dependent, curved-wave backscattering amplitude and total phase shift respectively. The amplitude reduction factor, γ, was held fixed at 0.9 during all fits [9].

Appropriate values for the threshold energy shifts ΔE_o for Fe-X and Mo-X interactions were derived by fitting spectra of the model compounds $[Fe_6S_6Cl_6]^{3-}$ and $(CO)_3MoFe_6S_6Mo(CO)_3$ [9,25] with theoretical phase shift and amplitude functions, while constraining the distances to crystallographic values. For the $(CO)_3MoFe_6S_6Mo(CO)_3$ model, multiple scattering was taken into account for the relevant CO components. Parameters taken from model compound fit results were held fixed for all fits. The appropriate values for coordination numbers N were derived from inspection of the crystallographic models [4,5,6]. The values for the distance R and distance deviation σ^2 were

allowed to vary, with published results being used as initial values for these parameters [9,10]. For all Fe K-edge fits, the Fe-Mo interaction was held fixed at the value derived from the Mo K-edge fits, this added another element of self-consistency and reduced the degrees of freedon in the resulting fits. In fits that used the Fe-Mo distance derived from the Fe K-edge fits, the resulting split in the Fe-Fe distances was actually more pronounced.

Results and Discussion

EXAFS Fourier Transforms vs. Crystallographic Radial Distributions. In Figure 1, we compare the radial distribution functions around Fe and Mo, derived from a recent crystallographic analysis of the *C. pasteurianum* Mo-Fe protein [6], with the phase-shift corrected Fe and Mo EXAFS Fourier transforms. In the 'P cluster', the average short Fe-Fe distance is proposed to be 2.71 Å, with a root mean square deviation σ of 0.11 Å. The crystallographic data suggests that the average 'M center' Fe-Fe distance is a shorter 2.60 Å, with a root mean square deviation σ of .13 Å. The current range of EXAFS data does not allow resolution of these 2 groups of distances, but the 'split-shell' distribution can be modeled by curve-fitting. At longer distances, the 'M center' has an important group of 'cross-cluster' Fe-Fe interactions at an average distance of 3.61 Å. The single-scattering analysis of these interactions is complicated by multiple-scattering paths that have similar total lengths, However, multiple scattering is not important for the interactions at distances < 3 Å.
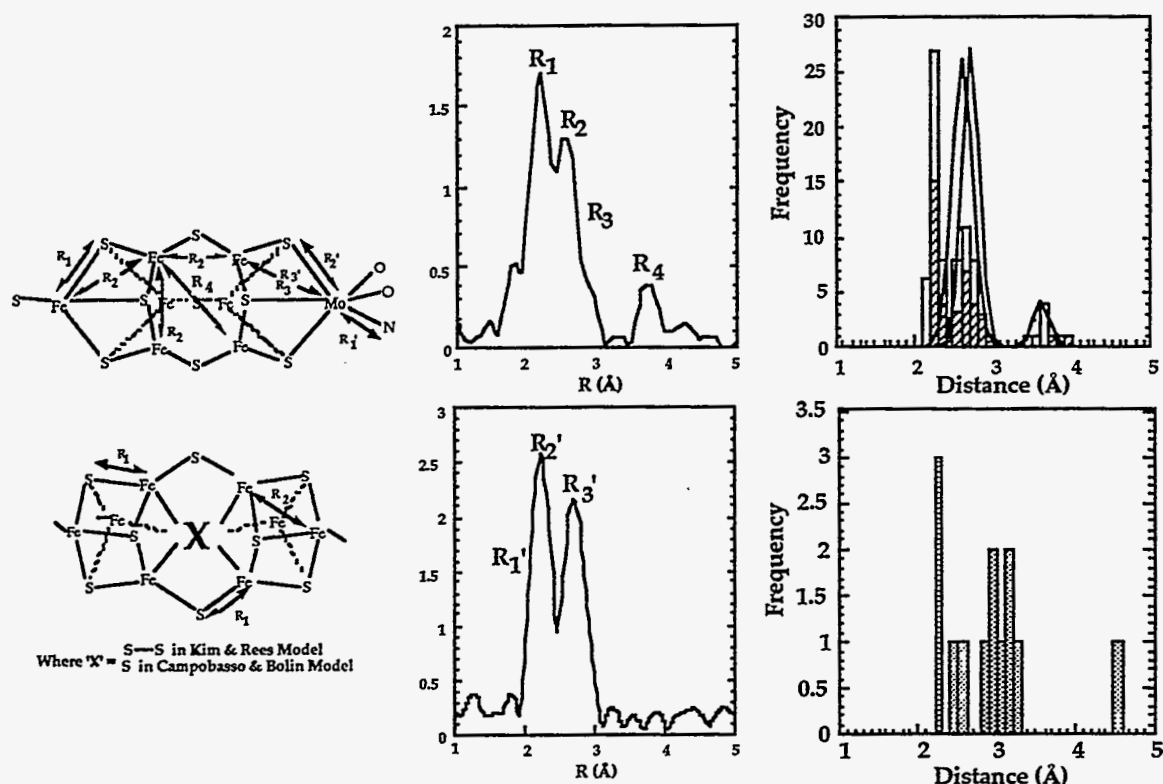
Figure 1: (left) Proposed models for the FeMo-cofactor and P-cluster with some representative distances derived from EXAFS. The accompanying Fourier transforms for the Fe K-edge (top, center) and Mo K-edge (bottom, center) have labels that show the correspondence between the Fourier transform features and the distances shown on the models. The histograms were derived from recent crystallographic coordinates [6] and correspond to interactions from Fe (top, right) and Mo (bottom, right). The gaussian curves shown on the Fe histogram represent the spread in similar Fe-Fe distances in the P-cluster and M-center.

IDS Oxidized MoFe Protein. The Fe EXAFS Fourier transform of IDS-oxidized MoFe protein (P^{2+}/M) is compared with resting (P/M) and thionin-oxidized (P^{2+}/M^+) protein in Figure 2. Like thionin-oxidized MoFe protein, there is a decrease in the intensity of the ~2.7Å transform peak, compared to the resting MoFe protein transform. The 3.7Å peak, first observed in the extracted FeMo-cofactor [11], remains of similar magnitude in the IDS data as in the resting enzyme [9]. Since the oxidation level of the 'M-center' is not

affected by IDS oxidation, a large change in the 'M-center' distances is not expected. For curve fitting analysis, the Fe EXAFS of the IDS oxidized MoFe protein was Fourier transformed (k=3-14.5Å^{-1}) and then the R-space region from 0-6Å was back-transformed. To limit the number of free parameters in the simulations, the Fe-Mo distance was fixed at the 2.71Å value obtained from the Mo K-edge EXAFS of resting enzyme. The best 4 shell single-scattering fit with this constraint (Table I and Figure 2), found average Fe-S and Fe-Fe distances of 2.31Å and 2.65Å, as well as a long Fe-Fe component at 3.74Å.

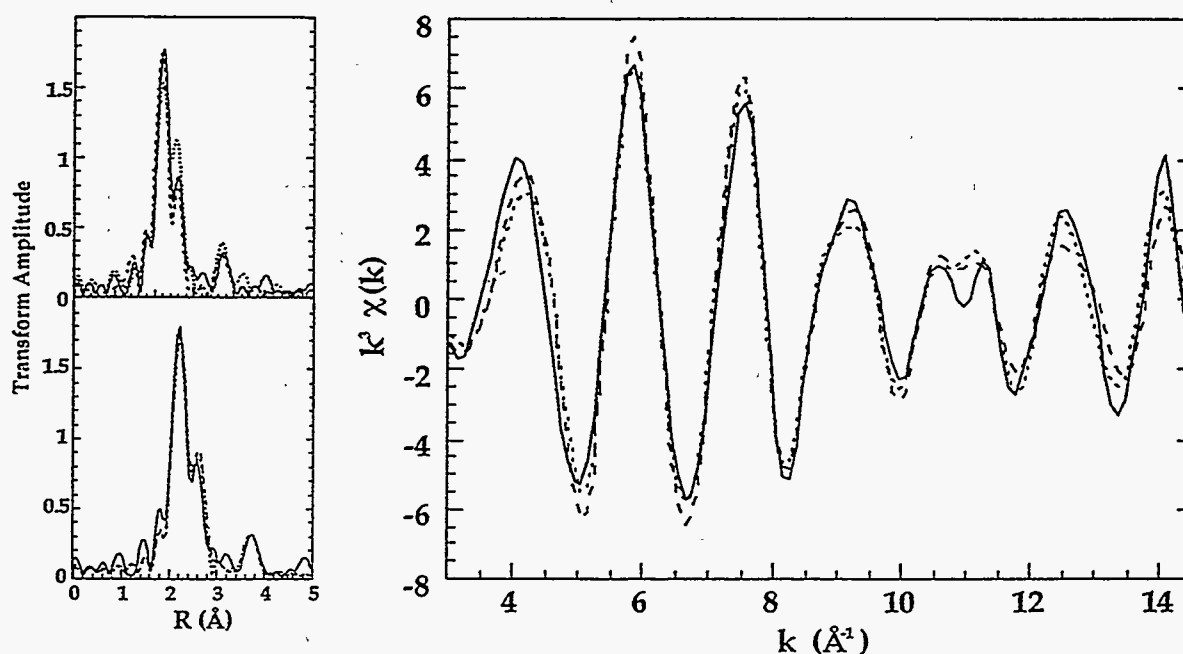**Figure 2:** *Left, top:* Fourier transforms (corrected for Fe) of IDS oxidized protein (shown solid) Thionine oxidized (shown dashed) and resting MoFe protein (shown dotted). *Left, bottom:* Fourier transforms of IDS oxidized protein with resulting fits *Right:* Fourier filtered EXAFS of IDS oxidized nitrogenase (shown solid) shown with the 4 component (short dash) and 5 component (dashed) fit results.

Since the fit to the data is good but not perfect, the significance of multiple scattering in the Fe EXAFS was estimated using the FEFF5 program [26]. For these calculations, a symmetrized model for the core of the 'M-center' was constructed by constraining all similar Fe-S and Fe-Fe distances to the same value. The largest multiple scattering contribution found for the 'M-center' was a 3.6Å Fe-S-Fe path (the distance refers to the total path length divided by 2) that was only 7% of the largest Fe-S interaction at ~2.3Å, and ~25% of the 3.7 Å single-scattering Fe-Fe interaction. Examination of 'P-cluster' multiple scattering is complicated by the current ambiguity in the crystal models. Although examination of the core 4Fe-4S cube structures does not show any multiple scattering in the <3Å region, the possibility of multiple scattering in the >3Å range is strongly dependent on the overall symmetry within the cubes and their bridging geometry. The Mo EXAFS data was also checked for multiple scattering. Although significant multiple scattering paths for the histidine and homocitrate ligand groups were found, their contributions are also not important in the range below ~3Å used for the current analysis.

The average Fe-Fe distance of 2.65Å is not significantly different from the 2.63Å value for resting enzyme. However, an important result from the 4-shell IDS fit is the large σ value of ~0.09 Å for the 2.65Å Fe-Fe interaction. Typical values for thermal motion disorder of short bridged metal-metal distances are on the order of 0.05Å or less, so a σ of ~0.09 Å indicates a

measure of 'static' as opposed to 'thermal' disorder. One interpretation is that upon oxidation, all Fe-Fe distances in nitrogenase become more disordered, with the average value at 2.65Å. A simple alternative is that the 'P-cluster' Fe-Fe interactions have all expanded while the cofactor interactions have remained the same, so as to give an overall average of 2.65Å.

Examination of the radial distribution function derived from the resting nitrogenase crystal structure [5,6] suggests dividing the short Fe-Fe interactions into two subgroups, one with an average Fe-Fe coordination number N=1.6, accounting for Fe-Fe interactions in the 'M center', and another with N=1.6 corresponding to Fe-Fe interactions in the 'P-cluster'. Splitting the radial distribution is also chemically reasonable, since the 3-coordinate Fe in the 'M center' might be expected to have stronger Fe-Fe bonding interactions and significantly shorter distances. Previous EXAFS analyses of isolated FeMo-cofactor also found relatively shorter average Fe-Fe distances than for the intact protein [11].

With the current range of data, using the resolution criterion that $\Delta R \cong \pi/2\Delta k$ [27], we can not truly resolve backscatterers that have similar atomic numbers and that have distances that differ by less than 0.14Å . We nevertheless explored a simple 'split-shell' model, allowing for two different short Fe-Fe components, while constraining as many other parameters as possible. Although the fit did not improve if the σ_{Fe-Fe} values were

constrained at 0.057 Å (the value found for the $[Fe_6S_6Cl_6]^{3-}$ prismane complex [25]), the fit did improve somewhat with unconstrained σ_{Fe-Fe} values (Table I). The constrained five component fit (Table I) found short Fe-Fe interactions at 2.59Å and 2.70Å. Although part of the improvement is expected because of the additional degrees of freedom introduced by the new interaction, the distances are chemically reasonable. With 15 different types of Fe in nitrogenase, the true radial distribution is no doubt more complex than this simple model.

The previously reported [9] resting enzyme and thionin-oxidized enzyme Fe EXAFS were reinterpreted with the new model (Table 1). As expected, the thionin-oxidized spectrum, which produced the largest σ_{Fe-Fe} values in the 4-shell fits, gave the largest difference in Fe-Fe distances when fit with the 'split-shell' model, with an average 'M-center' short Fe-Fe of 2.61Å, compared to a 'P-cluster' short Fe-Fe of 2.74Å. The 2.74Å Fe-Fe distance is the same as that seen in a synthetic Fe_4S_4 cluster [28], while the 2.61Å distance compares favorably with the 2.64Å value reported for isolated FeMo-co [11]. Split-shell analysis of the resting enzyme Fe EXAFS also gave a relatively short 'M center' Fe-Fe distance of 2.58 Å and a 'P-cluster' average of 2.67Å, compared to respective crystallographic values (at room temperature) of 2.60Å and 2.71. As noted by others, the 'M-center' distances are near the bond length range for Fe-Fe bonds [29].

Singly Reduced MoFe Protein. Mo and Fe EXAFS spectra and Fourier transforms, illustrating the extraction process for obtaining the reduced E_1 spectra, are shown in Figure 3. The noise level for the pure E_1 spectrum is increased; this is expected for a spectral subtraction, and the contribution from the ±2.5% error in the $E_0 + E_1$ is small enough to be neglected in the subtraction. To provide additional constraints for the more complex Fe analysis, we first fit the Mo EXAFS data. The Mo EXAFS Fourier transform was filtered to select the region from 1-3Å and backtransformed. The fits yielded Mo-(O,N), Mo-S, and Mo-Fe distances of 2.13, 2.36, and 2.65 Å respectively (Table II). Of these distances, the most significant result is the apparent 0.06 Å contraction in the Mo-Fe distance. This Mo-Fe distance and the associated σ of 0.063 Å were then used as constraints in the analysis of the Fe EXAFS of the E_1 enzyme (P/M⁻).

For the Fe EXAFS of E_1, the dominant transform feature is still the ~2.3Å Fe-S interaction. The 2.7Å (Fe-Fe plus Fe-Mo) peak that is resolved in the E_0 transform is only a shoulder in the $E_0 + E_1$ mixture, becoming even less visible in the pure E_1 transform. However, in the 3-5Å region, the Fe-Fe interaction at ~3.75Å from 'cross-cluster' cofactor interactions is still obvious in the pure E_1 spectrum, which helps maintain confidence in the subtraction procedure.
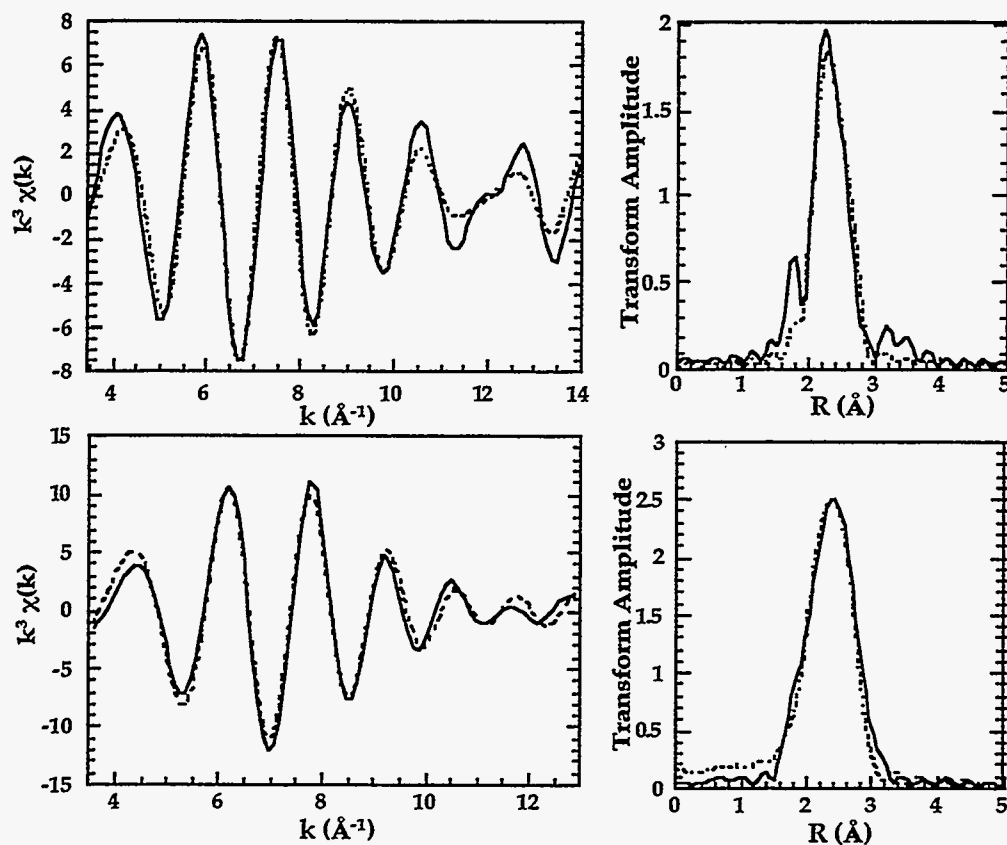
Figure 4: *Top:* Fe EXAFS and Fourier transform for the filtered data (shown solid) and the fit (shown dashed) *Bottom:* Mo EXAFS of the filtered data (shown solid) and resulting fit (shown dashed)

We have illustrated the degree of 'M-center' 'breathing' between oxidized and reduced forms, implied by the EXAFS analysis, by constructing a symmetrized model based on the crystallographic geometry (Figure 6). Of course, there is no reason for all the 'M center' short Fe-Fe distances to be the same, and the structure in the protein may be distorted from this idealized picture. For example, the central iron cage could elongate or flatten, and one possible distortion that is consistent with the EXAFS is also illustrated.
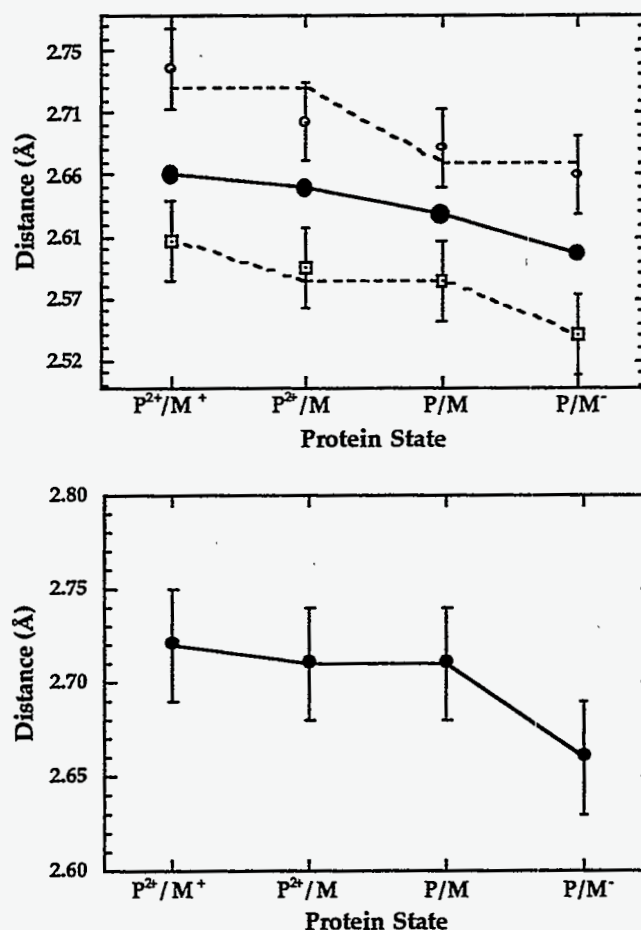
Figure 5: Plots showing the trends in metal-metal interactions during protein reduction/oxidation. *Top:* the variation in Fe-Fe distances as the protein goes from fully oxidized (P^{2+}/M^+) to reduced (P/M^-). The center plot indicates the variation in the 4 component fits while the outer data points indicate the trend demonstrated in the split-shell fits *Bottom:* trend in the Fe-Mo interaction for different redox states of the protein.

Since the publication of a crystallographic model for the MoFe protein, much attention has been paid to location of possible N_2 binding sites; this is essential to understanding the mechanism of enzymatic activity. The current model can be thought of as creating a sort of 'cage' surrounded by Fe. In the

resting structure, this cage is ~0.5Å too small for N_2 to enter, so it has been suggested that the cluster breaks open to accommodate dinitrogen [31]. Deng and Hoffman have considered the expansion of the cage required to accommodate an interior N_2, they suggest that the Fe-Fe distances would have to expand to ~3.0 Å [32]. They and others have also considered binding sites on the outer surface of the cage [5,32,33]. Our data, ranging from thionin-oxidized (3-electron oxidized per $\alpha\beta$ subunit) to the E_1 form (1-electron reduced) show that, at least over this range of reduction, the average Fe-Fe distance seen by EXAFS does not expand, rather it contracts slightly.

The significance of the current results can be interpreted in two different ways. On one hand, the general similarity of all of the Mo and Fe EXAFS for oxidized and reduced nitrogenase suggests that profound transformations have not occurred. For example, the persistence of the long 'cross-cluster' 3.75Å Fe-Fe peak in all of the Fe EXAFS Fourier transforms suggests that these interactions, and hence the overall 'M center' structures, are similar in resting, oxidized, and 1-electron reduced forms. Although this result is not very surprising, rearrangements were certainly possible. There are numerous examples of clusters which rearrange their polyhedral geometries upon electron transfer [34]; The potential influence of valence electrons on the molecular geometry of clusters has been appreciated for more than 30 years [35].

The ~0.07Å contractions proposed for Fe-Fe distances between thionin-oxidized and 1-electron reduced forms are chemically reasonable in magnitude. For example, a 0.06Å contraction with "change of electron count" occurs when $S_2Ni_3(C_5H_5)_3$, with a mean Ni-Ni distance of 2.80 Å [36], is converted to 2.74 Å in the recently isolated monocation [37], a further contraction to 2.53 Å occurs in $(C_5H_5)_3Ni_3(CO)_2$, with 4 fewer electrons for Ni-Ni interactions from the original cluster [38]. Another example of shortening on removal of an electron is the complex $SFeCo_2(CO)_9$ [39], where the average metal-metal distance is 0.08 Å shorter than the 2.64 Å distance in $SCo_3(CO)_9$ [35]. These changes can be rationalized by an electron counting scheme formulated by Lauher for trinuclear clusters that considers the highest 3 of the 27 molecular orbitals formed from the metal atomic orbitals as antibonding [40].

Instead of expanding, metal-metal distances do sometimes contract with addition of electrons. For example, in aqueous Mo chemistry, the Mo-Mo distances shorten from ~2.6Å for Mo(V)-Mo(V) dimers to ~2.5 Å in the Mo(IV) trimer all the way to 2.12 Å in the Mo(II) dimer [41]. However, most such examples occur for early transition metals which are initially lacking sufficient d-electrons for metal-metal bonding. The contraction we observe in Fe-Fe and Mo-Fe distances upon reduction is thus surprising and perhaps important. Both in $[Fe_4S_4]^{n+}$ clusters, where n = 1, 2, 3, and in $[Fe_6S_6^{n+}L_6]^{n-}$

prismanes, where n = 2, 3, addition of electrons results in expansion of the Fe-Fe distances [42]. Also, in the [Fe6S6ⁿ⁺L6(Mo(CO)3)2]ⁿ⁻ capped prismanes where n = 2, 3, the more reduced species has longer Mo-S and Mo-Fe distances [25].
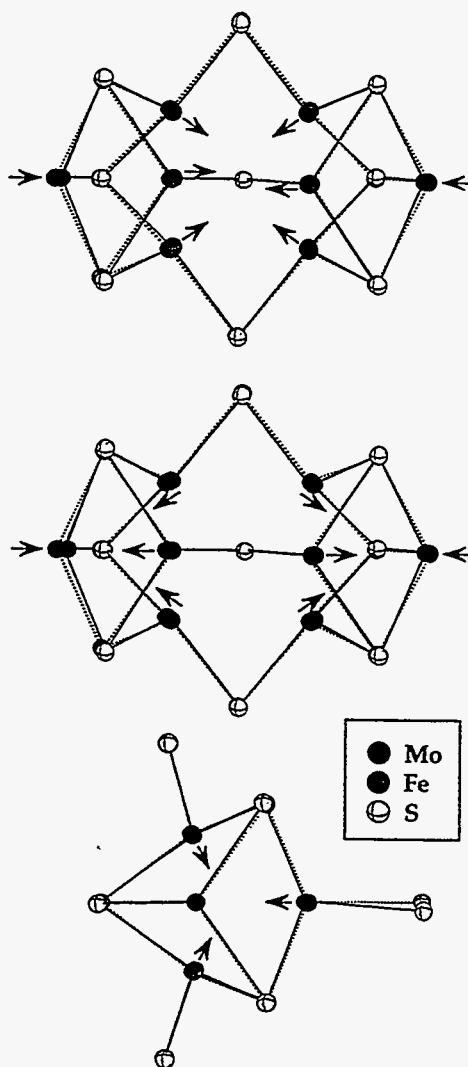

Figure 6: Two possible structural rearrangements of the M-center in the singly reduced state. The models have been symmetrized using distances derived from EXAFS and the arrows indicate the direction of change in atom positions.

Since the majority of documented metal clusters expand as electrons are added, the observed contraction in EXAFS average distances begs for some

explanation. The clusters certainly catalyze special chemistry, so there could be something special about the bonding of the 3-coordinate Fe centers in the 'M center' cage. There is one alternative explanation that we cannot yet refute, related to EXAFS artifacts from asymmetric distribution functions. Eisenberger and Brown observed an anomalous apparent contraction with increasing temperature in Zn metal EXAFS [43]. They found that in the case of an asymmetric distribution function that tails to longer distances, the EXAFS is disproportionately sensitive to the sharp leading edge of the distribution and yields distances shorter than the arithmetic average. The same effect might occur for particular distortions of the 'M center' and 'P cluster'. For example, if the 'M center' expanded along its 3-fold axis, while contracting for 2 of the Fe-Fe distances in the planes perpendicular to the long axis, a broad asymmetric distribution could be created. Calculations performed by Deng and Hoffman indicate the possibility of asymmetry where the MoFeS fragment of the 'M-center' may exhibit a contraction, while the FeS end of the 'M-center' may undergo a small expansion [44].

Asymmetrical structural changes are well documented not only for biological [Fe_4S_4] clusters and their models, but in other small molecules such as the [{$Fe(\mu_3$-S)Cp$\}_4$] series [34c]. The neutral cluster has 2 short (2.64 Å) and 4 long (3.36 Å) Fe-Fe distances [45], going to 2 short (2.64 Å), 2 medium (3.19 Å), and 2 long (3.32 Å) Fe-Fe distances upon 1 electron oxidation [46] and 4 short (2.83 Å) and 2 long (3.25 Å) Fe-Fe distances with the next oxidation [47]. Thus,

although the cluster volume and average Fe-Fe distance expands with reduction, the leading edge of the Fe-Fe distribution function actually moves to shorter distances. Relevant to possible distortions in hexanuclear clusters, we note that in $Co_6C(CO)_{12}S_2$, the Co-Co distances along the long axis of the trigonal prism are 2.67 Å compared to the 2.44 Å distances in the planes perpendicular to the long axis [48]. In the $[Fe_6C(CO)_{16}]^{2-}$ complex, the short Fe-Fe distances range from 2.55 to 2.72 [49]. The shortest metal-metal vectors in both cases are perpendicular to the approximate 3-fold axes. In this spirit, we again divided the Fe-Fe component for the reduced Fe EXAFS (P/M⁻) and got distances of 2.56 Å (N=1.1,σ2=0.00263 Å²), 2.66 Å (N=1.6, σ2=0.00311 Å²) and 2.84 Å (N=0.5, σ2=0.00115 Å²) with a factor of two improvement in the quality of fit value (F, see table I). Although there are far too many variables for this type of fit to be definitive, it does help to illustrate that there are many possible distortions that may be masked within our resolution limits.

Whether or not the especially short Fe-Fe distances represent arithematic averages, it is clear that at least some of the Fe-Fe distances are especially short. The proposed reduced 'M-center' value of 2.54 Å (a -0.04 Å contraction from the resting protein) is similar to Fe-Fe distances in clusters with Fe-Fe bonding. The Fe-Fe distances proposed for the 'M-center' are close to the 2.52 Å interaction in $Fe_2(CO)_9$, where metal-metal bonding has been proposed [50] (or denied [51]). There is also a strong analogy with the cluster

$S_2Fe_3(CO)_9$ [35] which contains Fe-Fe distances of 2.59 Å (ave) and 3.37 Å.

The possible expansion of the 'P-cluster' upon oxidation may also be significant, but the lower symmetry makes it harder to model. For the IDS oxidized MoFe protein, for which only the 'P-cluster' changes oxidation state, we observed an expansion of the overall average short Fe-Fe distance from 2.62 to 2.65Å. Using the split-shell model (although the data does not allow unambiguous resolution of 'P-cluster' and 'M-center' distances), one interpretation is that the average 'P-cluster' Fe-Fe distance expands from ~2.67 to ~2.72Å (these numbers are arrived at by taking the average distances from the thionine and IDS oxidized results and the average of resting and reduced results). Recent crystallographic modeling of the MoFe protein has also indicated that, when exposed to agents capable of oxidizing 'P-clusters', there is an expansion in the average Fe-Fe distances in the 'P-cluster' [52].

Summary

The metal clusters in nitrogenase 'breathe' slightly upon reduction or oxidation. Contrary to expectations, a significant fraction of the average Fe-Fe distances contract as the enzyme becomes more reduced. Comparison with known cluster models compounds suggests that rearrangement during further reduction of the enzyme may be significant and deserve additional study.

Table I: *Azotobacter vinelandii* nitrogenase Fe K-edge EXAFS fitting

	Fe-S [b]			Fe-Fe [c]			Fe-Mo [d]			Fe-Fe' [e]			[a] F
	N	R,Å	$\sigma^2\times10^{-5}$ Å²	N	R,Å	$\sigma^2\times10^{-5}$ Å²	N	R,Å	$\sigma^2\times10^{-5}$ Å²	N	R,Å	$\sigma^2\times10^{-5}$ Å²	
Thionine Ox. P²⁺/M⁺													
4 components	3.6	2.29	555	3.2	2.66	988	0.2	2.72	443	1.3	3.73	369	0.46
5 components	3.6	2.29	501	1.6 / 1.6	2.61 / 2.74	333 / 333	0.2	2.72	443	1.3	3.74	395	0.56
5 components	3.6	2.29	521	1.6 / 1.6	2.62 / 2.73	430 / 549	0.2	2.72	443	1.3	3.73	425	0.41
IDS Oxidized P²⁺/M													
4 components	3.6	2.31	506	3.2	2.65	871	0.2	2.71	290	1.3	3.74	347	0.61
5 components	3.6	2.31	475	1.6 / 1.6	2.59 / 2.70	333 / 333	0.2	2.71	290	1.3	3.75	344	0.79
5 components	3.6	2.31	482	1.6 / 1.6	2.60 / 2.71	355 / 548	0.2	2.71	290	1.3	3.74	469	0.57
Resting P/M													
4 components	3.6	2.31	599	3.2	2.63	634	0.2	2.71	295	1.3	3.73	361	0.72
5 components	3.6	2.31	582	1.6 / 1.6	2.58 / 2.67	333 / 333	0.2	2.71	295	1.3	3.74	392	0.84
5 components	3.6	2.31	566	1.6 / 1.6	2.60 / 2.68	376 / 538	0.2	2.71	295	1.3	3.74	360	0.69
Reduced P/M⁻													
4 components	3.6	2.33	578	3.2	2.60	938	0.2	2.66	398	1.3	3.72	245	0.19
5 components	3.6	2.33	655	1.6 / 1.6	2.54 / 2.66	333 / 333	0.2	2.66	398	1.3	3.72	243	0.25
5 components	3.6	2.33	632	1.6 / 1.6	2.54 / 2.66	479 / 534	0.2	2.66	398	1.3	3.72	251	0.17

a F is defined by $\Sigma|\chi_{exp}-\chi_{calc}|/npts$, *b* $\Delta E_0=-3eV$, *c* $\Delta E_0=-8eV$, *d* $\Delta E_0=-6eV$, *e* $\Delta E_0=-10eV$

Table II: *Azotobacter vinelandii* nitrogenase Mo K-edge EXAFS fitting

	Mo-O/N [b]			Mo-S [c]			Mo-Fe [d]			[a]F
	N	R,Å	$\sigma^2 \times 10^{-5}$,Å^2	N	R,Å	$\sigma^2 \times 10^{-5}$,Å^2	N	R,Å	$\sigma^2 \times 10^{-5}$,Å^2	
Thionine Oxidized (P^{2+}/M^+)	3.0	2.17	317	3.0	2.38	399	3.0	2.72	435	0.51
Resting (P/M)	3.0	2.20	283	3.0	2.36	340	3.0	2.71	310	0.87
Reduced (P/M^-)	3.0	2.13	263	3.0	2.36	178	3.0	2.65	397	0.54

a   F is defined by $\Sigma \, |\chi_{exp} - \chi_{calc}| \, / \, npts$

b $\Delta E_0 = 3.3 eV$

c $\Delta E_0 = -14 eV$

d $\Delta E_0 = -10 eV$

References:

1) Orme-Johnson, W.H. *Annu. Rev. Biophys. Biophys. Chem.* **1985**, *14*, 419-459.

2) Eady, R.R. *Adv. Inorg. Chem.* **1991**, *36*, 77-102.

3) Hageman, R.V.; Burris, R.H. *Proc. Natl. Acad. Sci. U.S.A.* **1978**, *75*, 2699-2702.

4) Kim, J.C.; Rees, D.C. *Science* **1992**, *257*, 1677.

5) Chan, M.K.; Kim, J.; Rees, D.C. *Science* **1993**, *260*, 792-794.

6) Campobasso, N., *Ph.D. Thesis, Purdue U.*, **1994.**

7) Zimmerman, R.; Munck, E.; Brill, W.J.; Shah, V.K.; Henzl, M.T.; Rawlings, J.; Orme-Johnson, W.H. *Biochim. Biophys. Acta,* **1978**, *537*, 185-207.

8) Burgess, B.K. *Chem. Rev.* **1990**, *90*, 1377-1406.

9) Chen, J.; Christiansen, J.; Tittsworth, R.C.; Hales, B.J.; George, S.J.; Coucouvanis, D.; Cramer, S.P. *J. Am. Chem. Soc.* **1993**, *115*, 5509-5515.

10) a) Flank, A.M.; Weininger, M.; Mortenson, L.E.; Cramer, S.P. *J. Am. Chem. Soc.* **1986**, *108*, 1049-1055. b) Chen, J.; Christiansen, J.; Campobasso, N.; Bolin, J.T.; Tittsworth, R.C.; Hales, B.J.; Rehr, J.J.; Cramer, S.P. *Angew. Chem. Int. Ed. Engl.* **1993**, *32*, 1592-1594.

11) a) Conradson, S.D.; Burgess, B.K.; Newton, W.E.; Mortenson, L.E.; Hodgson, K.O. *J. Am. Chem. Soc.*, **1987**, *109*, 7507. b) Arber, J.M.; Flood, A.C.; Garner, C.D.; Gormal, C.A.; Hasnain, S.S.; Smith, B.E. *Biochem. J.* **1988**, *252*, 421-425. c) Antonio, M.R.; Teo, B.K.; Orme-Johnson, W.H.; Nelson, M.J.; Groh, S.E.; Lindahl, P.A.; Kauzlaurich, S.M.; Averill, B.A. *J. Am. Chem. Soc.* **1986**, *108*, 1049-1055.

12) Lowe, D.J.; Thorneley, R.N.F. *Biochem J.* **1984**, *224*, 877-886.

13) Henzl, M.T., *Ph.D. Thesis, U. Wisc.,* **1980.**

14) Burgess, B.K.; Jacobs, D.B.; Stiefel, E.I. *Biochim. Biophys. Acta* **1980**, *814*, 198-209.

15) Fisher, K.; Lowe, D.J.; Thorneley, R.N.F. *Biochem J.* **1991**, *279*, 81-85.

12) Lowe, D.J.; Thorneley, R.N.F. *Biochem J.* **1984**, *224*, 877-886.

16) Orme-Johnson, W.H.; Paul, L.; Meade, J.; Warren, W.; Nelson, M.; Groh, S.; Orme-Johnson, N.R.; Munck, E.; Huynh, B.N.; Emptage, M.; Rawlings, J.; Smith, J.; Roberts, J.; Hoffman, B.; Mims, W.B.; in *Current Perspectives in Nitrogen Fixation* ; Gibson, A.H.; Newton, W.E., eds.; Elsevier, North-Holland, New York, **1981**, 79-84.

17) Munck, E.; Rhodes, H.; Orme-Johnson, W.H.; Davis, L.C.; Brill, W.J.; Shah, V.K. *Biochim. Biophys. Acta* **1975**, *400*, 32-53.

18) (a) Hagen, W.R. in *Iron Sulfur Proteins* (Sykes, A.G., Cammack, R. Eds), *Advances in Inorganic Chemistry*, **1992**, Vol. 38, 165-122, Academic Press, New York.

(b) Surerus, K.K.; Hendrich, M.P.; Christie, P.D.; Rottgardt, D.; Orme-Johnson, W.H.; Munck, E.J. *J. Am. Chem. Soc.* **1992**, *114*, 8579-8590. (c) Plerik, A.J.; Wassink, H.; Haaker, H.; Hagen, W.R. *Eur. J. Biochem.* **1993**, *212*, 51-61.

19) Tittsworth, R.C.; Hales, B.J. *J. Am. Chem. Soc.* **1993**, *115*, 9763-9767.

20) Cramer, S.P.; Tench, O.; Yocum, M.; George, G.N. *Nucl. Instrum. Methods A266*, **1988**, 586-591.

21) Sansone, M.; Via, G.; George, G.N.; Meitzner, G.; Hewitt, R., in *X-Ray Absorption Fine Structure* (S.S. Hasnain, Ed.) **1991**, pp 656-658, Ellis Horwood Ltd., W. Sussex, England.

22) Cramer, S.P.; Hodgson, K.O.; Stiefel, E.I.; Newton, W.O. *J. Am. Chem. Soc.* **1978**, *100*, 2478-2760.

23) McKale, A.G.; Knapp, G.S.; Chan, S-K. *Phys. Rev. B* **1986**, *33*, 841-846.

24) Marquardt, D.W. *J. Soc. Ind. Appl. Math.* **1963**, *11*, 443.

25) Coucouvanis, D. in *Molybdenum Enzymes, Cofactors and Model Systems*; Stiefel, E.I.; Coucouvanis, D.; Newton, W.E. eds.; ACS Symposium Series 535, New York; **1993**, 304-331.

26) (a) Rehr, J.J.; Mustre de Leon, J.; Zabinsky, S.I.; Albers, R.C. *J. Am. Chem. Soc.* **1991**, *113*, 5135. (b) Mustre de Leon, J.; Rehr, J.J.; Zabinsky, S.I.; Albers, R.C. *Phys. Rev. B*, **1991**, *44*, 4146.

27) Lee, P.A.; Citrin, P.H.; Eisenberger, P.; Kincaid, B.M. *Rev. Mod. Phys.* **1981**, *53*, 769-806.

28) Laskowski, E.J.; Frankel, R.B.; Gillum, W.O.; Papaefthymiou, J.R.; Ibers, J.A.; Holm, R.H. *J. Am. Chem. Soc.* **1978**, *100*, 5322-5337.

29) G. Gonzalez-Moraga, *Cluster Chemistry*, Springer-Verlag: Berlin, **1993.**

30) *X-Ray Absorption: Principles, Applications, Techniques of EXAFS, SEXAFS and XANES*; Prins, R.; Köningsberger, D., eds.; Wiley: New York, **1988.**

31) a) Schrauzer, G.N.; Docemeny, P.A.; Palmer, J.G. *Zeitschrift Fur Naturforschung Section B-A Journal of Chemical Sciences*, **1993**, *48*, 1295-1298 b) Schrauzer, G.N. *J. Inorg. Biochem.* **1993**, *51*, 370.

32) Deng, H.; Hoffman, R. *Angew. Chem. Int. Ed. Engl.* **1993**, *32*, 1062-1065.

33) Dance, I. G. *Aust. J. Chem.* **1994**, *47*, 979-990.

34) (a) Rieck, D, F.; Rae, A. D.; Dahl, L. F. *J. C. S. Chem. Comm.* **1993**, 585-587. (b) Drake, S. R.; Barley, M. H.; Johnson, B. F. G.; Lewis, J. *Organometallics* **1988**, *7*, 806-812, and references cited therein. (c) Geiger, W. E.; Connelly, N. G. *Adv. Organomet. Chem.* **1985**, *24*, 87-130, and references cited therein. (d) Geiger, W. E. *Prog. Inorg. Chem.* **1985**, *33*, 275, and references cited therein.

35) Wei, C. H.; Dahl, L. F. *Inorg. Chem.* **1965**, *4*, 493-499.

36) Vahrenkamp, H.; Uchtman, V. A.; Dahl, L. F. *J. Am. Chem. Soc.* **1968**, *90*, 3272-3273.

37) North, T. E.; Thoden, J. B.; Spencer, B.; Dahl, L. F. *Organometallics* 1993, 12, 1299-1313.

38) Maj, J. J.; Rae, A. D.; Dahl, L. F. *J. Am. Chem. Soc.* **1982**, *104*, 3054.

39) Hock, A.; Mills, O.S. *Advances in the Chemistry of Coordination Compounds*, The Macmillan Co.: New York, **1961.**

40) Lauher, J.W. *J. Am. Chem. Soc.* **1978**, *100*, 5305-5315.

41) Cramer, S.P.; Gray, H.B.; Dori, Z.; Bino, A. *J. Am. Chem. Soc.* **1979**, *101*, 2770-2772.

42) Stiefel, E. I.; George, G. N. in *Bioinorganic Chemistry*, Bertini, I.; Gray, H. B.; Lippard, S. J.; Valentine, J. S. eds. University Science, Mill Valley **1994**, 365-453 and references cited therein.

43) Eisenberger, P.; Brown, G.S. *Sol. State. Comm*, **1979**, *29*, 481-484.

44) Deng, H; Hoffman, R. personal communication.

45) a) Schunn, R.A.; Fritchie, C.J.; Prewitt, C.T. *Inorg. Chem.* **1966**, *5*, 892   b) Wei, C.H.; Wilkes, G.R.; Treichel, P.M.; Dahl, L.F. *Inorg. Chem.* **1966**, *5*, 900.

46) Toan, T.; Fehlhammer, W.P.; Dahl, L.F. *J. Am. Chem. Soc.* **1977**, *99*, 400-407.

47) Toan, T.; Teo, B.K.; Ferguson, J.A.; Meyer, T.J.; Dahl, L.F. *J. Am. Chem. Soc.*, **1977**, *99*, 408-416.

48) Bor, G.; Gervasio, G.; Rossetti, R.; Stanghellini, P.L. *J.C.S. Chem. Comm.*, **1978**, 841-843.

49) Baird, N.C.; West, R.M. *J. Am. Chem. Soc.*, **1971**, *93*, 3073-3074.

50) (a) Barnett, B.L.; Krüger, C. *Angew. Chem. Int. Ed. Engl.*, **1971**, *10*, 910-911 Mealli, C.; Prosperio, D.M. *J. Organomet. Chem.* **1990**, *386*, 203-28.

51) Reinhold, J.; Hunstock, E. *New. J. Chem.* **1994**, *18*, 465-471.

52) Bolin, J. personal communication.

Chapter VII

Characterization of the Apodinitrogenase protein

## from *Azotobacter vinelandii* using EXAFS[1]

ABSTRACT

The cofactorless apodinitrogenase protein from *Azotobacter vinelandii* MoFe protein has been investigated using EXAFS spectroscopy. We have found Fe-S and Fe-Fe distances of 2.34 Å and 2.85 Å along with a second Fe-Fe interaction at 3.05 Å. The first shell Fe-Fe distance is much longer than what is typically found for other Fe-S clusters. Comparison with simulated EXAFS generated for the two current crystallographic models for the Fe-S 'P-clusters' shows no spectral homology. Although it is possible that the metal centers in Apo I are arranged differently than intact P-clusters, it is more likely that the metal clusters are extremely disordered. With a wide range of Fe-Fe distances, the amplitudes and distances found by EXAFS could be significantly in error.

---

[1] J. Christiansen, M.J. Homer, G.P. Roberts, R.C. Tittsworth, B.J. Hales, S.P. Cramer to be submitted to Biochemistry.

Introduction

Biological nitrogen fixation is catalyzed by the nitrogenase enzyme system, which consists of a smaller (~65 kDa) Fe protein and a larger (~220 kDa) MoFe protein [1]. A 4Fe-4S cluster in the Fe protein transfers electrons to the MoFe protein, coupled with ATP hydrolysis. Inhibitor [2], and presumably substrate binding occurs at the $MoFe_7S_9$ 'M-center' cluster [3] in the MoFe protein. This protein is an $\alpha_2\beta_2$ tetramer whose peptide is encoded by the *nifK* and *nifD* genes. The MoFe protein also contains a structurally unique 8Fe:8-9S P-cluster [4].
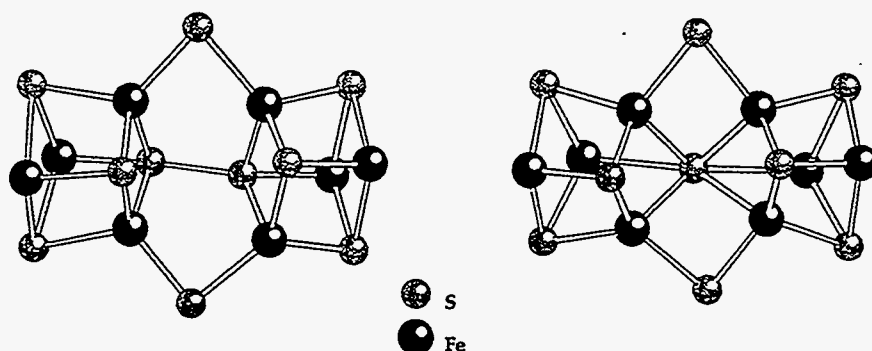
Scheme 1: Two proposed models for the MoFe protein P-cluster. *(left)* model proposed by Kim and Rees, a disulfide bond joining the two Fe-S cube fragments. *(right)* The model proposed by Campobasso and Bolin, a single sulfur is joining the two cube fragments.

Crystallographic models for the wild type nitrogenase MoFe protein have been published [5,6]. Although there is general agreement on the structure of the M-center, there is still some discrepancy in the structures proposed for the P-clusters. The current model of Kim and Rees suggests two 4Fe-4S cubes bridged by two cysteinyl sulfurs and a disulfide bond, while the model of Campobasso and Bolin involves a single sulfur joining the two 4Fe-

4S fragments (Scheme 1).
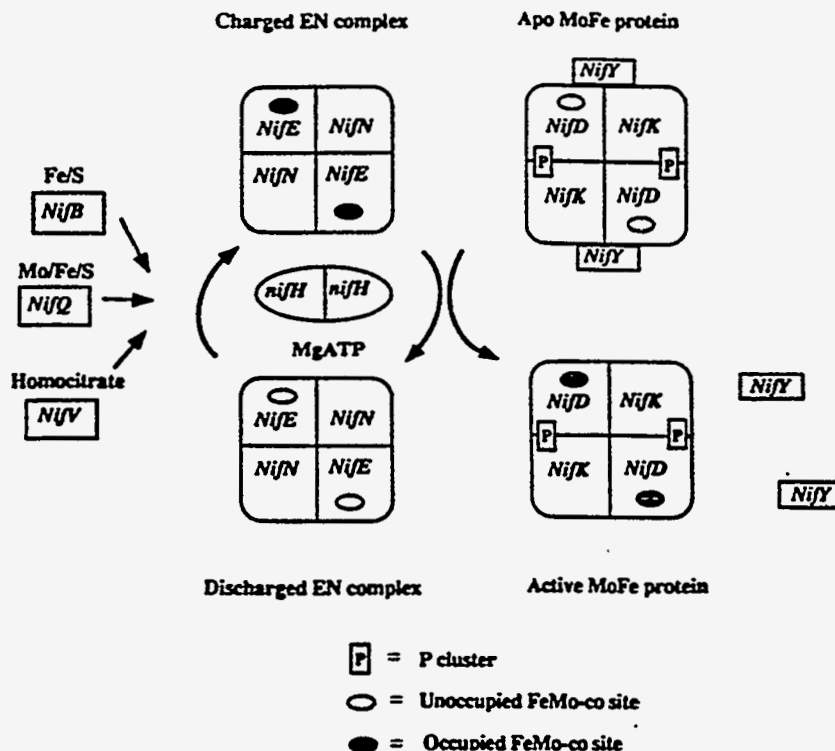
Scheme 2: Overall schematic of nitrogenase biosynthesis. The nifB, NifQ and nifV gene products are probably involved in FeMo-co biosynthesis and homocitrate synthesis. The nifN and nifE genes form a scaffold protein with a tetrameric structure. Apodinitrogenase does not contain FeMo-co, but does contain the NifY product. Upon addition of FeMo-co, NifY dissociates and leaves intact MoFe protein. From ref [8].

Several *nif* genes, including *nifQ, -B, -V, -N, -E and -H* have been implicated in the construction, and possibly insertion, of FeMo-co [7,8] (Scheme 2). Among these, a protein resulting from strains with a mutation in the *nifB* gene has been purified [9-11]. This protein, referred to as "Apo 1", does not contain the M-center but apparently possesses intact P-clusters. Apo I protein by itself does not reduce dinitrogen, but is activated *in vitro* upon addition of purified FeMo-co in a regenerating mixture containing Fe protein

and MgATP [11].

In an early attempt to purify the Apo I protein from *Klebsiella pneumoniae*, the highest specific activity achieved was ~500 nmol C_2H_2 reduced/(min·mg protein) [9]; compared to >2000 nmol C_2H_2 reduced/(min·mg protein) for wild type MoFe protein. Another purification involving *Azotobacter vinelandii* reported specific activities of 1900 nmol C_2H_2 reduced/(min·mg protein), but only 70% purity [10]. In 1990, Paustian and co-workers [11] devised a purification protocol for *Azotobacter vinelandii* which gave >95% purity and specific activity of ~2200 nmol C_2H_2 reduced/(min·mg protein), comparable to those achieved with wild type MoFe protein. They also demonstrated that Apo I copurifies with a small, tightly bound ~20 kDa protein, resulting in an $\alpha_2\beta_2\delta_2$ hexamer. Later studies [12] have shown that this additional δ protein is the product of the nifY gene and dissociates from the hexamer upon activation by FeMo-co, resulting in the $\alpha_2\beta_2$ tetramer found in wild type MoFe proteins.

High purity and high activity Apo I, has not yet been spectroscopically characterized. Previous MCD studies of *Klebsiella pneumoniae nifB*-mutants showed some similarities to wild type MoFe protein during redox titrations, but an EPR signal in the resting state was attributed to a contaminating species [13]. A better understanding of Apo is important for

understanding the mechanism of MoFe protein construction. Also, a better understanding of the Apo I protein may allow the properties of the P-cluster to be studied spectroscopically without interfering contributions from the M-center.

Experimental Procedures

Protein Purification and Characterization. Apo 1 was purified by methods previously described [12]. Assays for dinitrogenase activity and activation of Apo 1 have also been previously described [11]. Apo 1 used in these experiments had a specific activity of 1400-1500 nmol C_2H_2 reduced/(min·mg protein). Protein levels of Apo 1 were measured by quantitative amino acid analysis by the Microchemical Facility at the University of Minnesota (Minneapolis, MN). Metal content of the purified samples was determined with an Applied Research Laboratories 34000 Inductively Coupled Plasma - Atomic Emission Spectrophotometer at the University of Wisconsin Soil and Plant Analysis Laboratory (Madison, WI). Purified Apo 1 had ~13 Fe and ~0.02 Mo atoms per hexamer, while analysis of a purified control dinitrogenase MoFe protein (specific activity = 2300 nmoles of ethylene produced/min/mg) showed ~27 Fe and ~1.8 Mo per tetramer. EXAFS samples were loaded into lucite cuvettes, previously washed in dithionite, under anaerobic conditions. The cells are 3mm high and 1 mm deep. A 6μm polypropylene film was used to seal the cuvettes.

XAS data collection: To reduce and bracket experimental errors, three XAS data sets were collected from different sample preparations on two different beamlines using different monochromator configurations: 1 set on National Synchrotron Light Source beamline X10C, with a Si(111) monochromator configuration and running in focussed mode; and 2 sets on Stanford Synchrotron Radiation Laboratory beamline 7-3 with Si(220) monochromator configuration and running in unfocussed mode. For harmonic rejection on beamline 7-3, the second monochromator crystal was detuned to 60-70% of maximum intensity. A mirror feedback system was used for harmonic rejection on beamline X10C [14]. Beam spot size was maintained at less than 1 x 7 mm either by adjustments to hutch slits (BL 7-3) or adjustments to beamline focussing optics (X10C). Beam intensity was monitored by nitrogen filled ion chambers. The absorption edge for an iron metal foil was collected in parallel with protein data using a three ion chamber configuration(Scott, 1985), and the energy was calibrated by defining the first inflection point energy of the foil spectrum as 7111.2 eV.

XAFS spectra were collected in fluorescence mode using a Canberra Industries 13-element Ge solid state array detector [16]. Single channel analyzer windows were set to collect the Fe $K\alpha$ emission and total incoming count rates were kept below 35 KHz. The amplifier shaping times were 0.5µs. Samples were loaded under cryogenic conditions and maintained at ~10 K in an Oxford Instruments CF1208 liquid helium flow cryostat.

EXAFS analysis procedures: EXAFS oscillations were extracted from the raw data with a cubic spline and Victoreen normalization by routine methods [17]. Scans were deglitched using single point removal, if necessary, and all deglitching was performed prior to spline removal to minimize the introduction of spurious oscillations. A value of 7131 eV was used to define the initial magnitude of the photoelectron wave vector $k=[(8\pi^2 m/h^2)(E-E_0)]^{1/2}$. Individual EXAFS data sets were then overlayed and compared over the full range of data. After confirming reproducibility, data sets were interpolated onto identical k-space grids and averaged together.

EXAFS spectra were fit to the single-scattering, curved wave functional form of the EXAFS equation [18] using a Marquardt curve-fitting algorithm [19]:

$$\sum_i \frac{N_i \gamma_i f_i(k,R_i)}{kR_i^2} e^{-2\sigma_i^2 k^2} sin[2kR_i + \phi_i(k,R_i)]$$

where the summation is over all backscatterers at a distance R, with root mean square distance deviation σ^2, and coordination number N. The energy and distance dependent phase $\phi(k,R)$ and amplitude $f(k,R)$ functions were derived from general use, single scattering FEFF5 [20] calculations and tabulated in the spirit of the commonly used McKale tables [18] for these functions. The amplitude reduction factor, γ, was held fixed at 0.9 to account

for intrinsic processes which reduce the EXAFS amplitude. Values for small threshold energy shifts, ΔE_0, were derived from fits performed on an $(EtN)_3(Fe_6S_6Cl_6)CH_3CN$ prismane [21] using the methods just described and fixing distances and coordination numbers at well defined crystallographic values.

Results

Figure 1 compares the Fe K-edge of Apo I with that of the resting wild type MoFe protein. The overall edge structures are very similar - a relatively strong 1s->3d transition at ~7112 and a relatively broad overall peak about 20 eV higher. The shape does not show sharp features present in oxidatively damaged MoFe protein [22]. The strength of the dipole forbidden 1s -> 3d pre-edge feature consistent with a non-centrosymmetric Fe geometry [23-24], present in resting MoFe protein at ~7113 eV is also visible in the Apo I sample.

The EXAFS spectrum for Apo 1 is shown in Figure 2. Unlike other Fe-S protein EXAFS, there is no clear beat pattern. The Fourier transform is dominated by a peak at ~2.3 Å with weaker peaks in both the long and short distance sides. The tentative Fe-Fe peak at 2.8 Å in the Fourier transform is small compared with that in other 2Fe and 4Fe systems [25]. Surprisingly, the EXAFS is more like that reported for a 2Fe plant ferredoxin than for a 4Fe cluster [25].
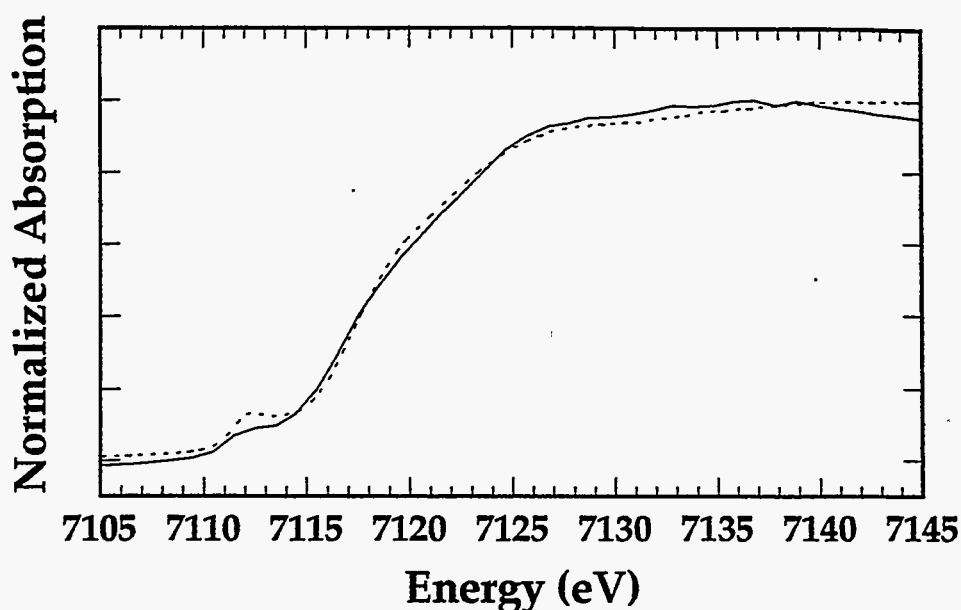
Figure 1: Comparison of the Fe K-edges for Apo I (solid) and wild type MoFe protein (dashed).

For comparison with the Apo I data, the EXAFS and corresponding Fourier transform for a 4Fe-4S ferredoxin (Figure 2) are also shown. The normal 4Fe-4S cluster exhibits a beat pattern in the EXAFS around $k=7$ Å^{-1}, and the Fourier transform shows two peaks corresponding to the Fe-S interactions at ~2.3 Å and Fe-Fe interactions at ~2.7 Å. For additional comparison, we calculated theoretical EXAFS based on current models for the P-cluster deposited in the Brookhaven Protein Databank by Kim, et. al. [26] and a model proposed by Campobasso and Bolin [6]. The spectra were simulated by averaging the contributions from each Fe site in the crystallographic P-cluster models (Figure 2). Because of the relatively wide variation in Fe-S and Fe-Fe distances, the model put forth by Kim and Rees shows reduced amplitude in both the EXAFS and Fourier transform. There is not a strong beat pattern in the EXAFS and the ~2.8 Å peak in the Fourier

transform is much smaller than the ~2.3 Å Fe-S peak. In contrast,

simulations using the P-cluster model proposed by Campobasso and Bolin [6]

show a strong beat pattern in the EXAFS and two nearly identical peaks in the
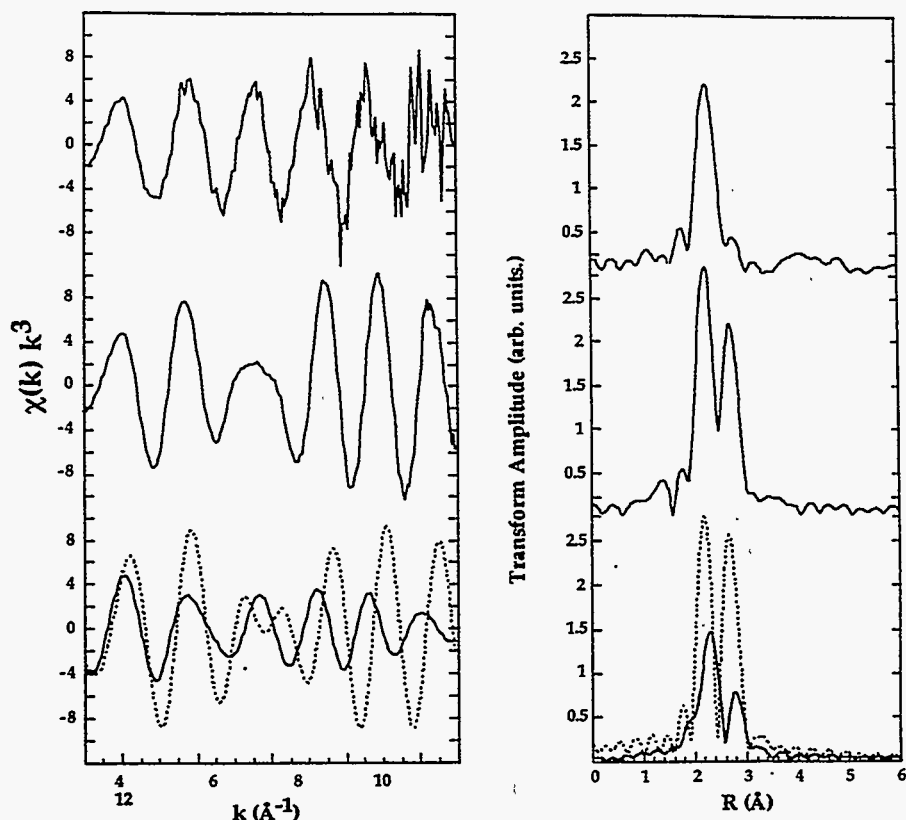
Figure 2: (*top*) EXAFS and Fourier transforms for nitrogenase Apo I. (*middle*) EXAFS and Fourier transform for a 4Fe-4S ferredoxin (courtesey of Dr. Graham N. George, SSRL). (*bottom*) EXAFS and Fourier transforms for the crystallographic modesl proposed by Kim and Rees (solid) and Campobasso and Bolin (dotted).

corresponding Fourier transform. This is because the latter model is far

more regular in Fe-S and Fe-Fe distances, similar to the 4Fe-4S ferredoxin

For curve fitting analysis the EXAFS for Apo 1 was filtered and

backtransformed on the range R=0.5-3.3 Å. After filtering, the dominant peak

in the Fourier transform was modeled as a single shell of 4 Fe-S interactions at ~2.3 Å (Table I). By holding this interaction fixed and adding a second Fe-Fe shell with σ^2 and ΔE_0 set at reasonable values, the fit quality for various combinations of N and R can be measured. Using this method, an Fe-Fe shell was added, with ΔE_0 derived from the model cluster, $(EtN)_3(Fe_6S_6Cl_6)CH_3CN$ [21]. Two search profiles were generated - one with σ^2 from the $(EtN)_3(Fe_6S_6Cl_6)CH_3CN$ model compound and a broader distribution was simulated by approximately doubling this value. The resulting search profiles for both distributions are shown in Figure 3. After inserting the minimum values for N and R, the component was allowed to float to further reduce fit error. Before optimization, the search profile found the best Fe-Fe distance at 2.85 Å, which did not change significantly upon refinement. The resulting fit and accompanying Fourier transform is shown in Figure 3.

With the first two shells fixed, a search profile was generated to examine the possibility of another interaction at a longer distance. The contour plot that was generated for this search profile is also illustrated in Figure 3. Two results are immediately clear - (1) there is no minimum found in the immediate vicinity of 2.7-2.9 Å, indicating that the single Fe-Fe interaction modelled in the second shell is sufficient, (2) The only minimum in this particular space is when the third Fe-Fe shell has an N~0.6 and R~3.06. When this component was added back into the fit and the values of R and σ^2

were allowed to float and stabilize, the fit showed an improvement of 27% (Table I) and the resulting fit is shown in Figure 2 (bottom). By comparison with the two shell fit, one can see the three shell fit demonstrates much better behavior at high k and the low k region of the EXAFS shows some improvement.
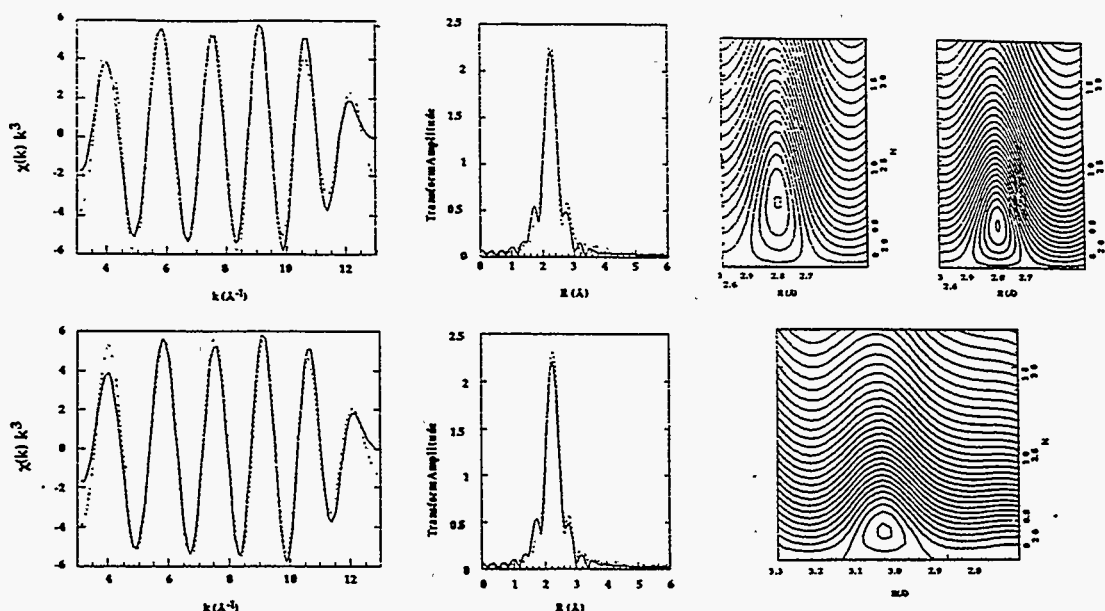
Figure 3: (top) Fe K-edge EXAFS of nitrogenase Apo I filtered data (solid) and the resulting fits (dashed). (*top*) Fit results for a single Fe-Fe interaction. (*bottom*) Fit results for two separate Fe-Fe interactions. (*top, right*) Search profiles for the first shell Fe-Fe interaction using a large σ^2 (left) and small σ^2 (right). (*bottom, right*) Search profile for a second Fe-Fe interaction.

Discussion

From what is already known about P-cluster structure, one would expect that the EXAFS from Apo I would be similar to the EXAFS of 4Fe clusters (Figure 2), at least in the range below 3Å. Examination of both the direct EXAFS and the Fourier transforms (Figure 2) shows that this is not the case.

Unfortunately, there are several possible explanations for this discrepancy. Since the Fe-Fe peak is weak, one obvious explanation is that Apo I does not possess bridged 4Fe clusters, but rather has Fe arranged in some type of 2Fe-2S geometry. However, power saturation EPR studies of this Azotobacter vinelandii Apo I indicate that the metal centers may behave as 4Fe-4S clusters [27]. Furthermore, quantitative fitting of the EXAFS results in an Fe-Fe distance of 2.86 Å, which is much longer than the 2.7-2.8 Å Fe-Fe distances reported for other 2Fe-2S clusters [28]. The Fe-S distance of 2.34 Å is comparable to distances found in these systems.

The fits allow for a second long Fe-Fe component at ~3.06 Å (Table I). The possibility that this interaction could be attributed to the carbons coordinated to S_{cys} ligands was investigated. The resulting quality of fit was 17% worse than Fe-Fe fit for 1.6 carbons at ~3.15 Å. A search profile was also generated for the possibility of an O/N ligand at ~2 Å and no minimum was found.

Previous EXAFS studies of wild type MoFe protein from *Azotobacter vinelandii* [29] gave an overall average Fe-Fe distance of 2.64Å. A recent Fe K-edge EXAFS study tried to separate the contributions from the two metal centers and results implied that the average P-cluster Fe-Fe distance is ~2.68 Å [30]. This value is close to that in the crystallographic P-cluster model put

forth by Campobasso and Bolin [6] which has a relatively narrow distribution of Fe-Fe distances with an average of 2.69 ± .03 Å. In contrast, the crystallographic model proposed by Kim and Rees [26] has a very broad distribution of Fe-Fe distances with an average of 2. 96 ± 0.20 Å. Examination of the simulated EXAFS and Fourier transforms from these two models are very different from the spectra resulting from Apo I.

The low oxidation state proposed for the P-clusters (all Fe^{2+}) [31] may have something to do with the flexibility and possible distortions of these clusters. Although model systems at the $Fe^{2.5+}$ oxidation level are relatively symmetrical [28], we note that for $[Cp_4Fe_4S_4]^0$ [32], the Fe-Fe distances range from 2.63 Å to 3.37 Å. So, it is plausible that the cluster in Apo I is still topologically an 8Fe center, but with a multitude of Fe-Fe distances. In such a case, the EXAFS values may not give a true arithmetic average [33].

Although we cannot make a definitive statement as to the true nature of the Apo I metal clusters, the data does show several things of interest. The Fe-Fe distances are much longer than what is found in typical Fe-S clusters [28,32]. However, it is probable that the metal clusters in Apo I are highly disordered, so an unambiguous coordination and distance assignment is not possible. It is clear that the Apo I metal clusters show little to no structural homology with the two models currently proposed for the wild type MoFe protein P-cluster. Since EPR signals arising from oxidized P-clusters in wild

type MoFe protein have been characterized [34], further studies of this high purity Apo I protein in these oxidized forms may provide further information about the Fe-S clusters in Apo I.

Table I: Results of Fe K-edge EXAFS Fitting of Apodinitrogenase

	N	R (Å)	σ^2 (Å^{2}x10^5)	F^c
2-component				
Fe-S^a	4.0	2.34	464	0.55
Fe-Fe^b	1.0	2.85	720	
3-component				
Fe-S^a	4.0	2.34	469	0.40
Fe-Fe^b	1.0	2.85	440	
Fe-Fe'^{b}	0.4	3.05	769	

^{a} ΔE_0=-1.8 eV

^{b} ΔE_0=-7.2 eV

^{c} as defined by $(\Sigma [f_{expt}\text{-}f_{fit}]^2 k^6)/npts$

References

(1) Orme-Johnson, W.H. *Ann. Rev. Biophys. Biophys. Chem.* **1985**, *14*, 419.

(2) Christie, P. *Personal Communication.*

(3) Burgess, B.K. *Chem. Rev.* **1990** *90*, 1377.

(4) Kim, J., Rees, D.C. *Biochemistry* **1994**, *33*, 389.

(5) Kim, J., Rees, D.C. *Science* **1992**, *257*, 1677.

(6) Campobasso, N. *Ph.D. Thesis*, Purdue U. **1994**.

(7) Triplett, E.W., Roberts, G.P., Ludden, P.W. & Handelsman, J. *ASM News* **1989**, *55*, 15-21.

(8) Dean, D.R., Bolin, J.T. & Zheng, L. *J. Bacteriol.* **1993**, *175*, 6737-6744.

(9) Hawkes, T.R. & Smith, B.E. *Biochem. J.* **1983**, *209*, 43-50.

(10) Burgess, B.K., Yang, S.-S., You, C.-B., Li, J.-G., Friesen, G.D., Pan, W.-H., Steifel, E.I., Newton, W.E., Conradson, S.D., Hodgson, K.O. in *Current*

Perspectives in Nitrogen Fixation Gibson, A.H. & Newton, W.E., eds.; Australian Academy of Science, Canberra; **1981**, pp 71-74.

(11) Paustian, T.D., Shah, V.K. & Roberts, G.P. *Biochemistry* **1990**, *29*, 3515-3522.

(12) Homer, M.J., Paustian, T.D., Shah, V.K. & Roberts, G.P. *J. Bacteriol.* **1993**, *175*, 4907-4910.

(13) Robinson, A.E., Richards, A.J.M., Thomson, A.J., Hawkes, T.R. & Smith, B.E. *Biochem. J.* **1984**, *219*, 495-503.

(14) Sansone, M., Via, G., George, G.N., Metizner, G. & Hewitt, R. in *X-Ray Absorption Fine Structure*, Hasnain, S.S., ed.; Ellis Horwood Ltd., West Sussex, England; **1991**, pp 656-658.

(15) Scott, R.A. *Methods Enzymol.* **1985**, *117*, 414.

(16) Cramer, S.P., Tench, O., Yocum, M., George, G.N. *Nucl. Instrum. Methods* **1988**, *A266*, 586.

(17) Cramer, S.P., Hodgson, K.O., Stiefel, E.I., Newton, W.O. *J. A m.* Chem. Soc. **1978**, *100*, 2478.

(18) McKale, A.G., Knapp, G.S., Chan, S.-K. *Phys. Rev. B* **1986,** *33,* 841-846.

(19) Marquardt, D.W. *J. Soc. Ind. Appl. Math.* **1963,** *11,* 443.

(20) a) Mustre de Leon, J., Rehr, J.J., Zabinsky, S.I., Albers, R.C. Phys. Rev. B **1991,** *44,* 4146. (b) Rehr, J.J., Mustre de Leon, J., Zabinsky, S.I., Albers, R.C. *J. Am. Chem. Soc.* **1991,** *113,* 5135.

(21) Coucouvanis, D. in *Molybdenum Enzymes Cofactors and Model Systems* Stiefel, E.I., Coucouvanis, D., Newton, W.E., eds.; ACS Symposium Series 535, New York; **1993,** pp 304-331, *and references therein.*

(22) Cramer, S.P. *Ph.D. Thesis,* Stanford University, **1977.**

(23) Randall, C.R., Shu, L.J., Chiou, Y.M., Hagen, K.S., Ito, M., Kitajima, N., Lachiotte, R.J., Zang, Y., Que, L., Jr. *Inorg. Chem.* **1995,** *34,* 1036.

(24) Roe, A.L., Schneider, D.J., Mayer, R.J., Pyrz, J.W., Que, L., Jr. *J. Am. Chem. Soc.* **1984,** *106,* 1676.

(25) Teo, B.-K., Shulman, R.G., Brown, G.S., Meixner, A.E. *J. Am. Chem. Soc.*

1979, *101*, 5624.

(26) Kim, J., Rees, D.C. *Nature* **1992**, *360*, 553.

(27) Tittsworth, R.C. Personal communication.

(28) Holm, R.H.; Ibers, J.A. in *Iron-Sulfur Proteins* W. Lovenberg, ed.; Academic Press, New York; **1977**, pp. 205.

(29) Chen, J., Christiansen, J., Tittsworth, R.C., Hales, B.J., George, S.J., Coucouvanis, D., Cramer, S.P. *J. Am. Chem. Soc.* **1993**, *115*, 5509.

(30) Christiansen, J., Tittsworth, R.C., Hales, B.J., Cramer, S.P., *J. Am. Chem. Soc. in press*

(31) Orme-Johnson, W.H. in *Molybdenum Enzymes, Cofactors and Model Systems* Stiefel, E.I., Coucouvanis, D., Newton, W.E., Eds.; ACS Symposium Series 535, Washington DC; **1993**, pp 257.

(32) Toan,-T., Teo, B.-K., Ferguson, J.A., Meyer, T.J., Dahl, L.F. *J. Am. Chem. Soc.* **1977**, *99*, 408.

(33) Teo, B.-K. in *EXAFS Spectroscopy: Techniques and Applications*, Teo, B.-

K., Joy, D.C., eds.; Plenum Press, New York; **1981**, pp 13.

(34) (a) Tittsworth, R.C., Hales, B.J. *J. Am. Chem. Soc.* **1993**, *115*, 9763. (b) Hagen, W.R. in *Iron-Sulfur Proteins* Sykes, A.G., Cammack, R., eds.; *Advances in Inorganic Chemistry*; Academic Press, New York; **1992**, *38*, 165. (c) Surerus, K.K., Hendrich, M.P., Christie, P.D., Rottgardt, D., Orme-Johnson, W.H., Münck, E. *J. Am. Chem. Soc.* **1992**, *114*, 8579.

Chapter VIII

Introduction to XMCD:

The Biological Experiment

<u>ABSTRACT</u>

Over the past decade, there has been great progress made in the field of x-ray magnetic circular dichroism (XMCD) at soft x-ray energies (300-1000 eV). Applying this experiment to biological systems requires several problems be overcome. The problems with dilute samples and methods of detection, similar to the problems encountered in biological soft x-ray XAS, are compounded by the presence of a magnetic field. To help maximize the XMCD effect, the ratio of the magnetic field to sample temperature must also be maximized. Early results from this group have demonstrated the effect on a biological sample, but future experiments will utilize ultra-low temperature apparatus and better sources of circular polarization.

Introduction to XMCD

An extension to the current array of XAS experiments is the relatively new technique of X-Ray Magnetic Circular Dichroism (XMCD). By magnetizing a sample in an external field, one can generate a difference in the x-ray absorption by left and right circularly polarized light. First theorized for rare earth materials [1] and later demonstrated for 3d transition metals [2], this technique offers significant advantages over typical XAS. XMCD is sensitive only to magnetic interactions and it can resolve overlapping features allowing identification of individual types of a particular element. Furthermore, since XMCD examines the magnetic, as well as electronic properties of a sample, knowledge of the coupling and exchange properties of mixed-metal and mixed-spin clusters can be gained. This work will deal primarily with the XMCD experimental techniques at soft x-ray energies, examining the L-edges of the first-row transition metals. However, since XMCD is an extension of XAS, experiments at both hard and soft x-ray energies are possible.

Recall the transition for a first-row transition metal L-edge: $2p^6 3d^n$ -> $2p^5 3d^{n+1}$. The selection rules for this regular XAS experiment are $\Delta J = 0, \pm 1$ [3]. In the presence of a magnetic field, the degeneracy of the M_J levels will be lifted and, with left and right circularly polarized light, the selection rule is modified to become: $\Delta J = 0, \pm 1$ and $\Delta M_J = -1$ for right circularly polarized (RCP)

light and ΔM_J=+1 for left circularly polarized (LCP) light [4]. Unfortunately, there is a slight discrepancy in these selection rules. Depending on how the initial and final state transitions are defined [5], the selection rules can also be stated as ΔM_J=+1 for RCP and ΔM_J=-1 for LCP, which are different only in sign. In order to overcome these differences, the general 'rule of thumb' is to subtract the spectra in such a way (LCP-RCP or RCP-LCP) that the majority spin for the element being examined gives rise to a negative L_3 absorption.

The theoretical treatment for XMCD has been incorporated into the same methods used for analysis of standard soft x-ray XAS of first row transition metals described earlier: the initial state is described in spherical symmetry and then the crystal field is incorporated in order to account for the chemical surroundings of the absorbing atom. The primary difference being that the initial and final states need to be described in the presence of a magnetic field and the final spectra are reported as the difference between two polarized spectra.

The XMCD effect is best illustrated with an example. Consider the L_3 absorption of a copper ion in spherical symmetry, an almost full d shell, spin S=1/2 and at an ideal temperature, T=0. In the Cu(II) configuration, the initial state is $2p^6 3d^9$, which has orbital momentum L=2. With coupling, the total momentum J=L+S can take on values of J=3/2 and J=5/2. When a magnetic

field is applied to the system, the degeneracy in the M_J levels will be lifted, and the lowest energy level will be $| J=5/2, M_J=-5/2 >$. In the final state configuration, $2p^5 3d^{10}$, the d-shell is now full, but the hole in the 2p orbital needs to be considered. This final state has $L'=1$ and $S'=1/2$ which couple to form $J'=1/2$ and $J'=3/2$ final states. Examination of the selection rules shows that the only formally allowed transition from the lowest energy state is $\Delta J=-1$, giving a final state of (without considering field effects) $| J'=3/2, M_J'=(3/2,1/2,-1/2,-3/2) >$. In the case of left circularly polarized light, the transition is to $| J'=3/2, M_J'=-3/2 >$. For right circularly polarized light, the final M_J state would be -7/2, which is not possible for the given J' and so there is no absorption for this helicity. If the XMCD spectrum is reported as the difference between left and right polarizations, the resulting L_3 spectrum would be a single negative peak. For an actual system, these results would be modified to account for local symmetry and for temperature >0 K.

Figure 1 illustrates the steps involved in simulating the XMCD for a 2 Fe system composed of antiferromagnetically coupled Fe(II) and Fe(III). This type of system can be seen in bacterial ferredoxins and is indicative of the type of analysis that will occur for complicated mixed-valence clusters. At the top of the figure, the two simulated Fe L-edge spectra for Fe(II) and Fe(III) are shown. It is important to note the peak shift that is present, it is this shift in energy between different oxidation states that can separate overlapping
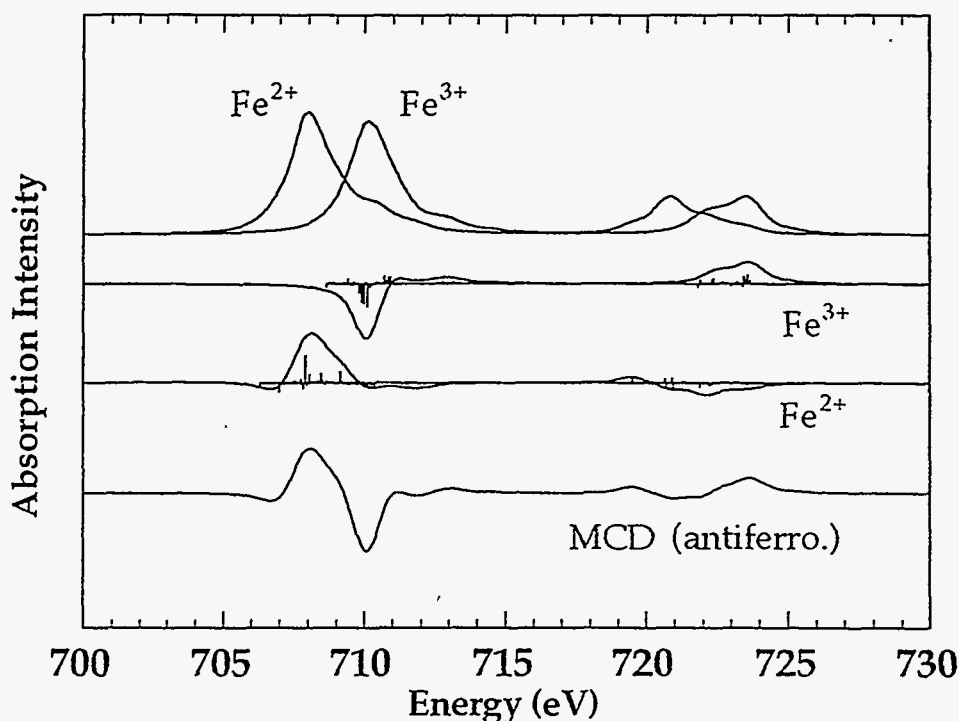
Figure 1: Demonstration of XMCD analysis for a theoretical 2Fe system. *(top)* Simulated Fe L-edge XAS for Fe(II) and Fe(III) atoms. *(middle)* Two plots showing the simulated XMCD for Fe(III) and Fe(II) atoms. *(bottom)* By adding these two contributions together, the resulting XMCD for an antiferromagnetically coupled 2Fe system is generated.

structure and give rise to the features present in an XMCD spectrum. In the middle two plots of Figure 1, the multiplet simulations for the XMCD are shown along with the simulated spectra. Since we are dealing with an antiferromagnetic system in this example, the Fe(III) spectra is inverted[1]. The XMCD spectrum of this coupled system is obtained by adding the two middle

---

[1] As a consequence of the XMCD selection rules used to generate this figure, the XMCD was calculated as LCP-RCP so that the L_3 absorption edge will give a negative XMCD for the majority spin Fe(III). This is consistent with the simple Cu(II) example presented earlier.

spectra to form the bottom plot in Figure 1. Notice the positive and negative features that are introduced and how the presence of the peak shift between the two oxidation states has helped to produce these features.

Magnetization and the Field/Temperature Ratio

In order to observe the XMCD effect, the sample must be magnetized. All magnetic domains must align parallel or antiparallel to the applied magnetic field. In previous XMCD work on non-biological systems, the samples were of a ferromagnetic or ferrimagnetic nature, so sample magnetization was a simple matter using low magnetic fields. Biological metal clusters are generally paramagnetic and so stronger fields and/or lower
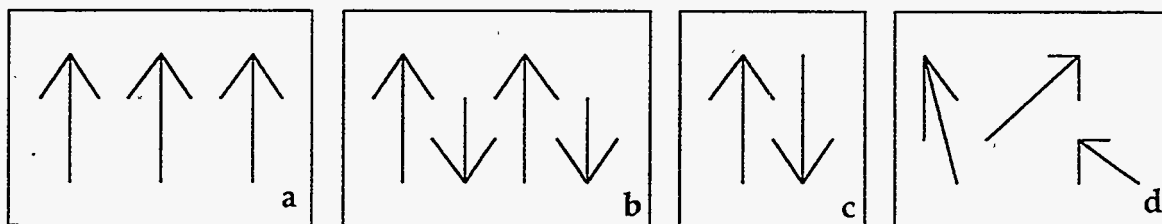

Figure 2: Illustration of the different types of magnetism. (a) ferromagnet, with all domains oriented parallel, (b) ferrimagnet, all domains oriented parallel or antiparallel with a net moment, (c) antiferromagnet, domains oriented as in a ferrimagnet, but with no net moment, (d) paramagnet, domains present, but randomly oriented with no net moment

temperatures must be used to properly magnetize the sample.

To understand the requirement for temperature and magnetic field, a quick look at the theory of paramagnetism is in order. Qualitatively, a paramagnetic system is composed of many domains which can exhibit

magnetic properties, but due to random orientations of these domains, the bulk system does not exhibit magnetic properties. Ferromagnets contain magnetic domains which are oriented so that there is an overall magnetic moment to the system. Ferrimagnets contain domains which are oriented both parallel and antiparallel to the net magnetic moment of the system. If the magnitude of the parallel and antiparallel magnetic domains were equal, a simple antiferromagnet would result (Figure 1).

For an ion in free space, the magnetic moment is given by:

$$\vec{\mu} = -g\beta\vec{J} \qquad (1)$$

where J, the total angular momentum, is the sum of the spin (S) and orbital (L) momentum components, β is the Bohr magneton (defined as $eh/4\pi mc$, sometimes shown as μ_B) and g is the Landé factor, taken as 2.00 for the free electron.

The total magnetization for the system can be written as:

$$\vec{M} = N \cdot \left\langle \vec{\mu} \right\rangle \qquad (2)$$

which is the number density, N, multiplied by the average of the magnetic moments in the sample. This shows how the bulk, macroscopic magnetization is related to the molecular magnetic moments contained in the system.

For a magnetic system, the energy levels are given by:

$$U = -\vec{\mu} \cdot \vec{H} \qquad (3)$$

where H is the applied magnetic field. By substituting in the magnetic moment defined in equation (1) and considering the projection along the magnetic field, the energy levels reduce to:

$$U = m_j g \beta H \qquad (4)$$

where m_j is the azimuthal projection of J (values of $J...-J$). If one considers a single electron without any orbital moment ($J=1/2, m_j=\pm 1/2$), this results in a two level system with a spacing of $2\beta B$ between the two levels (Figure 3).
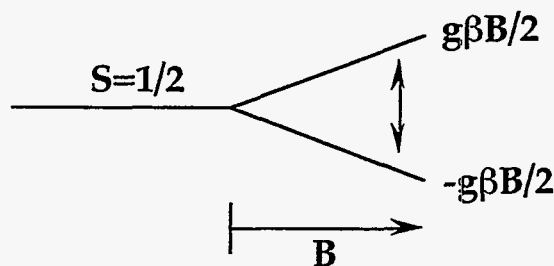
Figure 3: Schematic illustration of the energy levels resulting for an S=1/2 system.

To examine the field and temperature dependence of a paramagnetic system, consider the equilibrium populations of this two level system in a magnetic field. Treating the populations of each level as Boltzmann distributions:

$$\frac{N_+}{N_{tot}} = \frac{\exp\left(\frac{\beta H}{kT}\right)}{\exp\left(\frac{\beta H}{kT}\right) + \exp\left(-\frac{\beta H}{kT}\right)} \qquad (6)$$

$$\frac{N_-}{N_{tot}} = \frac{\exp\left(-\frac{\beta H}{kT}\right)}{\exp\left(\frac{\beta H}{kT}\right) + \exp\left(-\frac{\beta H}{kT}\right)} \qquad (7)$$

$N_\pm$ represents the populations of the two spin states and N_{tot} is the total population of both states. Utilizing the general term for the magnetization, given in equation (2) (where $x=\beta H/kT$, $g=2$, $J=1/2$):

$$\bar{M} = (N_+ - N_-)\beta = N_{tot}\beta\frac{e^x - e^{-x}}{e^x + e^{-x}} = N\beta \cdot \tanh(x) \qquad (8)$$

It is equation (8) that demonstrates the relationship between the total magnetization to the applied magnetic field and the temperature of the
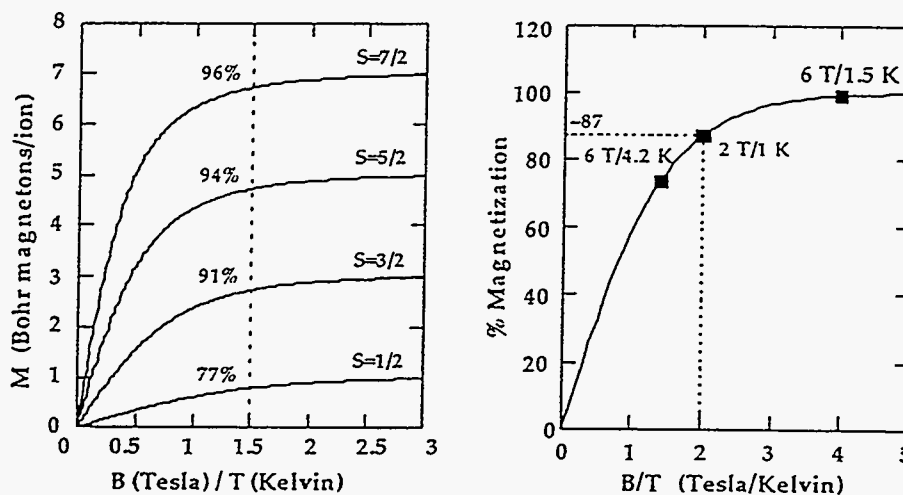
Figure 4: Demonstration of magnetization curves. *(left)* Magnetization curves for several different spin manifolds showing that for higher spin, magnetic saturation is achieved with a lower B/T ratio. The dashed line is for a B/T ratio of 1.5 and the percentage of saturation is shown at the intersection of the corresponding curve. *(right)* The magnetization curve for a S=1/2 system shown with several different points representing various B/T ratios. The dashed line demonstrates the high percentage of magnetization for a B/T=2 ratio.

sample. The XMCD arises from the unequal occupation of these Zeeman split magnetic sublevels which result with high magnetic field and/or low temperature. It is important to note that magnetization is required to maximize the XMCD for a given system, but the absolute magnitude of the effect (LCP-RCP/LCP+RCP) depends on the transitions involved. By measuring the XMCD effect at several different magnetic field values, equation 8 (and its analogs derived for higher spin manifolds) can be used to determine the actual temperature of the surface of the sample, or in the case where the temperature is known, the magnetic ground state can be calculated. It should be noted that for ferromagnetic systems, the inherent orientation of the magnetic domains can be explained by considering an internal magnetic field within the system. This eliminates the need for a strong external field to achieve magnetic saturation.

Figure 4 shows a comparison of the magnetization curves for various spin manifolds. From this illustration it is clear that for higher spin manifolds a smaller B/T ratio is required to achieve magnetic saturation. A dashed line is shown for a B/T ratio of 1.5 and the percentage of magnetization is shown where this line intersects the different magnetization curves. This ratio would result for a 6 Tesla magnetic field and 4 Kelvin temperature, which we have achieved using a superconducting magnet and liquid helium cryostat [6]. Although with a system of this kind one could readily do XMCD experiments on $S=7/2$, $5/2$ and even $3/2$, but for a simple
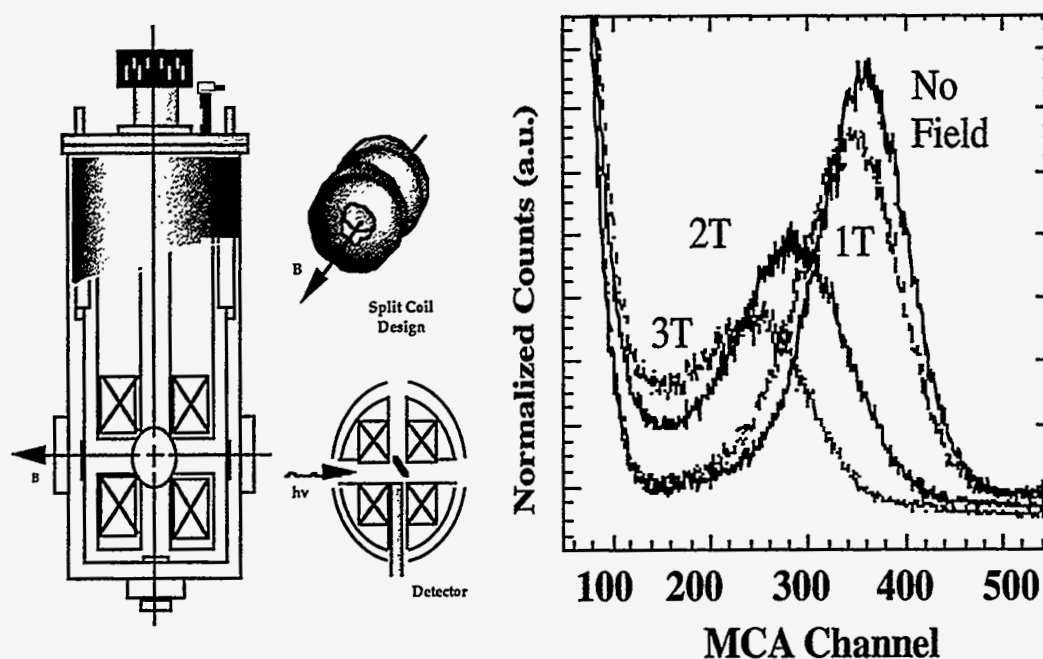
Figure 5: (*left*) schematic views of the split coil magnet system showing the orientation of the field, detector and sample location in relation to the photon beam. (*right*) The effect magnetic field on detector resolution and overall count rate.

S=1/2 system, the percentage of magnetization is significantly reduced. The magnetization curve for a S=1/2 system, described by equation 8, is shown in Figure 4 (right). Shown along the main curve are representative data points for various field/temperature ratios. From this curve, it can be seen that in order to obtain ~87% or greater magnetization, a B/T ratio of >2 must be obtained.

The Biological Experiment

In order to perform the biological XMCD experiment, several issues needed to be addressed in addition to the general considerations for running a soft x-ray experiment such as ultra-high vacuum and low energy x-rays. The

issue of signal detection came up early in our experiments. In general, proteins are very dilute samples with millimolar metal concentrations, whereas the samples used for inorganic XMCD consist of thin films or powders. Just as with the biological soft x-ray XAS experiments described earlier, bulk sensitive detection techniques do not allow for sufficient signal throughput. The resulting method of choice is still fluorescence detection, since it is capable of collecting a small signal with minimal interference from the large, slowly varying absorption background.

The first experiments with XMCD utilized a superconducting magnet capable of reaching fields as high as 6 Tesla and a liquid helium cryostat which could reach temperatures of 1.5 K [6]. The magnet is a split-coil design which allows us to insert our fluorescence detector and sample into the point of maximum field (Figure 5, left). Unfortunately, the Ge solid-state array detectors utilized for these experiments are sensitive to high magnetic fields as illustrated in Figure 5. The figure is a histogram of MCA channels, which relate directly to energy. Examination of Figure 5 shows that with no magnetic field the peak is nicely resolved from the 1/f noise present at the left edge of the graph. As the field is increased, however, the peak starts to reduce in amplitude and becomes less and less resolved from the noise.

In order to correct this problem, the magnetization curve must be revisited. To achieve complete magnetization, and therefore optimize the

XMCD effect, there is the option to increase the magnetic field or lower the temperature. Since the detector demonstrates signifigant error above 2 Tesla, the temperature must be reduced. As shown in Figure 4 (right), in order to achieve >87% magnetization, the temperature of the sample must be reduced below 1 K (B/T=2). This temperature is lower than what can be readily achieved with typical liquid helium techniques, such as our original cryostat used.

Despite these issues, XMCD was demonstrated for the metalloprotein rubredoxin from the thermophilic bacteria *Pyrococcus furiosis*. This was an ideal candidate for the early XMCD studies since it could be prepared in a very concentrated form and the single Fe site allows for simple interpretation. The results of XMCD studies of Fe rubredoxin [7] are shown in Figure 6. Here, the Fe is in the oxidized form, Fe(III), with S=5/2. Recall that with higher spin manifolds, a lower B/T ratio is required for optimum magnetization. So even with relatively warm temperatures and poor thermal shielding, a signifigant XMCD effect can be observed. For this particular case, an XMCD effect of ~30% (lcp-rcp/lcp+rcp) was observed.

Although the effect was quite pronounced for Fe rubredoxin, it was still smaller than the calculated 43% effect, possibly due to the fact that the actual surface temperature was probably warmer than 1.5 K. This temperature deficiency becomes readily apparent when the apparatus is used to measure

the XMCD of a 2Fe sample. The particular ferredoxin used contains a mixed valence, antiferromagnetically coupled Fe pair giving a total S=1/2. Although the individual Fe atoms have higher spin manifolds, the coupling makes the sample more difficult to magnetize.
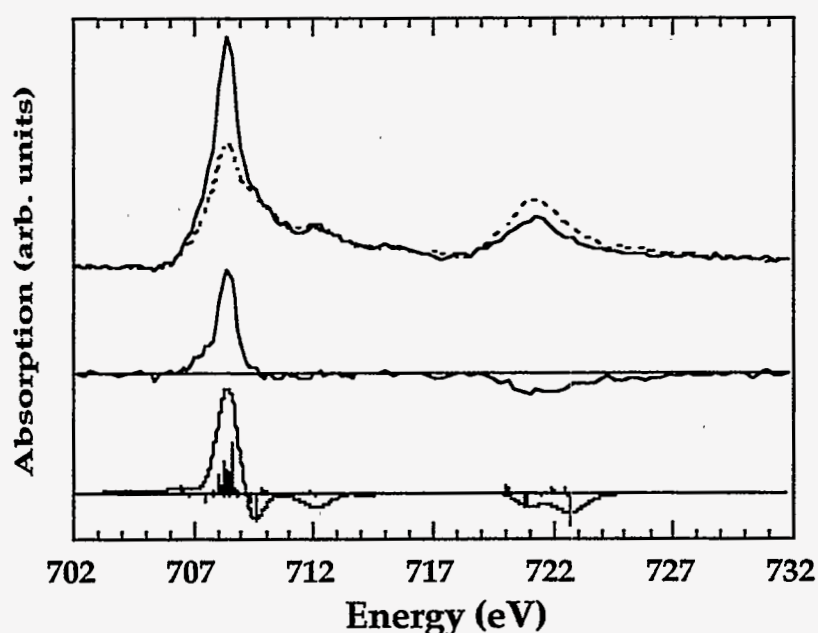
Figure 6: Results of XMCD studies of Fe rubredoxin. *(top)* absorption edges at two different polarizations showing the change in amplitude. *(middle)* the subtracted spectrum showing the magnitude of the effect and any spectral features. *(bottom)* multiplet simulated XMCD showing strong agreement with the experimental results.

The XMCD resulting from an early attemp at a 2Fe ferredoxin is shown in Figure 7. The XMCD results in a small ~12% effect and a single negative going peak in the L_3 edge. Recalling the calculation in Figure 1, it is readily apparent that the 'down-up' pattern calculated for the theoretical 2Fe is not

observed in this case. One probable explanation is that the temperature of the sample was not low enough to adequately magnetize the sample and demonstrate a noticeable XMCD effect. The lack of the 'down-up' features can be attributed to poor signal statistics arising from such a small effect.

The results above make it clear that in order to expand experimental horizons and optimize the XMCD effect, an ultra-low temperature experiment must be developed capable of lowering the sample temperature
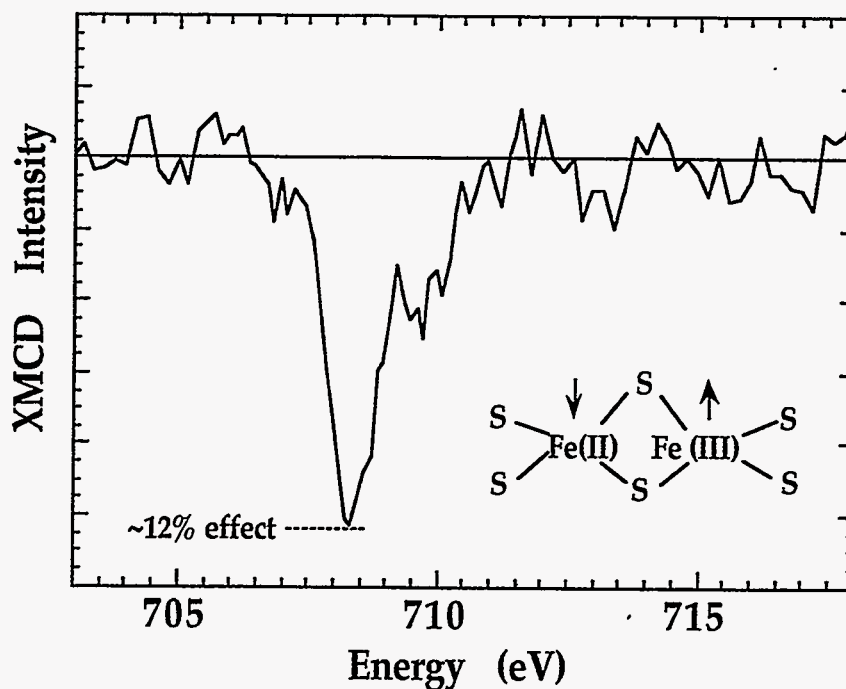

Figure 7: Demonstration of the XMCD observed for an antiferromagnetically coupled 2Fe ferredoxin.

below 1 K. In order to achieve these temperatures, different cryogenic

techniques have to be exploited and the system needs to be designed for optimum thermal conductivity to the sample while maintaining minimal thermal load from other experimental parameters. The paramount result from these experiments should be to demonstrate the actual temperature of the sample surface. Knowledge of this temperature would allow one calculate the amount of magnetization in the sample and can assist a thorough analytical treatment by yielding information about the occupation of the zeeman split sublevels.

By incorporating a ^{3}He cryostat into the 6 Tesla magnet described earlier, we have demonstrated the first ultra low temperature XMCD and these results will be discussed in chapter X. Shielding has been devloped that allows the x-ray beam to reach the sample and fluorescence emission to exit and be collected by a detector. This shielding has been able to successfully shield the sample from the room temperature heat load of the beamline and liquid nitrogen cooled detector face. The description of this system and accompanying shielding will be given in the next chapter.

Sources of Circular Polarization

While we have been developing better techniques of data acquisition, in a parallel fashion, sources of polarized light have been improving dramatically. This combination is making biological XMCD an 'almost routine' experiment. As new insertion devices are commissioned

experimenters are no longer confined to a few bend magnet beamlines for their experiments. As newer generation synchrotron sources offer brighter light, the signal throughput is increased allowing better data to be collected in a shorter time.

The intensity distribution of a bend magnet is such that the dominant intensity is in the plane of the electron storage ring. This distribution can be described over all angles and all frequencies in the following form [8]:

$$\frac{d^2I}{d\omega\, d\Omega} = \frac{e^2\omega^2}{4\pi^2 c}\left|-\hat{\varepsilon}_{\parallel}A_{\parallel}(\omega) + \hat{\varepsilon}_{\perp}A_{\perp}(\omega)\right|^2$$

where the two polarization components are given by the orientation of the electric field vector parallel or perpendicular to the plane of the electron orbit. These amplitudes ($A(\omega)$) can be calculated and the following equation results:

$$\frac{d^2I}{d\omega\, d\Omega} = \frac{e^2\omega^2\rho^2}{3\pi c^3}\left(\frac{1}{\gamma^2}+\psi^2\right)^2\left[K_{2/3}^2(\xi) + \frac{\psi^2}{(\frac{1}{\gamma^2})+\psi^2}K_{1/3}^2(\xi)\right]$$

where the two terms in brackets are still separated by polarization. The angle ψ is the angle of the observation point above the plane of the ring and K_n^2 are the modified Bessel functions, with the argument:

$$\xi = \frac{h\upsilon[1+(\psi\gamma)^2]^{\frac{3}{2}}}{2h\upsilon_c}$$

where hv is the photon energy and hv_c is the critical photon energy which, as described earlier, is a property of the specific photon source. These two polarization amplitudes are plotted in Figure 8. It is apparent from the equations above and Figure 8 that the greatest intensity is in the plane of the ring, and as one moves out of this plane (increasing ψ) the intensity falls off very quickly. At $\psi=0$, the beam is purely linearly polarized, and as ψ increases, the overall intensity falls off and a perpendicular component starts to become signifigant. Bend magnet theory predicts that the parallel and perpendicular components of radiation are phase correlated. By moving above (or below) the plane of the ring, thus introducing more perpendicular character, the light becomes elliptically polarized.
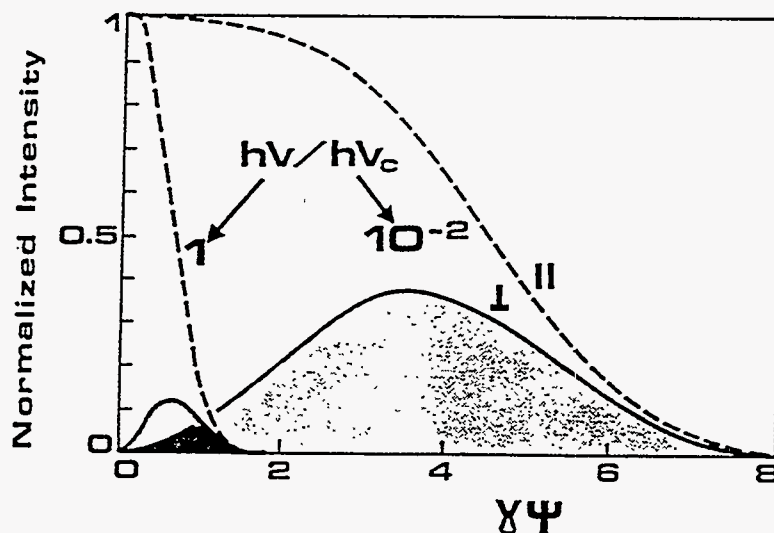

Figure 8: Curves showing the amplitude of parallel and perpendicular polarization as a function of angle above the plane of the ring.

To obtain this circularly polarized light from a bend magnet, one must

optimize the beamline optics to collect light above or below the plane of the electron orbit. This also means that the experiment will suffer a signifigant loss in flux, which can be a critical problem when studying dilute biological samples. To conquer this problem, insertion devices have been developed which have the high brightness and bandwidth characteristics of wigglers and undulators, but also deliver high purity circularly polarized light.

The standard insertion devices mentioned in an earlier chapter will deliver intense light, but it will be polarized in the plane of the ring and optimized in such a way that circular polarization is not possible. However, it is possible to design a multiple-pole device which can generate a periodic magnetic field that causes the electron beam to travel in a helical path through the device. This motion of the beam, in turn, produces high intensity circularly polarized light.

There are several different designs for both wigglers and undulators which can deliver high flux circular light. These designs essentially utilize the same ideas to arrive at the final result and so to keep the discussion relevant to this work, I will focus on the design implemented by Carr and Lidia [9]. This device, known as the elliptically polarizing undulator (EPU), has been commissioned at the Stanford Synchrotron Radiation Laboratory. We have collected XMCD data at this beamline and the results will be described in chapter X.

The EPU consists of four rows of permanent magnets, each row occupying one quadrant around the electron beam path (Figure 9). The two
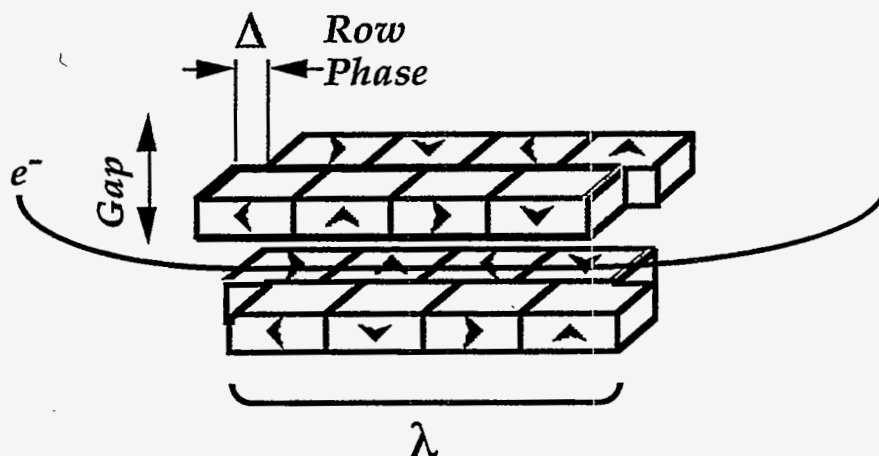

Figure 9: One period of the SSRL EPU showing the orientation of the gap and row phase in relation to the electron beam. The arrows within the blocks indicate the direction of the magnetic field for the permanent magnets.

magnet rows above and below the plane of the electron beam can move relative to each other and the gap between each of these pairs can also be adjusted. As is typical with most undulators, by adjusting the gap between the two pairs of magnet rows, the energy of the beam fundamental can be adjusted. Adjusting the magnet rows in the second and fourth quadrant (in the same direction) the so-called 'row phase' (shown as Δ in Figure 9) is adjusted and the helicity of the electron trajectory, and hence the x-ray beam, is changed. If $\Delta=\lambda/2$ the magnets will align like a typical undulator and the light will. be polarized horizontally, for $\Delta=0$, the light will be polarized vertically and all intermediate values for helicity will be between these two

extremes. For this device, at any given value for the undulator gap, there is a 'row phase' that results in circularly polarized light and the inverse of this phase will result in light circularly polarized in the opposite sense.

Conclusions

To perform XMCD on paramagnetic, biological samples is a non-trivial task. Although experiments have been performed using high fields and relatively high temperatures, it is clearly apparent that ultra-low temperatures must be used and the magnetic field lowered in order to optimize the effect and lessen detector field effects. Alongside this experimental development, new and better sources of circularly polarized light are being brought on line. The combination of these things are making the XMCD experiment much easier. The next two chapters will discuss the operation and set-up of the ^{3}He cryostat/magnet system and the following chapter will demonstrate the device on a protein sample.

References

(1) B.T. Thole, G. Van der Laan and G.A. Sawatzky, *Phys. Rev. Lett.* **1985**, *55*, 2086-2088.

(2) (a) Chen, C.T.; Sette, F.; Ma, Y.; Modesti, S. *Phys. Rev. B* **1990**, *B42*, 7262-7265. (b) Chen, C.T.; Smith, N.V.; Sette, F. *Phys. Rev. B* **1991**, *B43*, 6785-6787. (c) Sette, F.; Chen, C.T.; Ma, Y.; Modesti, S.; Smith, N.V. *AIP Conf. Proc.* **1990**, *215*, 787-795.

(3) (a) DeGroot, F.M.F.; Fuggle, J.; Thole, B.T.; Sawatzky, G.A. *Phys. Rev. B* **1990**, *42*, 5459. (b) van der Laan, G; Kirkwood, I.W. *J. Phys: Condens. Matter*, **1992**, *4*, 4189.

(4) (a) Goedkoop, J.; Ph.D. Thesis, Univerisyt of Nijmegen, **1989**. (b) Schillè, J.-Ph.; Kappler, J.-P.; Sainctavit, Ph.; Cartier dit Moulin, Ch.; Brouder, Ch.; Krill, G. *Phys. Rev. B* **1993**, *48*, 9491.

(5) Thole, B.T.; van der Laan, G.; Sawatzky, G.A. *Phys. Rev. Lett.* **1985**, *55*, 2086.

(6) George, S.J.; VanElp, J.; Chen, J.; Peng, G.; Mitra-Kirtley, S.; Mullins, O.C.; Cramer, S.P. in B. Chance, J. Deisenhofer, S. Ebashi, D.T. Goodhead, J.R. Helliwell, H.E. Huxley, T. Iizuka, J. Kirz, T. Mitsui, E. Rubenstein, N. Sakabe,

T. Sasaki, G. Schmahl, H.B. Stuhrmann, K. Wüthrich and G. Zaccai (eds.), *Synchrotron Radiation in the Biosciences*, Oxford University Press, New York, 1994, p.313 ff.

(7) VanElp, J.; George, S.J.; Chen, J.; Peng, G.; Chen, C.T.; Tjeng, L.H.; Meigs, G.; Lin, H.-J.; Zhou, Z.H.; Adams, M.W.W.; Searle, B.G.; Cramer, S.P. *Proc. Natl. Acad. Sci. USA,* **1993**, *90*, 9664-9667.

(8) For example, see: (a) Jackson, D.S. *Classical Electrodynamics,* John Wiley & Sons, New York, 1975, p 674 ff. (b)Margoritondo, G. *Introduction to Synchrotron Radiation,* Oxford University Press, New York, 1988, p 38 ff.

(9) Lidia, S.; Carr, R.*Nucl. Instr. and Meth.,* **1994**, *A347*, 77-82.

Chapter IX

Operation of the Ultra-Low Temperature

^{3}He Cryostat and 6-Tesla Magnet System

ABSTRACT

This chapter describes the operation of the ^{3}He cryostat and superconducting magnet system. It discusses the function of all the parts of both portions of the system and includes all the relevant data and figures required to maintain ultra-low temperature for an optimal time period.

Part I: Description of the System

Introduction

The superconducting magnet is of the split-coil design. This consists of two wire wound toroidal magnets with the geometry optimized so that the field is uniform at the midpoint between the two toroids. The magnetic field is effectively horizontal between these two toroids (see Figure 1, also Appendix A) and parallel to the beam path. This split between the coils allows insertion of a fluorescence detector, sample changing apparatus and the ^{3}He cryostat into a region of uniform field. The coils are submerged in their own liquid He dewar during operation. Surrounding this dewar, in ultra high vacuum, is a liquid nitrogen cooled shield. This whole apparatus is enclosed in the outer vacuum dewar/chamber (Figure 2, Appendix A).
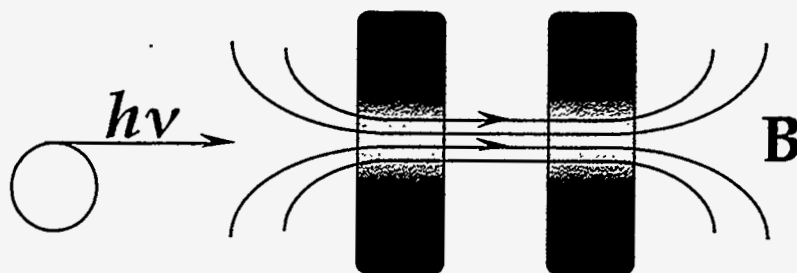

Figure 1: Schematic of the split coil design showing a cross section of the two toroidal magnets with the field and beam path orientation.

The cryostat is of the single-shot, sorption pumped ^{3}He design. The body of the cryostat is insulated from external heat loads by being inserted

down the middle of the magnet liquid helium dewar (shielding at the sample cold finger will be discussed later). Figure 2 shows a schematic of the cryostat and its orientation inside the magnet. The cryostat consists of four isolated spaces: the ^{4}He bath for condensing ^{3}He and thermal insulation; the exchange space which is used to thermally isolate (or thermally short) the ^{4}He bath from the ^{3}He space; the ^{3}He space, containing a charcoal sorption pump; the ^{3}He pot, location of liquified ^{3}He and the coldest point in the system during operation. When the system is at cryogenic temperatures and the exchange space evacuated, the ^{3}He space, ^{4}He bath and ^{3}He pot are all thermally isolated from each other. If the pressure is lowered in the ^{4}He bath, the liquid temperature can drop to below the condensation point of ^{3}He (Appendix B).
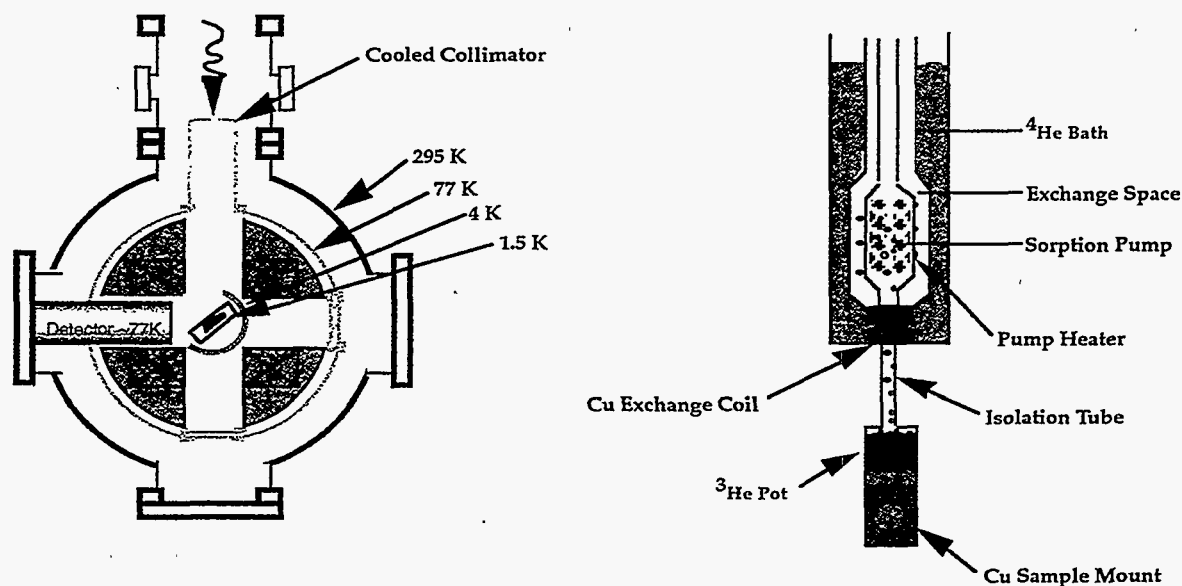

Figure 2: (left) Overhead schematic view of the magnet, detector and shielding layout. The sample is located in the very center, within the 1.5 K shielding. (right) Schematic diagram of the ^{3}He cryostat and sample mount.

If ^{3}He gas is slowly released from the charcoal pump, this gas can contact the Cu exchange coil which is in direct contact with the low temperature ^{4}He bath. This gas then condenses into the ^{3}He pot. Once the condensation is complete, the charcoal pump can be re-cooled thus lowering the pressure above the liquid ^{3}He, and lowering the temperature to ~300 mK.

System Tour

Cryostat (refer to Appendix A): The ^{3}He space is identified by a sealed bellows needle valve and a pressure gauge. Opening this valve will cause the release of the ^{3}He gas and/or introduce contamination into the system. When the system is at room temperature, this gauge should read ~240 psi (there will be some variation with ambient temperature). This pressure will also change during the experiment as the gas is absorbed and condensed. Although the ^{3}He pot is thermally isolated from this space (as described above), it is at the same pressure as this ^{3}He space. This is an important point, as during the experiment there will be times when the pressure in this area will be large enough that the thermal isolation between these two spaces will not be as effective.

There is a second port on the top of the cryostat which has a sealed-bellows needle valve, and also an overpressure release valve. This is the exchange space access. During operation, this space should only contain He gas or be pumped out to vacuum. There is an 8 pin electrical feedthrough on

this port that allows monitoring of the charcoal pump Si diode and pump heater control (see Appendix F).

Finally, there is an ~1.0" port coming out of the side of the cryostat with an overpressure release valve. This is the pumping port for the ^{4}He bath. The fill port is the threaded opening at the very top of the cryostat. There is a 4 pin electrical feedthrough attached to this space which is used to monitor the 14" liquid He level sensor. There is a 19 pin electrical feedthrough just below this 4 pin feedthrough which is used to monitor the experimental thermometry. This does not actually enter the cryostat, but allows for wires to be run on the outside of the cryostat ^{4}He bath, which is in ultra-high vacuum during the experiment.

Traveling down the polished body of the cryostat are several thin manganin wires which are used for the temperature sensors and shield heating (attached to the 19 pin electrical feedthrough just described). There are also several stainless steel baffles along the body which are used to help align the cryostat within the magnet and to help minimize convective conduction. Emerging from the bottom of the cryostat is a fragile, thin-wall stainless steel tube connected to the Cu ^{3}He pot. It is this tube, with its poor thermal conduction and low cross section that provides the thermal isolation between the ^{3}He pot and the rest of the ^{3}He space. Screwed onto the bottom of the ^{3}He pot is a copper sample holder with a four-lead Ge resistance

thermometer inserted.

Around this sample holder is shielding that attaches to the bottom of the ^{4}He bath (Figure 3), on which a 1000 Å Al window is mounted for beam throughput, and a heater installed to keep water from condensing on the window during cooldown. This shielding is in two parts: the portion that has the heater wrapped does not need to be removed from the ^{4}He bath, while the
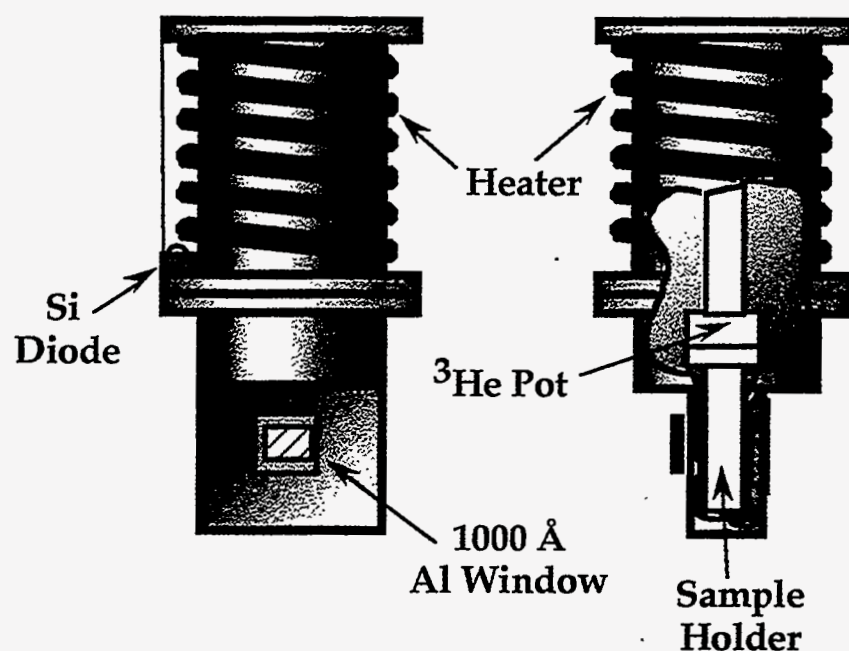
Figure 3: The 1.5 K shielding attached to the bottom of the 4He bath. The heater wire and Si diode are shown on the top portion and a cross section (right) shows the position of the 3He pot and Cu sample holder.

bottom portion will need to be removed to allow access to the Cu cold finger. During operation, this shielding is connected to the ^{4}He bath which will be at ~1.5 K.

Connected to the bottom of the magnet liquid helium dewar is a

movable shield. This shield can be moved up or down by use of a vaccum feedthrough on the bottom of the vaccuum chamber. The semi-circular shape of the shield (see Figure 2) allows the beam to enter and the detector to move close to the Al window unobstructed. When this shield is lowered, there is access to the 1.5 K shield and all the viewports will have optical access. During ultra-low temperature operation, this shield can be moved into the up and locked position. This connects the shield to the 4 K magnet reservoir and shields the 1.5 K shield from heat loads generated by the sample changing port and 77 K viewport windows.

Magnet (refer to Appendix A): At the very top of the magnet is the 4.625" conflat flange port where the cryostat is inserted. The black vacuum fitting is a rotation stage that allows for rotation of the cryostat/sample during the experiment under vacuum conditions. The bolts must not be overtightened as they can put enough pressure on the rotation flange that the cryostat can no longer rotate. There is also a 19 pin electrical feedthrough on the neck of the dewar, just below the cryostat flange. This feedthrough is for the magnet liquid He level sensors (there are two, in case one fails), persistent switch heating and voltage sensing. Coming out of the neck of the dewar is the magnet quench valve. This is a spring loaded o-ring seal that will open in the case of overpressurization within the sealed, magnet liquid helium dewar.

On the top flange of the magnet are the two threaded ports for liquid

helium filling (and venting). There is also a Swagelock assembly that holds the two high current leads for the magnet. This lead assembly has a pressure relief valve above the two high current lugs. It is very important that this not be blocked, since the leads for this system are cooled by the vapor from the liquid helium reservoir flowing through this lead assembly. Heat build-up at these leads can lead to excessive boil-off from the liquid helium reservoir and a local hot spot at the base of these leads can lead to a magnet quench.

Near the outside of this top flange is an overpressure foil in the case of overpressure in the vacuum space. If the vacuum space should overpressurize, this foil will tear on the sharp jaws and pressure will release (be careful around this fitting, it can be punctured very easily). If vacuum should be lost during operation a serious safety hazard will result and the system may be damaged as all the suddenly heated cryogenic reservoirs violently boil-off. A common practice has been to place a thin strip of tape over the top of this fitting. It should be tight enough to be protective, yet loose enough to allow pressure to escape in the event of a vacuum failure.

The second port near the outside of this top magnet flange has a Convectron gauge attached. This gauge is only useful at high pressures ($\sim 10^{-3}$ - 999 torr), but it can be used to monitor the initial magnet pumpdown and a slow bleed up to atmospheric pressure (~ 760 torr).

The top flange is attached to the rest of the dewar by a bolt pattern at the outside of the flange. In order to access the inner radiation shields and liquid helium dewar, this indium seal must be opened first and procedures for this will be discussed later. About halfway down the outer jacket is a welded lifting flange that is used for mounting the magnet into its table. It can also be used to stabilize the system during shipping.

At the bottom of the outer dewar are the conflat access ports to the magnet bore and split. Three of these are 4.625″ flanges, while the fourth is a 6.0″ conflat for the detector. There is also a small viewport window located just above one of the 4.625″ conflats and at a 30° angle to allow optical access to the bore of the magnet. At the very bottom of the dewar is another 4.625″ flange which goes through the center of the split between the magnets.

Part II: Operation of the Cryostat and Magnet System

Initial Set-Up

If the system is being unpacked, the shipping spacers must be removed before operation can begin. To do this, an overhead crane or winch will be required, and all 'UHV clean' procedures should be observed. First, open the indium wire seal at the top of the magnet (Figure 4) and remove the whole assembly from the outer vacuum jacket. At the bottom of the liquid nitrogen shield will be the first set of shipping spacers to be removed. Then, remove the liquid nitrogen shield at the point shown in Figure 4. This will expose the sealed liquid helium dewar that contains the magnet and the movable 4 K shield. At the bottom of this dewar are the inner shipping spacers that need to be removed.

This is the proper time to clean any components that will later be sealed in vacuum. This is also the time to confirm that the liquid nitrogen shielding is all in place. Figure 2 shows the current arrangement used on the liquid nitrogen shield. The port opposite the beam path should have a quartz window or blank disk in place. The beam port should have a liquid nitrogen cooled collimator attached (note: this may need to be placed loosely and then firmly attached after the vacuum jacket is sealed). The detector port should be free of obstruction, although some Al tape shielding can be used to minimize the size of the shield opening. The sample loading port can be sealed or be

left open. All of these items are attached to the shield with compression flanges. All surfaces should be clean and some indium wire placed between the mating surfaces to assure good thermal contact.
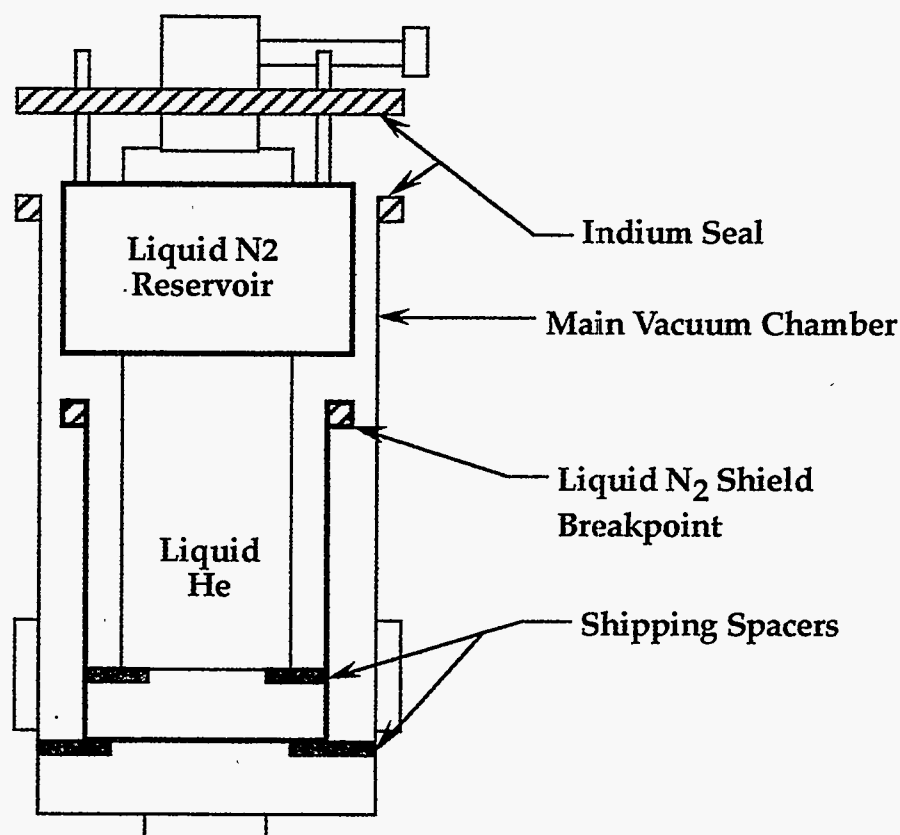
Figure 4: Schematic showing the location of the shipping spacers inside the vacuum chamber and flanges that need to be opened for access to the spacers.

To obtain an ultra-high vacuum compatible seal for the outer vacuum jacket an indium wire seal must be used. To prepare for this seal both mating surfaces and the new indium wire (0.040″ dia) must be thoroughly cleaned and old wire removed. DO NOT use metal instruments to do this, as they may gouge the machined surface and inhibit the seal. Try using a wooden applicator stick. Once the old sealing wire, dirt, dust and grease has been

removed, the new indium wire can be carefully placed into the groove. Be very careful, as indium wire is soft and easily kinks. Nicks or thin spots can result in seal failure. It is very important that the point where the two wire ends come together is made in such a way that when the flanges are bolted together, the seal will remain strong. Once the wire is in place, the inner cryogenic dewars can be slowly lowered into the vacuum can. The two flanges must come together slowly and evenly. This must be done carefully since the seal CANNOT be redone once the flanges come together. When the flanges are together, the bolts can be installed finger tight. The bolts MUST then be tightened EVENLY around the entire flange. The following tips should help to obtain a good seal:

· A recommended bolt tightening pattern is to tighten bolts in pairs on opposite diameters.

· Do not tighten all at once, go around the flange several times.

· Cut wire with a sharp razor, be careful not to pull the wire as this leads to thin spots.

· Do not rotate the flange to align the screw holes when in contact with the wire - This can tear the wire and the seal will fail.

· Since this flange will experience many different temperature variations during operation, lock washers should be used to keep the seal tight during metal expansion and contraction.

· Indium wire 'flows', so the seal should be left for approximately

half an hour and then the bolts checked again for tightness.

With the main flange sealed, all other external connections to the chamber can be made (i.e. gate valves, detector, feedthrough connection to movable 4 K shield, etc.). The cryostat can now be prepared for insertion into the magnet bore. All appropriate shielding for the cryostat must be in place, including the shield heater and Si diode. To assure good thermal contact to the sample, all copper surfaces should be cleaned with acid to remove oxide layers. This is especially critical for the threads that the sample holder will be screwed into. A small amount of conductive apiezon or vacuum grease can also be applied to these threads. With the sample holder clean, the lower portion of the radiation shield can be installed. A small amount of conductive apiezon or vacuum grease should be applied to this mating surface to assure good contact. At this point, the temperature sensors should be briefly connected and checked for accuracy (Si diodes ~ room temp, Ge sensor ~1-2 Ω, see Appendix C). Great care must be exercised not to damage the thin wires outside the cryostat as they are very fragile.

When ready to install the cryostat, the 1000 Å Al window can be installed. This must be done with extreme care, these windows are very fragile. Rough handling and strong air currents can shatter the window. If possible, a small amount of conductive apiezon or vacuum grease should be placed behind the frame and on the compression ring to assure adequate

thermal contact with the radiation shield. Once the window is installed, any beam phosphor should be placed on the outer radiation shield to allow for later beam alignment. With this done, the cryostat can be carefully installed into the top of the magnet. Be careful when tightening the bolts that hold the cryostat to the rotation flange. If overtightened, the flange will not rotate.

With the vacuum can sealed, a pump can be attached and the system slowly evacuated. Remember, the 1000 Å Al window must be treated with care. Pumping too quick will cause a current of air to rupture the window. It is recommended that the pumping speed, as monitored with the Convectron gauge, be no more than 1 torr/sec. When the vacuum is in the high 10^{-2} range, full pumping speed can be used and the window should be safe. When the pressure is adequate, a thorough He leak check should be performed, paying close attention to the indium seal at the top of the magnet. Hopefully, the pressure in the magnet will drop down in the mid-10^{-5} torr range after several hours.

Once the pressure has dropped into the 10^{-5} range and the system leak checked, the cryogenic spaces can be prepared. When cooling begins, any water and/or contaminants (even air, in the case of liquid helium) inside these spaces will freeze and can inhibit the proper operation of the system. It is very important that the vacuum chamber be evacuated when these procedures begin. If a cryogenic space is evacuated (i.e. the magnet liquid

helium reservoir) while the vacuum chamber is pressurized, the dewar can collapse.

Make sure that the gauge on top of the ^{3}He space still reads ~240 psi (with some variation depending on ambient temperature). The exchange space should be thoroughly evacuated (preferably with a turbo pump) and then purged with helium gas. This procedure should be repeated at least three times and then the space filled with an overpressure of helium gas. This same procedure should be used for the main cryostat reservoir (^{4}He bath). The magnet helium reservoir should be pumped to below 10 torr and then purged with helium gas. This procedure should also be repeated at least three times and then the magnet sealed.

Pre-Cooling the System

In order to conserve liquid helium and more efficiently cool the system, liquid nitrogen is used to fill all the cryogenic spaces first. This liquid will then be removed, after the initial cooling, and liquid helium put into the appropriate reservoirs. Care must be taken to remove ALL the liquid nitrogen, otherwise it will freeze when liquid helium is introduced.

The order in which liquid nitrogen is introduced can also be important. In this case, the cryostat will be cooled last in an attempt to condense all water remaining in the vacuum space on the magnet and nitrogen shield, and not

on the thin Al window. Since soft x-rays have very short penetration depths, it only takes ~1 micron of water to completely absorb the x-ray beam.

WHENEVER HANDLING CRYOGENIC MATERIALS - WEAR SAFETY GOGGLES AND GLOVES!

With all temperature sensors and heaters wired per the diagram in Appendix D, set the heater level for the cryostat radiation shield to ~280 K and leave it on. This will keep the window warmer than the freezing point of water during pre-cooling. Now, slowly introduce liquid nitrogen into the magnet liquid nitrogen reservoir. Liquid nitrogen can be filled quickly, but large amounts of splattering should be avoided. Once this reservoir is full, the openings can be sealed with rubber stoppers or just aluminum foil. A cover should be used, as this will reduce the rate of consumption and stoppers will minimize the amount of condensation that occurs around the fill and vent ports.

The magnet reservoir should be filled next. This will require ~60 liters of liquid nitrogen. Check again to make sure that all water and air are removed from this space, and purge with helium gas. The nitrogen should fill through one of the liquid helium ports and the other port should be fully open for vapor venting. It is a good idea to stick a piece of copper tube into the vent opening to direct the flow of gas away from the rotation flange. It is

also advisable to use a small piece of wood or soft material to hold the quench release valve open. The magnet has a large thermal mass and filling this space will take some time and generate a large amount of boil-off vapor. In order to monitor this fill (as well as the liquid helium filling) the resistance across the magnet leads (on the top flange of the magnet) can be monitored, using the table below:

Magnet Resistances at Specified Temperatures:

Room Temp.	21-22 Ω
Liquid Nitrogen	16-17 Ω
(<~10 K)	0 Ω

Once the magnet reservoir is completely full (this may not be the same time that the magnet resistance goes to ~16-17 Ω) the liquid nitrogen fill can be removed from the magnet. All the openings should be sealed and the quench valve closed. The system should now be left for several hours. This allows thermal equilibrium to be reached and for all the water to be plated out of the system. The quench relief and vapor cooled leads will allow any pressure from boil-off to be released.

After several hours of cooling the magnet with liquid nitrogen, the cryostat can now be pre-cooled. The radiation shield heating must be turned off at this time. It is critical that all water be removed from the system here

also. The cryostat has much less volume than the magnet so cleanliness is even more important. The cryostat should be filled to the top with liquid nitrogen and then sealed. Make sure that the release valve on the side of the pump-out port is not blocked by ice. If it is, use a heat gun to defrost it. The temperature of the radiation shield, sample cold finger and charcoal pump should be monitored throughout this process. Since helium gas is in the exchange space, the charcoal pump should read 77 K almost immediately while the radiation shield will cool more slowly. The cold finger resistance will change very slowly. It will take ~12 hours for the cold finger to cool to ~110 K or less. The vacuum should have improved dramatically by this time, to the low 10^{-7} torr or less. As the ^{3}He space cools, the pressure gauge should also drop down to ~70 psi.

Once the system is cooled to liquid nitrogen temperature, the liquid can be removed. If not already installed, the magnet initial-fill tube should now be installed. This is a short tube extension to the helium transfer lines, it screws into a tube on top of the magnet that goes to the bottom of the magnet dewar (Appendix A). The vapor cooled lead relief valve should be sealed to allow for dewar pressurization. If pressure (from dry N_2 or He gas) is applied to the other helium fill port, liquid nitrogen will be pushed out of the initial-fill tube. CAUTION liquid nitrogen will come out quickly. Be ready to collect this or transfer it into the liquid nitrogen reservoir. Once all the liquid is removed, the reservoir should be pumped and flushed as before. The

pressure should be brought down below 10 torr and then the reservoir purged with He gas. If pumping stalls at ~95 torr, this implies that all the liquid has not been removed. This pump and flush procedure should again be performed at least three times and then the dewar should be sealed under vacuum. This same procedure should be used to clear the liquid nitrogen out of the cryostat and purge the ^{4}He bath.

Liquid Helium Transfer

With the magnet and cryostat pre-cooled to liquid nitrogen temperatures and evacuated, liquid helium can now be introduced. The magnet should be filled first. Since this will be the first liquid helium fill, the initial fill tube should be in place and the shorter 90° transfer line used. Just as with the liquid nitrogen filling, a piece of copper tubing should be placed at the vent port to direct the cold vapor from freezing the rotation flange. The transfer line should be lowered into the liquid helium dewar slowly, making sure the dewar does not reach a dangerous overpressure. Once a very cold spray is observed at the other end of the transfer line (evidenced by the visible presence of 'fog') the transfer lines can be coupled together.

Liquid helium should be filled slowly to minimize consumption. If the space is filled too quickly, there will be tremendous boil-off after filling as the system comes to thermal equilibrium. By slow filling, the boil-off vapor cools the rest of the dewar and once condensation occurs, the fill will progress

rapidly. Monitor the liquid level by using the 22" level sensor readout on the power controller. Also, the resistance between the leads can be monitored using the table previously given. It can take almost 20 minutes before condensation starts to occur (or resistance goes to zero). Some important helium levels are shown in the table below:

Representative liquid He levels (from 22" sensor)

Sensor Reading	Level
0.0" - 0.5"	Condensation Starting
0.5 "	Bottom of Magnet
9.5"	Top of Magnet Coil
11.3"	Top of Persistent Switch
12.5"	*Minimum Operating Level*
22"	Maximum Level

Once the magnet is filled to the maximum 22" level, vent the liquid helium dewar and remove the transfer lines. The initial fill tube should also be removed at this time (it will no longer be needed if the magnet level is kept above 11"). Both fill and vent ports should be sealed with Goddard fittings and make sure that all relief valves are free from ice blockage.

The chamber vacuum should have improved into the 10^{-9} torr scale by this time. There will be a sharp pressure drop when the helium first condenses and then the pressure will go down slowly. After 24 hours, the magnet should be $<5 \times 10^{-9}$ torr or better. The surfaces cooled to liquid helium

temperature are very large, the magnet will act as a very powerful cryopump. The turbo pump being used to pump out the main vacuum will probably need to be removed (Experience has shown that this effect starts to become noticeable around 3×10^{-8} torr, but this value will vary depending on the pump being used). This should be checked as soon as possible to avoid pulling any oil or air into the system.

A similar procedure should be used to fill the cryostat ^{4}He bath. There may be some difficulty in getting the long 90° transfer line down the cryostat. Gentle rotation with soft pushing will bring the transfer line to the bottom of the cryostat. The process of filling the cryostat can now begin and the temperature of the Si diodes should show the temperature dropping rapidly before the 14″ level meter shows any condensation. Once the cryostat is filled, the transfer line can remain, (it is too difficult to continuously remove and re-insert) but should be sealed as well as the pump-out port. Make sure the overpressure release valve is clear of any ice blockage.

Because the Cu cold finger/^{3}He pot is thermally isolated from the rest of the system it can take a significant amount of time to cool. The charcoal sorption pump has its highest pumping speed at ~4 K and will expel ^{3}He gas at ~40 K. With liquid helium in the cryostat, the charcoal will pump out all ^{3}He gas and effectively isolate the ^{3}He pot. In order to allow some type of thermal exchange between the ^{3}He pot and the copper coil, the charcoal must

be warmed up. The charcoal will expel ^{3}He gas which will serve as a conduction medium between the copper coil and the ^{3}He pot (Figure 2). To do this, the exchange space must be thoroughly evacuated first (preferably with a turbo pump). When the exchange space is at high vacuum, thus isolating the ^{3}He charcoal pump from the ^{4}He bath, the charcoal pump should be heated to 45 K. This will allow the maximum amount of ^{3}He gas to be released for thermal conduction. It can take several hours for the copper cold finger to reach cryogenic temperature (~4-6 K). During this time, it may also be necessary to top up the level of liquid helium in the cryostat. Experience has found that if the exchange space is properly evacuated, the charcoal pump will remain at ~20 K without any heating. If nothing is going to be done with the magnet during this time, the level sensor should be turned off. The level sensor uses a current to measure resistance, so a small heat load is introduced when the sensors are being read.

Magnet Tests

With the system stabilized at liquid helium temperatures, tests of magnet operation can be run. Make sure that all relief valves are free and not frozen in place. Also, strong magnetic fields will be generated, so metal objects should be removed from the area or firmly secured. Confirm that all wiring is in accordance with Appendix D. The power controller should always be turned on first, then the magnet power supply (when de-activating, turn off the power supply first) to avoid power spikes.

Using the power controller, activate the persistent switch heater. When the persistent switch is activated, a light on the front of the power supply will illuminate. This magnet system uses voltage sensing, this means that the power controller monitors the voltage and polarity at the bottom of the vapor cooled leads. It is VERY IMPORTANT that these leads be connected properly, if reversed, they will damage the power supply. When charging the magnet, a positive voltage should ramp positive current, if this is not the case IMMEDIATELY turn off the power supply to stop the charging procedure. The system is set up to charge at maximum of 3.0 V, for higher currents (>35 A), it is recommended that 2.5 V be the maximum. DO NOT EXCEED THE MAXIMUM CURRENT RATING OF 87 AMPS. The magnet produces a maximum field of 6 Tesla, a good rule of thumb is '15 amps per Tesla'.

Check magnet operation by ramping to various fields/currents at both positive and negative polarities. Try maintaining a high current for several minutes at both polarities. To check the superconducting integrity, ramp the magnet to a fixed current/field and then deactivate the persistent switch. This puts the superconducting magnet into persistent mode, the power supply is no longer supplying the coil. After 30 minutes, adjust the power controller back to the original current (if it was changed, the persistent switch will not activate if there is a large difference in the magnet current and

supplied current). Turn the persistent switch back on. If the switch activates and there is not an appreciable change in the supplied current, the magnet is operating properly in persistent mode.

Operation of the Cryostat

Once the copper cold finger has reached liquid helium temperatures, the operation of the ^{3}He cryostat can begin. It is best to start the process with the cryostat filled with liquid helium. The heater should be turned off (if on) and the exchange space should remain at high vacuum. The Ge sensor is calibrated from 6 K to 0.3 K, so at these temperatures the temperature controller can read either Kelvin degrees or sensor resistance.

In order to minimize thermal loads on the cold finger, the liquid nitrogen cooled detector should be moved into the magnet, at least within a few inches of the 1.5 K shield. Also, the movable 4 K shield attached to the bottom of the magnet should be moved into the closed/locked position.

A mechanical pump can now be attached to the cryostat pumpout port and the temperature of liquid helium slowly reduced to ~1.5 K (~3.6 torr). It is very informative to have some type of pressure gauge attached in line, since the charcoal pump thermometry is thermally isolated when the exchange space is evacuated. Appendix E is a plot of the relationship between pressure and temperature. It will take several minutes to reach this low pressure, and

slow pumping will consume less liquid helium. During this process, the charcoal can be slowly warmed to 25 K. The Ge sensor should show a corresponding temperature drop as ^{3}He gas starts to condense at the copper exchange coil (Figure 2).

The gauge at the top of the ^{3}He space should show a slight vacuum as the heater is first turned on and the temperature of the ^{4}He bath is not yet <3.4 K. Around 3 K, the gauge will start to read high vacuum (bottom of gauge), the condensation of ^{3}He has begun. After 15-30 minutes, the temperature of the cold finger should be ~2 K and the ^{3}He pressure gauge should still be reading high vacuum. At this point, the charcoal can be slowly heated to 45 K. It is advisable to use low heater power settings and adjust the temperature in steps (i.e. 25K->30K->35K->40K->45K). There may be an increase in the cold finger temperature as the heater temperature is raised. This is due to the sudden release of warm ^{3}He gas not condensing and heating up the ^{3}He pot. Thermal equilibrium should re-establish quickly and the temperature should start dropping again after a minute or so.

The condensation should be allowed to proceed for at least 45 minutes. During this time, the sample cold finger can go as low as 1.5 K. A good indicator of when all the ^{3}He has condensed is that the temperature will tend to level out and show small oscillations.

When all of the ^{3}He has condensed, the charcoal heater should be turned off. A very small amount of He gas (i.e. a quick open/close of the needle valve) should then be added to the exchange space. The charcoal pump will then quickly cool to thermal equilibrium with the 1.5 K ^{3}He bath. This will also result in a large loss of liquid helium in the cryostat. The temperature of the sample cold finger should start to rapidly decrease. As the charcoal cools to 4 K and the charcoal pumping speed increases, the temperature will drop faster. Soon, the ultimate base temperature of ~300-400 mK will be reached.

Once this condensation has begun and the charcoal is pumping on liquid ^{3}He, the cryostat pump can be deactivated. This might be necessary, since the cryostat may need to be refilled after the condensation process. Prior experiments have found, however, that lower temperatures are achieved when the ^{4}He bath is kept under low pressure.

Some important Tips:

· Keep the exchange space very clean. Contaminants in this
space lead to large liquid helium consumption and poor
condensation.

· If you need to refill during the condensation, bring the pressure
in the cryostat up slowly with He gas. Then fill quickly and
pump back down. The temperature will increase during the fill

if the charcoal pump warms up, but it should recover as the charcoal cools back down.

· Pumps attached to the system should have their vibrations damped. Excess vibration will add heat load to the cold finger.

· The times given above are very approximate, and vary each time a condensation is performed. It is better to monitor the temperature and pressure without considering the time.

· Although the cold finger should go down to 1.5 K in theory, it rarely does this in practice. Low temperatures of 1.9-2.2 K are more typical. When a temperature in this range is reached for several minutes, the charcoal pump should be heated up to 45 K.

· Finally, operation of the charcoal pump during condensation tends to require a certain amount of 'feel', so experimenters should practice with the system prior to installation at a beamline.

During the conduction of the experiment, it is important that all cryogenic levels are maintained, especially in the magnet dewar. NEVER go below 12.5″ in the magnet, the magnet can quench. The topping up process of the magnet and cryostat is essentially the same as the fill process. Since there is liquid helium above the magnet, it is more efficient to fill from the top of the dewar, so the initial fill tube is not needed. It is also advisable to refill the magnet from the opposite side of the initial fill. Since the ^{3}He pot is

thermally isolated from the rest of the cryostat, after condensation, the level of the ^{4}He bath can drop to zero% for a short period before any effect is observed on the cold finger.

Appendix A: Magnet Schematic
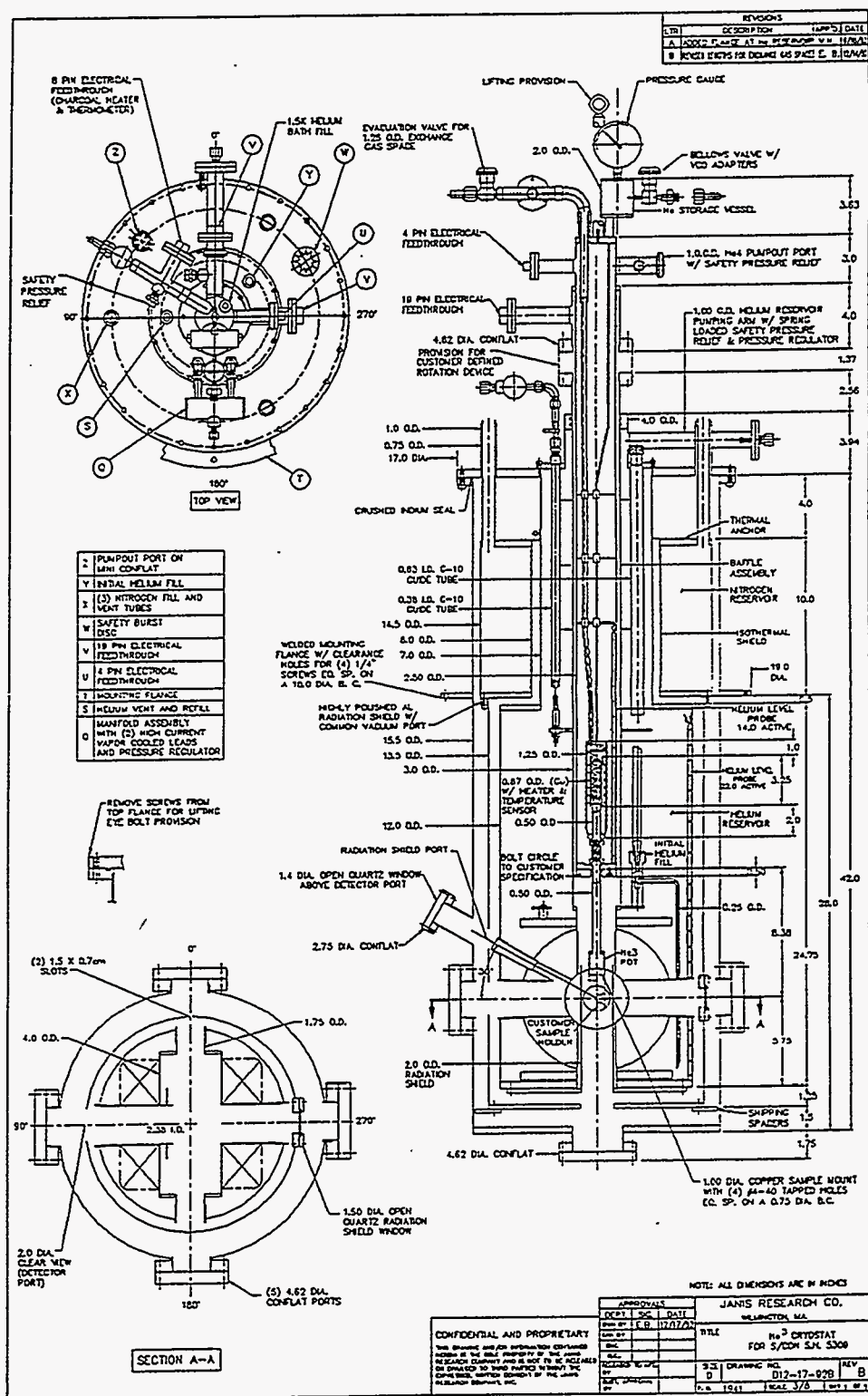
Appendix B: Cryogenic Information

Nitrogen
　　Boiling Point (at 1 atm)- 77 K
　　Heat of Vaporiztion (J/cm^3) - 160

Helium-4
　　Boiling Point (at 1 atm) - 4.2 K
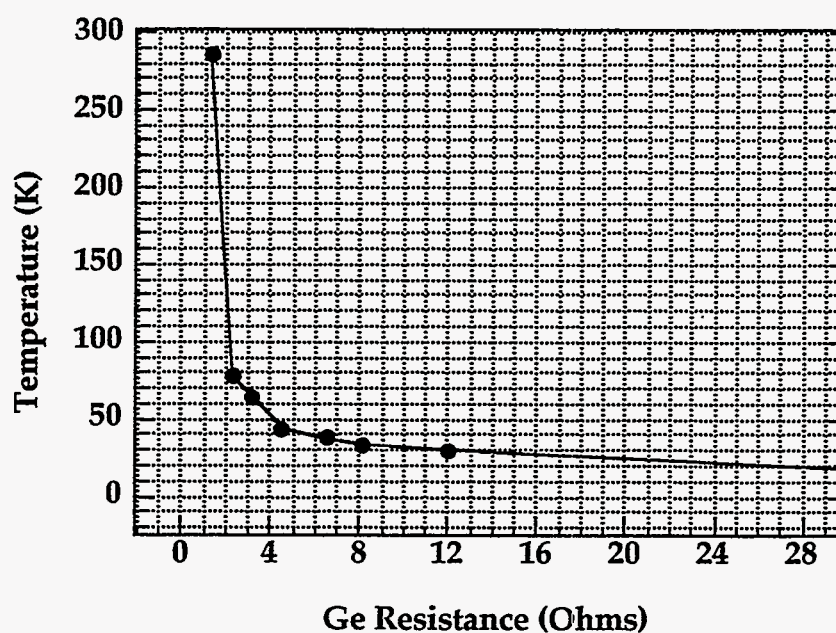　　**Heat of Vaporization (J/cm^3) - 2.6**

Helium-3
　　Boiling Point (at 1 atm) - 3.4 K
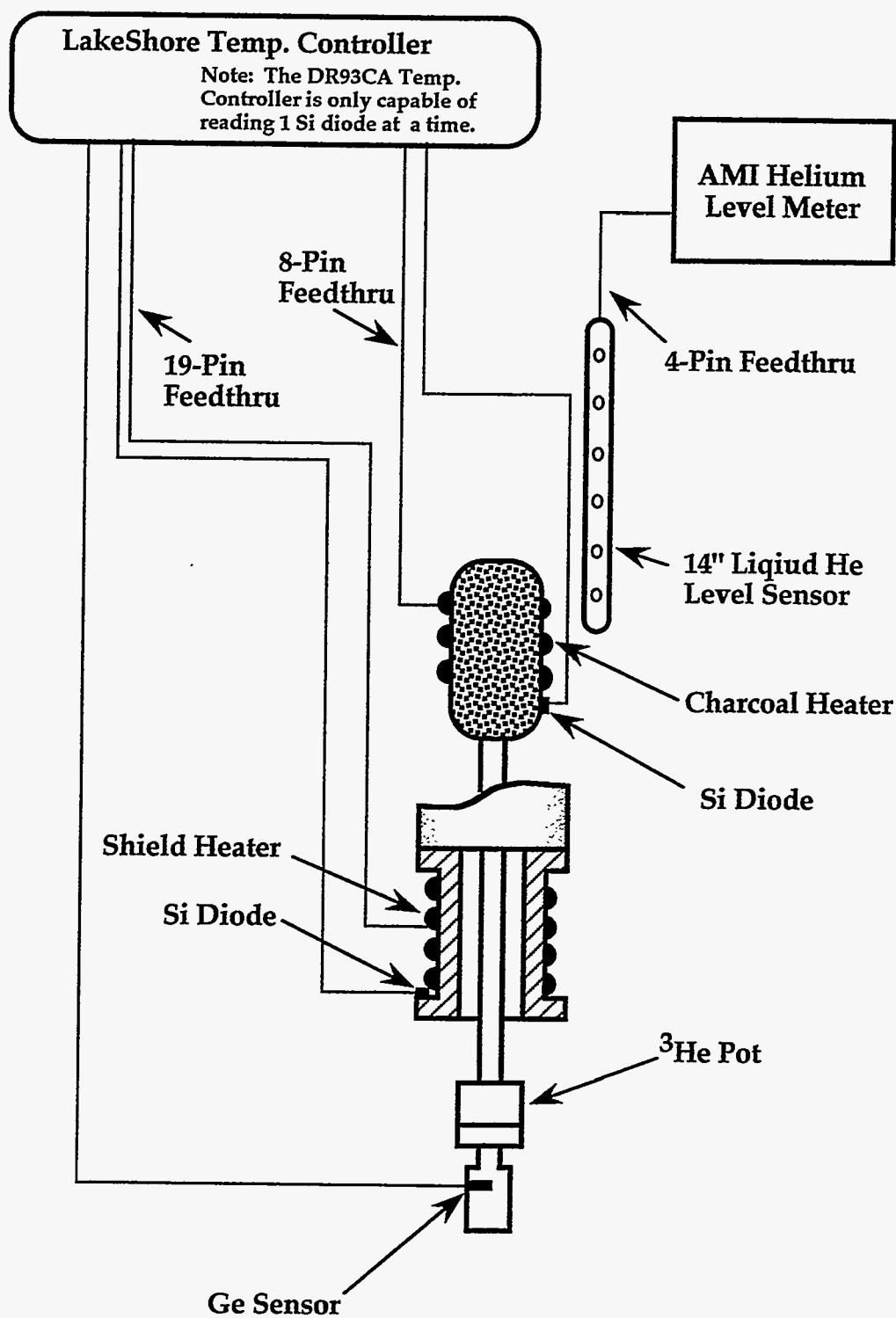　　**Heat of Vaporization (J/cm^3) - 0.48**

Appendix C: Ge Resistance Values

- **Using LakeShore Ge sensor #26404.**
- **For Temps <8 K, see sensor calibration chart.**
- **These values are from experiment, and should only be used for rough approximations**
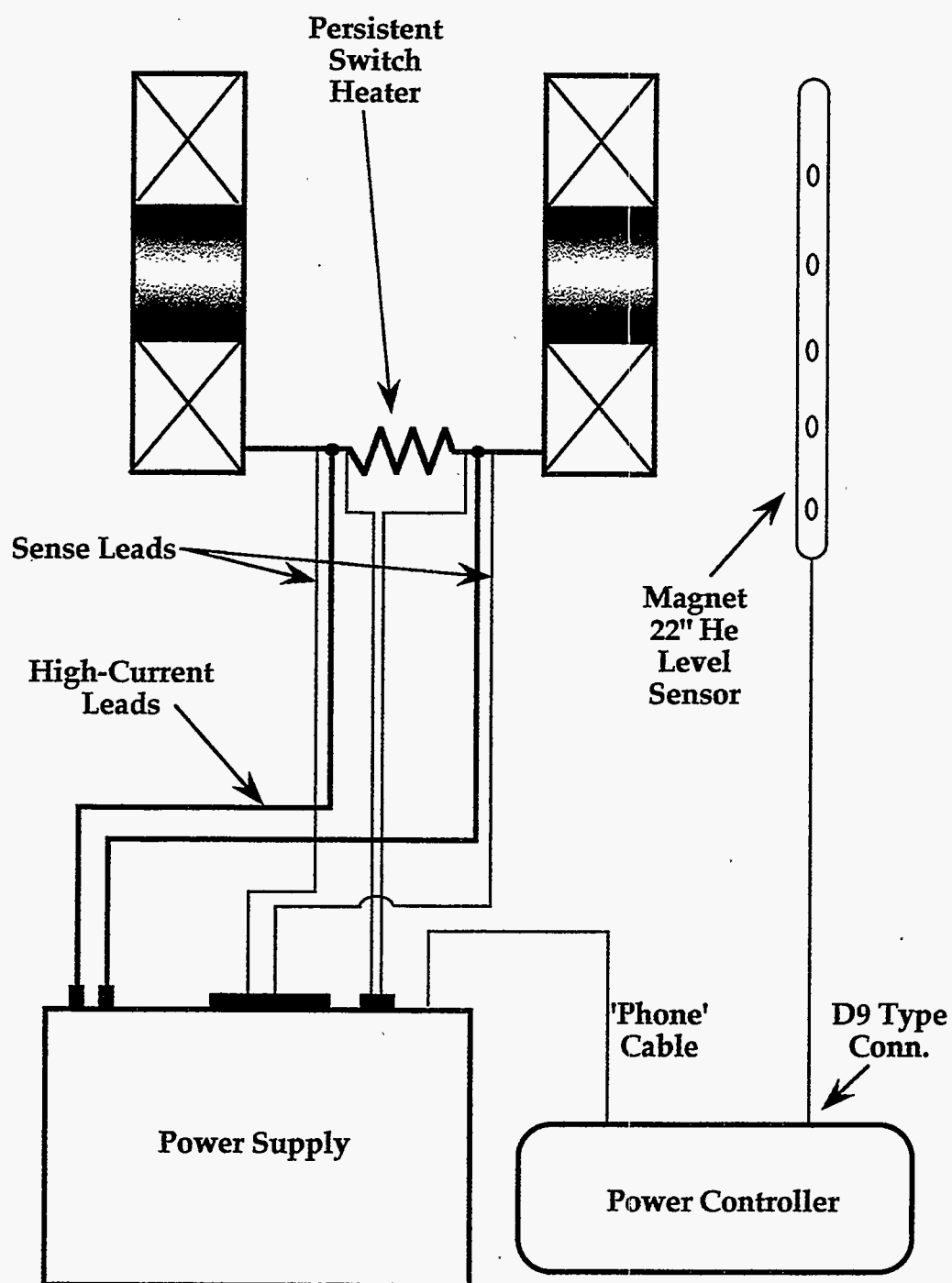

Resistance (Ohms)	Temperature (K)
1.39	~285
2.32	77.2
3.25	64.3
4.59	43.4
6.62	37.3
8.19	33.1
12.01	28.8
51.46	4.20

Appendix D: Wiring Diagrams - Cryostat

Appendix D: Wiring Diagrams - Magnet

Appendix E: Pressure vs. Temperature for Liquid ^{4}He
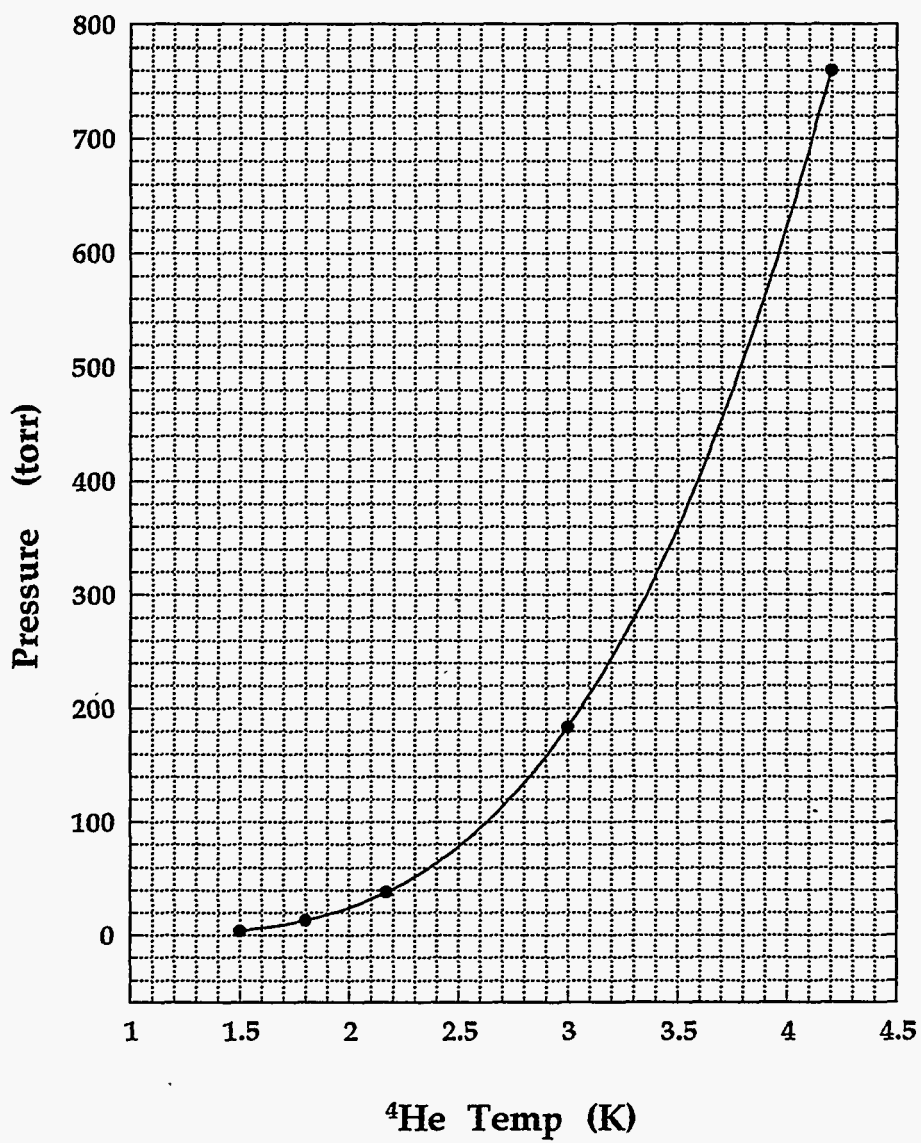
Appendix F: Pin-Outs and Magnet Specifications

Cryostat Pin-Outs for Electrical Feedthroughs

8-Pin Connector:

Pin A - **I+**

Pin B - **V+**   (For Charcoal Si Diode)

Pin C - **I-**

Pin D - **V-**

Pin E -

Pin F -

Pin G - **25 Ohm heater**

Pin H - **25 Ohm heater**

4-Pin Connector:

Pin A - **V-**

Pin B - **V+**   14" Active Length He Level Sensor

Pin C - **I-**

Pin D - **I+**

Appendix F: Pin-Outs and Magnet Specifications

19-Pin Connector:

      Pin A -

      Pin B -

      Pin C -

      Pin D -

      Pin E - **I+**

      Pin F - **V+**   #26404 Ge Resistance Sensor

      Pin G - **I-**

      Pin H - **V-**

      Pin J - **I+**

      Pin K - **V+**   Radiation Shield Si Diode

      Pin L - **I-**

      Pin M - **V-**

      Pin N - **Rad Shield Heater**

      Pin P -

      Pin R -

      Pin S -

      Pin T -

      Pin U - **Rad Shield Heater**

      Pin V -

Appendix F: Pin-Outs and Magnet Specifications

Magnet 19-Pin Connector:

Pin A - **V-**

Pin B - **V+**   22" Active Length Helium Level Sensor

Pin C - **I-**

Pin D - **I+**

Pin E - **V-**

Pin F - **V+**   22" Active Length Helium Level Sensor (spare)

Pin G - **I-**

Pin H - **I+**

Pin J - **-S**   Magnet Voltage Sense Lead

Pin K - **+S**   Magnet Voltage Sense Lead

Pin L - **Persistent Switch Heater**

Pin M - **Persistent Switch Heater**

Pin N -

Pin P -

Pin R -

Pin S -

Pin T -

Pin U -

Pin V -

Magnet Specifications

Rated Central Field @ 4.5 K	60 kG (6 T)
Rated Max Current	87.95 Amps
Maximum Test Field @ 4.2 K	63.4 kG (6.34 T)
Field to Current Ratio	682.2 G/A (0.0682 T/A, 14.7 A/T)
Homogeneity over 1 cm	±0.5%
Inductance	31.35 Henries
Persistent Heater Current	46 mA
Persistent Heater Resistance	65.8 Ohms

NEVER EXCEED MAXIMUM RATED CURRENT

DO NOT OPERATE SYSTEM WITH LESS THAN 12.5″ LHE IN MAGNET

Chapter X

X-Ray Magnetic Circular Dichroism at Temperatures < 1 K: Demonstration with the Blue Copper Site in Plastocyanin[1]

ABSTRACT

We have demonstrated the first XMCD to be taken at ultra-low temperatures (< 1K) using a ^{3}He cryostat. By measuring the XMCD at a fixed temperature and varying fields, we have been able to plot a magnetization curve for the S=1/2 Cu site in the protein plastocyanin. This magnetization curve allows us to definitively calculate the temperature at the surface of the sample and remove any ambiguity related to the system thermometry. These experiments at low temperature open the door to further study of more complicated systems by optimizing the observable XMCD effect and allowing us to reach a wide range of field and temperature combinations.

Introduction

X-ray Magnetic Circular Dichroism (XMCD) is the differential absorption of left and right circularly polarized X-rays in the presence of a magnetic field. This technique can provide element and oxidation state specific information about the magnetic properties of isolated metal centers, complex clusters, or multilayers. As the number of synchrotron sources capable of providing high photon flux and variable photon helicity grows, the XMCD technique is getting an increased amount of attention.

XMCD was first predicted for the $M_{4,5}$ edges of rare earth elements [1] and a linear dichroism effect was demonstrated experimentally at the Tb edge in a terbium-iron garnet [2]. The theory was then used to predict XMCD for the 3d transition metal $L_{2,3}$ edges [1,3] and demonstrated for several ferromagnetic and ferrimagnetic systems [4]. Soft XMCD was first demonstrated for a paramagnetic, biological system by probing the Fe site of rubredoxin from Pyrococcus furiosus [5]. Unlike the ferromagnetic or ferrimagnetic systems studied previously, a paramagnetic system requires a much stronger field and lower temperature to align the magnetic moment.

The blue copper protein, plastocyanin, has been the subject of intense interest and study due to its importance in biological systems as an electron transferase [6]. The active site consists of Cu in a C_{3v} distorted T_d Geometry [7] with a short thiolate S(cys)-Cu (2.07Å), a long thioether S(met)-Cu (2.82Å),

and two normal N(his)-Cu (~2Å) bonds [8]. It exhibits unique spectral features, including an intense blue color which Gray and coworkers predicted [9] to be a S(cys)-Cu charge transfer transition in a distorted tetrahedral site. These unique spectral features have been shown to arise from a highly covalent site [10]. More recently, Cu L-edge XAS has been used to quantify the high covalency of the copper site [11]. Using a sum rule relating the integrated L-edge intensity to the number of d-vacancies, it was shown that about half of the formal d vacancy is filled by charge transfer from the ligands.

Other sum rules developed by Carra [12], Thole [13] and Altarelli [14] relate the integrated XMCD intensity to the orbital angular momentum. Plastocyanin is an ideal candidate for testing these sum rules, since it consists of a single, paramagnetic S=1/2 Cu center with well understood electronic structure. The sample concentration is sufficient for good signal to noise. Furthermore, Arrio and coworkers [15] have developed analytical expressions that relate the XMCD to crystal field strength and spin-orbit splittings.

In this paper, we present the first XMCD experiments performed at very low temperatures, using the copper site in plastocyanin as a test system. By incorporating a ^{3}He cryostat into our split-coil superconducting magnet [16], we have been able to conduct XMCD experiments at temperatures <1 K, as demonstrated by the field dependence of the magnetization curve. The success of these experiments opens the door to further study of other

complex metal clusters of both chemical and biological interest.

Experimental

Sample Preparation: Plastocyanin was isolated from spinach by previously published methods [17] to a final concentration of ~0.8mM in 250mM potassium phosphate (pH=7) buffer. The sample was dehydrated onto a gold-plated, copper sample holder that was tightly screwed into a threaded opening with a tapered end on the sample cold finger. To guarantee good thermal all copper contact points between the sample holder and cold fingerconta were cleaned with an HCl/ZnCl flux to remove any oxide layers and thermally conductive grease was applied to the tapered end to ensure good contact at all points. During the experiment, the beam position on the sample was changed frequently, to minimize damage from photoreduction.

Experimental Set-Up: Experiments were conducted at the Stanford Synchrotron Radiation Laboratory on beamline 5-2 [18]. This beamline is ideal for these experiments due the newly installed elliptically polarized undulator [19]. This insertion device is capable of producing the high brightness of an undulator, with the added advantage of being able to produce photons of left and right circular polarization, under control of the experimenter. In principle, only the photon helicity is changed as the insertion device magnet phase is swept, the beam path through the optics and the beam position on the sample are preserved throughout the experiment.

This inherent stability eliminates any errors introduced by adjusting entrance slits or changing tilt of the entrance mirrors to swap polarization, as is typically done with bend magnet beamlines [20].

The XMCD apparatus used a superconducting split-coil magnet, enclosed in a UHV compatible chamber which connects directly with beamline
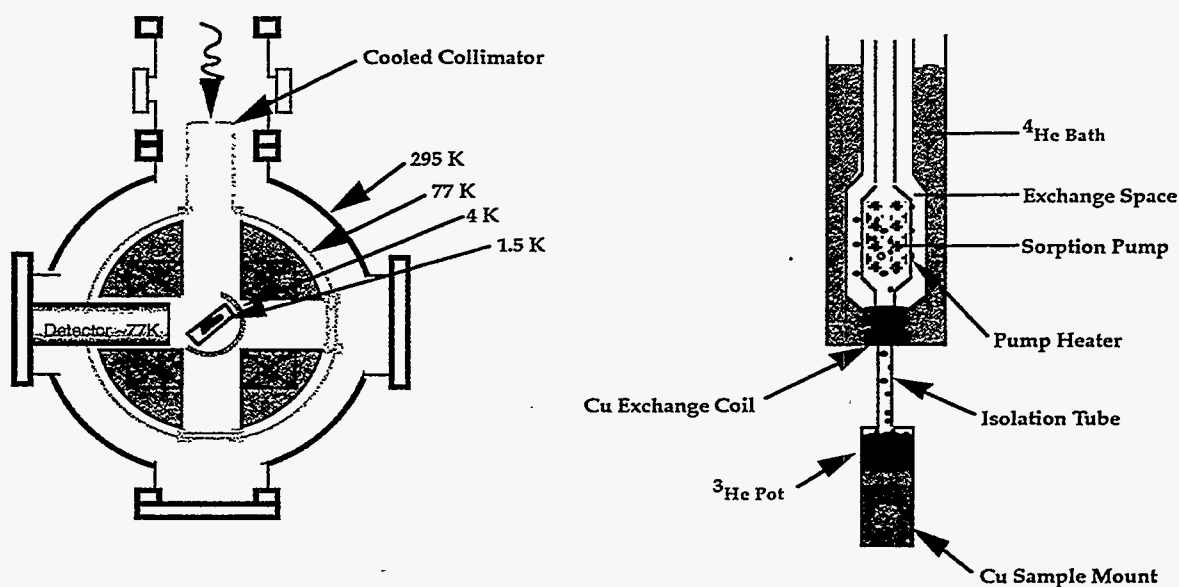

Figure 1: (left) Overhead schematic view of the magnet, detector and shielding layout. The sample is located in the very center, within the 1.5 K shielding. (right) Schematic diagram of te ^{3}He cryostat and sample mount.

vacuum to eliminate absorbing windows in the light path [16]. A windowless, liquid nitrogen cooled, 13 element solid-state Ge array detector [21] is inserted between the two coils, perpendicular to the photon beam path (Figure 1). A ^{3}He cryostat is inserted from the top of the chamber and the cold finger sits at the center of the split between the two coils in the region of

uniform field (Figure 1).

The cryostat is a single-shot, pumped charcoal ^{3}He design [22] (Figure 1, bottom right). The temperature of the sample cold finger is monitored by a Ge resistance thermometer located ~3 mm behind and ~5mm above the center of the sample surface. This sensor indicated temperatures of ~0.3 K when the cryostat was fully cooled in the absence of a magnetic field. In order to shield the sample from heat sources, several shields were used (Figure 1, top left). Surrounding the sample cold finger is an Al shield which is attached to the cryostat's liquid He reservoir which operates at 1.5 K, Figure 1: (top, left) Overhead schematic view of the magnet, detector and shielding layout. The sample is located in the very center, within the 1.5 K shielding. (bottom, right) Schematic diagram of the ^{3}He cryostat and sample mount although higher temperatures were measured on the outside of the shield during the run. The front of this shield has a thin (1000Å) Al window which lets the x-ray beam enter and the fluorescence emission exit to the Ge detector. There is a 50 ohm heater wrapped around the top of this shield to help prevent icing of the thin Al window during cooldown. There is another shield that surrounds approximately 80% of the 1.5 K shield that is connected to the magnet 4.2 K liquid He supply and can be dropped down to allow for optical access to the interior of the magnet bore. Viewports at the rear of the magnet and opposite the detector are sealed at the liquid nitrogen shield by cooled quartz windows. Heat source input from the beampipe was

minimized by attaching a liquid nitrogen cooled aluminum collimator with a 9.5 mm opening.

Data Acquisition: Data were collected in two ways: spectral comparison and single energy counting. In both cases the detector amplifiers were set to 6 μs shaping time and count rates were kept in a linear range. For the spectral comparison method, the detector was set to count on the Cu L emission peak for the duration of the scan. Then, either the magnetic field or beam polarization was switched. Accompanying spectra taken without any magnetic field and alternating beam polarization were also taken to check for zero field effects and changes in energy calibration. All spectra for a given configuration were then compared for the presence of increased photoreduced Cu. None of the spectra collected showed any evidence for a change in the amount of photoreduction in a data set. Spectra for each field and/or polarization were then compared and the peak integrated to get the total peak intensity and the resulting XMCD effect is reported as I_l-I_r/I_l+I_r.

The second method employed was that of single energy counting. In this configuration, the detector would accumulate counts for 120 seconds in two windows, one set for the O Kα and the other for the Cu L emission while the energy was fixed at 942 eV. The energy was then moved to 938 eV and a 'background' taken by accumulating counts as before. The ratio of these two (peak-baseline) signals at different fields and polarizations can then be used to

calculate the XMCD effect at that single energy point.

Results and Discussion

The XMCD in the L_3 edge of plastocyanin in a 1 Tesla field is shown in

Figure 2. A strong, ~40% effect is clearly visible[2]. Data of this type was
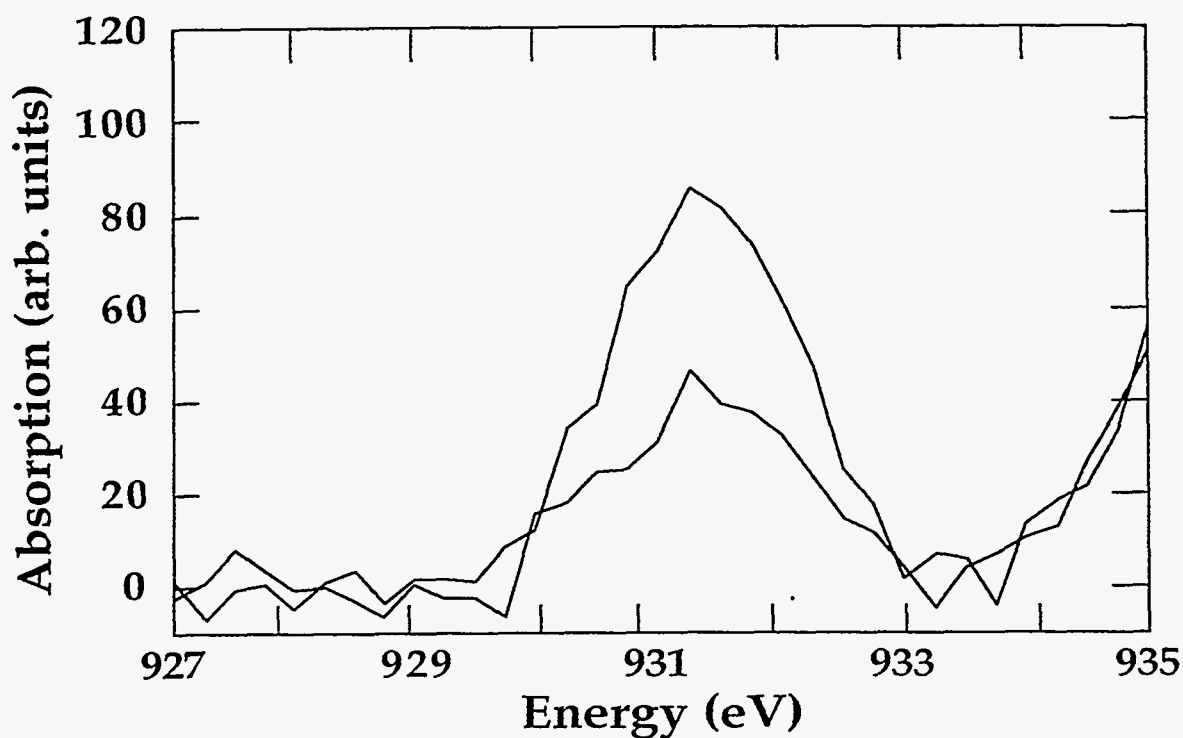

Figure 2: A demonstration of the XMCD effect for a 1 Tesla field and ~0.3 K. The two lines represent different combinations of opposite beam helicity and/or opposite magnetic field.

collected for several fields and the temperature was held fixed at a measured

value of 0.3 K at the cold finger.

---

[2] The rapidly rising baseline at the high energy side of the scan is due to transitions to 4s and continuum states and possibly to the presence of photoreduced protein. There were not any detectable changes in amplitude for all the scans used to generate this data. Since protein in the Cu(I) state does not contribute to the 2p->3d L_3 transition, a modest fraction of photoreduced Cu(I) protein does not interfere with the magnetization curve measurements.

All of the data collected were then graphed on a magnetization plot showing the size of the effect versus the field/temperature ratio. For an isotropic S=1/2 system, it has been shown that the XMCD should be of the form [23]:

$$XMCD = A \cdot Tanh\left[\frac{g\mu B}{2kT}\right] \qquad (1)$$

where A is a normalization constant, μ/k is the ratio of the Bohr magneton and the Boltzmann constant, g is the electron g-factor (~2.00 for this case) and
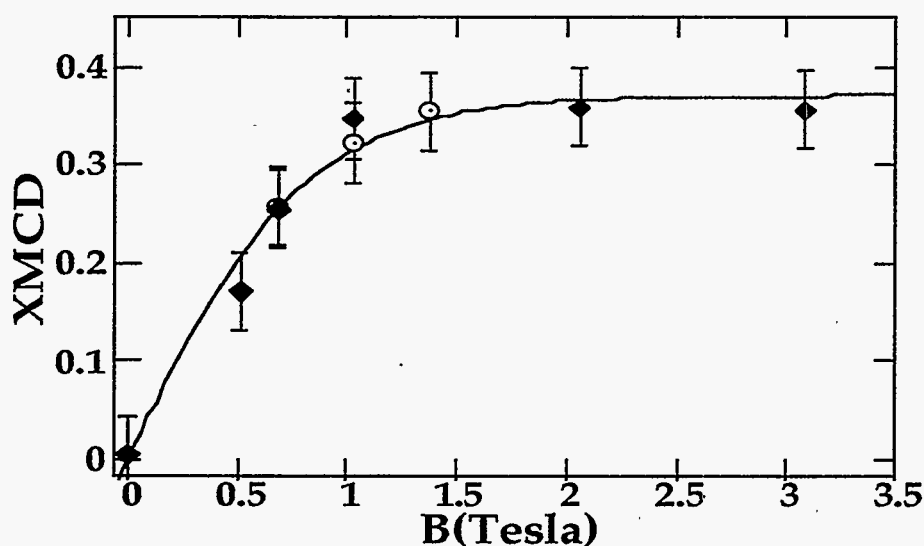

Figure 3: The magnetization curve for Cu Plastocyanin at a monitored temperature of ~300mK. The solid black diamonds indicate data points derived directly from the individual data sets while the open circles are from data collected by the single energy counting method.

the ratio B/T is the field/temperature ratio. By fitting this functional form to the data with known B and optimized A and T, the temperature of the sample surface can be accurately determined. Knowledge of the true sample surface temperature is important, since temperature sensors located elsewhere within the system will probably monitor a lower temperature than that actually present on the surface. Due to their chemical composition, protein samples such as plastocyanin are not good thermal conductors, and the short penetration depth of soft x-rays means that the surface of the sample is receiving a higher radiation dose and heat load.

The results of this curve fitting are shown in Figure 3. The points shown as solid diamonds represent the data points taken by spectral comparison, the open circles represent points taken using the single energy counting method. A nonlinear least-squares fit to equation (1) yields a temperature of 0.55 ± 0.05 K.

By using the following equation for themal conductivity:

$$k(\Delta T) = \left(\frac{\dot{Q}}{\Delta T}\right) \cdot \left(\frac{l}{a}\right) \tag{2}$$

where a is the area and l is the length of the flow of heat, ΔT is the difference in temperature between the two sides of the sample and dQ/dt represents the heat flow with respect to time, a rough calculation can be performed for the

thermal conductivity of the protein sample. Assuming that the total heat load impinging on the surface of the sample is on the order of $\sim 10^2$ microwatts and beam dimensions of ~ 5 mm^2 with an approximate sample thickness of ~ 50 microns, a thermal conductivity can be derived that is on the order of 10^{-2} milliwatts/cm/K. This value can be compared to the thermal conductivities at $\sim 1K$ for high purity copper metal, $\sim 7x10^3$ mW/cm/K and stainless steel, $\sim 10^{-1}$ mW/cm/K [22]. For the energies used in these experiements, the photon flux of $\sim 10^{11}$ photons/second, only introduces $\sim 15\mu W$ to the overall sample heat load. As new insertion devices are commissioned which promise substantial increases in photon flux, this contribution will rapidly become very important in calculations of this type.

Summary

These results have established that XMCD can be recorded in modest magnetic fields at temperatures < 1K. This sets the foundation for further experiments on more complex systems. Magnetization curves of S=1/2 systems establish a precise temperature at the surface of the sample and can be used as a calibration for future experiments. By using lower magnetic fields, there is less interference with fluorescence detection equipment and maximum signal throughput. These are critical factors in experiments on dilute metalloprotein systems. Ultra-low temperature XMCD should allow characterization of very weakly coupled magnetic systems.

References

(1) B.T. Thole, G. Van der Laan and G.A. Sawatzky, *Phys. Rev. Lett.*, *55* (1985) 2086-2088.

(2) G. van der Laan, B.T. Thole, G.A. Sawatzky, J.B. Goedkoop, J.C. Fuggle, J.-M. Esteva, R. Karnatak, J.P. Remeike and H.A. Dabkowska, *Phys. Rev. B, 34* (1986) 6529-6531.

(3) G. Van der Laan and B.T. Thole, *Phys. Rev. B, 43* (1991) 13401-13411.

(4) a) F. Sette, C.T. Chen, Y. Ma, S. Modesti and N.V. Smith, *AIP Conf. Proc., 215* (1990) 787-795. b) P. Rudolf, F. Sette, L.H. Tjeng, G. Meigs and C.T. Chen, *J. Magn. Mag. Mat. 109* (1992) 109-112.

(5) J. VanElp, S.J. George, J. Chen, G. Peng, C.T. Chen, L.H. Tjeng, G. Meigs, H.-J. Lin, Z.H. Zhou, M.W.W. Adams, B.G. Searle and S.P. Cramer, *Proc. Natl. Acad. Sci. USA, 90* (1993) 9664-9667.

(6) a) E.I. Solomon, M.J. Baldwin and M.D. Lowery, *Chem. Reviews, 92* (1992) 521. b) S.K. Chapman in R.W. Hay, J.R. Dilworth and K.B. Nolan (eds.), Perspectives in Bioinorganic Chemistry, JAI Press, London, 1991, p. 95ff. c) H.B. Gray and E.I. Solomon in T.G. Spiro (ed.), *Copper Proteins,* John Wiley & Sons, New York, 1981, p.3ff.

(7) K.W. Penfield, R.R. Gay, R.S. Himmelwright, N.C. Eickman, V.A. Norris, H.C. Freeman and E.I. Solomon, *J. Am. Chem. Soc.*, *103* (1981) 4382.

(8) J.M. Gus and H.C. Freeman, *J. Mol. Biol.*, *169* (1983) 521-563.

(9) a) D.R. McMillan, R.C. Rosenberg and H.B. Gray, *Proc. Natl. Acad. Sci. USA*, *71* (1974) 4762. b) D.R. McMillan, R.A. Holwerda and H.B. Gray, *Proc. Natl. Acad. Sci. USA*, *71* (1974) 1339-1341. c) E.I. Solomon, J. Rawlings, D.R. McMillan, P.J. Stephens and H.B. Gray, *J. Am. Chem. Soc.*, *98* (1976) 8046-8048.

(10) K.W. Penfield, A.A. Gewirth and E.I. Solomon, *J. Am. Chem. Soc.*, *107* (1985) 4519

(11) S.J. George, M.D. Lowery, E.I. Solomon and S.P.Cramer, *J. Am. Chem. Soc.*, *115* (1993) 2968-2969.

(12) P. Carra, *Jpn. J. Appl. Phys.*, *S32* (1993) 279-283.

(13) B.T. Thole, P. Carra, F. Sette and G. Van der Laan, *Phys. Rev. Lett.*, *68* (1992) 1943-1946.

(14) M. Altarelli, *Phys. Rev. B*, *47* (1993) 597-599.

(15) M.-A. Arrio, Ph. Sainctavit, C. Brouder and C. Deudon, *Physica B,* *208&209* (1995) 27-28.

(16) S.J. George, J. VanElp, J. Chen, G. Peng, S. Mitra-Kirtley, O.C. Mullins and S.P. Cramer in B. Chance, J. Deisenhofer, S. Ebashi, D.T. Goodhead, J.R. Helliwell, H.E. Huxley, T. Iizuka, J. Kirz, T. Mitsui, E. Rubenstein, N. Sakabe, T. Sasaki, G. Schmahl, H.B. Stuhrmann, K. Wüthrich and G. Zaccai (ed.), *Synchrotron Radiation in the Biosciences,* Oxford University Press, New York, 1994, p.313.

(17) W.L. Ellefson, E.A. Ulrich, D.W. Krogmann, *Methods Enzymol., 69* (1980) 223-228.

(18) R.Z. Bachrach, R.D. Bringans, B.B. Pate and R.G. Carr, *SPIE Proceedings, 582* (1985) 251.

(19) S. Lidia, R. Carr, *Nucl. Instr. and Meth., A347* (1994) 77-82.

(20) a) C.T. Chen, F. Sette, N.V. Smith, *Appl. Opt., 29,* (1990) 4535-4536. b) C.T. Chen, *Rev. Sci. Instrum., 63* (1992) 1229-1233.

(21) S.P. Cramer, J. Chen, S.J. George, J. VanElp, J. Moore, O. Tensch, J.

Colaresi, M. Yocum, O.C. Mullins and C.T. Chen, *Nucl. Instr. and Meth.,* *A319* (1992) 285-289.

(22) For general discussion see: A. Kent, *Experimental Low Temperature Physics*, Macmillan Press, London, 1993.

(23) C. Kittel, *Introduction to Solid State Physics*, John Wiley & Sons, New York, 1986, p. 401.